

Efficiency Analysis of a Radial Piston Pump Applied in a 5MW Wind Turbine with Hydraulic Transmission

Kasper Aastrup Mortensen

Klaus Høj Henriksen

Master Thesis in Electro-Mechanical System Design

Aalborg University 2011

EFFICIENCY OF A RADIAL PISTON PUMP APPLIED IN A 5 MW WIND TURBINE

Master Thesis in Electro-Mechanical System Design

Kasper Aastrup Mortensen
Klaus Høj Henriksen



EFFICIENCY OF A RADIAL PISTON PUMP APPLIED IN A 5 MW WIND TURBINE

Abstract:

This master thesis addresses a pump which PMC Servi has suggested for application in hydraulic transmission in a wind turbine. A mechanical and hydraulic model is constructed and several standard valves are tested and the NG63 valve is chosen for further analysis. By conducting CFD-analysis a new deflector valve is designed. By inserting this into the non-linear model, an efficiency of the system is found to be 0.983127 which was 0.74 percentage points higher than the NG63 valve. Multiple valves are then tested, and the set-up with two valves as both in- and outlet is chosen with a resulting efficiency of 0.992038. The model is then expanded with a friction and leakage model for the piston rings applied on each piston of the pump. This model is then attempted utilised on the slipper pad bearing between the eccentric shaft and the piston rod. Due to a lack of non-linear behaviour of the pressure in the slit the model proved incapable of modelling the fluid film height and thus a steady state model is constructed instead. With friction and leakage from the piston ring and slipper pad included, the overall efficiency is found to be 0.98937.

Project: Master Thesis in EMSD
ECTS: 60
Project period: Fall 2010 and spring 2011
Project group: 54D

Klaus Høj Henriksen

Kasper Aastrup Mortensen

Supervisor: Torben O. Andersen
Enclosed: 1 CD
Date of completion: 31/5-2011

Prints in circulation: 5
Pages excluding Appendix: 105
Pages including Appendix: 127

By signing this document, each member of the project group certifies that all have contributed equally in the writing of this project and thereby jointly being liable for the contents of this report.

Preface

This thesis is a product of a master project in the field of Mechanical Engineering with specialisation in Electro-Mechanical System Engineering (EMSD) at Aalborg University. It has been written by project group 54D on 10th semester from September 1st 2010 to May 31st 2011.

This report is addressed to readers with a basic knowledge of mathematical modelling describing, mechanical- and hydraulic systems.

Figures, equations, and tables are numbered continuously throughout each chapter and appendix. E.g. Figure 4.3.2 is Figure 2 in section 3 in chapter 4. The symbols applied in the report is gathered in the nomenclature with a description and the unit and is placed before the introduction. A CD is enclosed with the report and contains the articles mentioned in the bibliography, the SimuLink models constructed, CFD results, and Maple sheet for several of the calculations.

We would like to acknowledge and give special thanks to Thomas Condra for help and guidance with the CFD analysis and the dimensional analysis and to Anders Christian Olesen for assistance with the ANSYS programming.

Guide

This report uses the Harvard system of referencing. In context this appears as the authors surname and year of publishing in square brackets, e.g. [Phillips, 2000]. If the year of publishing is uncertain or unknown this will be followed by an asterisk, e.g. [Phillips, 2000*]. The references cited are found in detail in the *Bibliography* sorted alphabetically by authors surname.

Appendices and enclosures are referred to as e.g. *appendix A.2* or *enc. I.3*. Enclosures are found on the enclosed CD.

Contents

Nomenclature	V
1 Introduction	1
1.1 Offshore Wind Industry	1
1.2 Application of Hydraulic Transmission in a Wind Turbine	3
1.3 The PMC Servi Pump	5
2 Non-linear Pump Model	9
2.1 Mechanical Model	9
2.2 Hydraulic Model	16
2.3 Simulation	26
2.4 Problem Analysis and Approach	31
3 Valve Design	33
3.1 Computational Fluid Dynamics Analysis	33
3.2 Deflector Design	35
3.3 CFD Results	38
3.4 Variable C_d Implementation	46
3.5 Parameter Variation	47
3.6 Summary	54
4 Friction and Leakage Analysis	57
4.1 System Description	57
4.2 Piston Ring Friction and Leakage	58
4.3 Slipper Pad Friction and Leakage	72
4.4 Friction and Leakage Results	90

4.5	Summary	95
5	Conclusion	97
6	Summary	101
	Bibliography	103
A	Hydraulic Model	107
A.1	Variable Stiffness	107
B	CFD	109
B.1	Fundamental Fluid Dynamics	109
B.2	Boundary Conditions	111
B.3	Meshing	111
B.4	CFD Result Figures	116
C	Opening Area of Deflector Valve	119
C.1	Stage 1	119
C.2	Stage 2	120
D	Friction and Leakage	125
D.1	Flow Factors	125

Nomenclature

Nomenclature	Description	Unit
α_j	Jet angle of fluid exiting valve	$[rad]$
β	Bulk modulus	$[Pa]$
δ	Surface roughness profiles of surface one and two respectively	$[m]$
ε	Angle in mechanical model, cf. Figure 2.1.6	$[rad]$
η	Efficiency	$[-]$
θ_r	Rotor angle	$[rad]$
θ_{int}	Angle between cylinders	$[rad]$
κ	Frictional coefficient in poppet valve	$[-]$
μ	Dynamic viscosity	$[Pa \cdot s]$
ν	Kinematic viscosity	$[m^2/s]$
ν_1 / ν_2	Possions ratio of material one and two	$[-]$
ξ	Angle in mechanical model, cf. Figure 2.1.2	$[rad]$
ρ	Density of the hydraulic fluid	$[kg/m^3]$
σ	Surface roughness	$[m]$
τ_L	Load torque on motor	$[Nm]$
τ_r	Rotor torque	$[Nm]$
τ_{CR}	Torque in connecting rod	$[Nm]$
σ	Surface roughness	$[m]$
σ^*	Non-dimensional Surface roughness $\sigma^* = \frac{\sigma}{c}$	$[m]$
ϕ	Angle in mechanical model, cf. Figure 2.1.2	$[rad]$
ϕ_c	Contact flow factor concerning the average gap between two surfaces	$[-]$
ϕ_f	Shear stress flow factor representing the sliding velocity component of shear stress.	$[-]$
ϕ_{fs}	Shear stress flow factor representing the ϕ_f but in terms of mean flow	$[-]$
ϕ_s	Flow factor representing additional flow due to sliding in a rough bearing	$[-]$
ϕ_x	Flow factor comparing the average pressure flow on a rough surface to that of a smooth surface	$[-]$
Ψ_P	Function examining for cavitation, cf. Equation 4.23	$[-]$
Ψ_{atm}	Function examining for cavitation, cf. Equation 4.23	$[-]$

Nomenclature	Description	Unit
ω_B	Angular velocity of booster pump	$[rad/s]$
ω_m	Angular velocity of motor	$[rad/s]$
ω_r	Angular velocity of rotor	$[rad/s]$
ω_{ref}	Reference angular velocity of rotor	$[rad/s]$
Ω	Constant 4.0	$[-]$
\mathcal{P}	Power loss	$[W]$
$A(x_{pop})$	Opening area of poppet	$[m^2]$
A_A	Pressure area of port A in valve	$[m^2]$
A_B	Pressure area of port B in valve	$[m^2]$
A_{in}	Inlet area of the valve	$[m^2]$
A_{inside}	Inside surface area of piston ring	$[m^2]$
A_M	Orifice area of motor	$[m^2]$
A_p	Surface area of the piston	$[m^2]$
$A_{outside}$	Outside surface area of piston ring	$[m^2]$
A_X	Pressure area of port X in valve	$[m^2]$
b	Height of the piston ring	$[m]$
c	Nominal clearance	$[m]$
c_f	Friction coefficient	$[-]$
C_d	Discharge coefficient	$[-]$
C_{con}	Converge criteria of numerical method	$[-]$
d	Distance between the shafts, cf. Figure 2.1.2	$[m]$
d_c	Diameter of capillary tube	$[m]$
\vec{e}_{sign}	Vector containing signs of errors regarding numerical method	$[-]$
D_H	Hydraulic Length	$[m]$
F_{asp}	Force caused by asperities	$[N]$
F_{cyl}	Force caused by cylinder pressure	$[N]$
F_{CR}	Force in connecting rod, cf. Figure 2.1.2	$[N]$
F_{fl}	Flow force on poppet	$[N]$
F_{fr}	Friction force on poppet	$[N]$
F_{fric}	Friction force in piston ring or slipper pad	$[N]$
F_g	Gravitational force	$[N]$
F_{GR}	Groove force in piston ring	$[N]$
F_{Lands}	Force caused by pressure across the lands of the slipper pad	$[N]$
F_p	Force caused by pressure in the fluid film on the piston ring	$[N]$
F_{PA}	Force on poppet caused by pressure in A	$[N]$
F_{PB}	Force on poppet caused by port B	$[N]$
F_{pocket}	Force caused by pocket pressure acting on the slipper pad	$[N]$
F_{PX}	Force on poppet caused by port X	$[N]$

Nomenclature	Description	Unit
F_N	Normal force in cylinder cf. Figure 2.1.2	$[N]$
F_r	Force caused by rotor torque, cf. Figure 2.1.2	$[N]$
F_{RS}	Reaction force in central shaft, cf. Figure 2.1.2	$[N]$
F_{spr}	Spring force on poppet	$[N]$
h	Film height between piston ring and cylinder wall	$[m]$
h_{lim}	Maximum squeeze film	$[\frac{m}{s}]$
h_{land}	Film height between slipper pad and eccentric shaft	$[m]$
$h_{land_{opt}}$	Optimal film height between slipper pad and eccentric shaft	$[m]$
H	Non-dimensional film height $H = \frac{h}{c}$	$[m]$
J_r	Mass moment of inertia of rotor	$[kg \cdot m^2]$
l	Length of connecting rod, cf. Figure 2.1.2	$[m]$
l_p	Length of piston rod, cf. Figure 2.1.2	$[m]$
L_H	Height the slipper pad, cf. Figure 4.3.2	$[m]$
$L_{H_{pocket}}$	Height of pocket area, cf. Figure 4.3.2	$[m]$
L_i	Length of the land. Equal to L_1, L_2, L_3 or L_4 , cf. Figure 4.3.2	$[m]$
L_{PR_x}	Depth of piston ring, cf. Figure 4.4.4	$[m]$
L_{PR_y}	Height of piston ring, cf. Figure 4.4.4	$[m]$
L_W	Width of the slipper pad, cf. Figure 4.3.2	$[m]$
$L_{W_{pocket}}$	Width of the pocket, cf. Figure 4.3.2	$[m]$
M_p	Mass of piston	$[kg]$
M_{pop}	Mass of poppet	$[kg]$
p	Pressure in fluid film, only used in chapter 4	$[Pa]$
P_{atm}	Atmospheric pressure	$[Pa]$
P_{BP}	Bearing pocket pressure	$[Pa]$
P_C	Cylinder pressure	$[Pa]$
P_H	High pressure	$[Pa]$
P_L	Low pressure	$[Pa]$
P_t	Tank pressure	$[Pa]$
$P(X, T)$	Pressure through the film	$[Pa]$
Q_B	Flow produced by booster pump	$[m^3/s]$
Q_{cap}	Flow through the capillary tube	$[m^3/s]$
Q_H	Flow through high-pressure tube	$[m^3/s]$
Q_L	Flow through low-pressure tube	$[m^3/s]$
Q_{land}	Leakage flow across the land	$[m^3/s]$
Q_{leak}	Leakage flow across the piston ring	$[m^3/s]$
Q_{VH}	Flow through outlet valve	$[m^3/s]$
Q_{VL}	Flow through inlet valve	$[m^3/s]$

Nomenclature	Description	Unit
r_τ	Length from central shaft to slipper pad, cf. Figure 4.3.8	[m]
r_A	Radius applied in calculation of opening area in poppet, cf. Figure 2.2.8	[m]
r_B	Radius applied in calculation of opening area in poppet, cf. Figure 2.2.8	[m]
r_{ecc}	Radius of eccentric shaft, cf. Figure 4.3.8	[m]
r_{ring}	Radius piston ring	[m]
r_{cyl}	Radius cylinder	[m]
r_{pp}	Ratio between the piston area and pocket are, cf Equation 4.53	[—]
r_{WH}	Ratio between length and width of the slipper pad	[m]
Re	Reynolds no.	[—]
s	Length applied in calculation of opening area in poppet, cf. Figure 2.2.8	[m]
T	Non-dimensional time $T = t\omega$	[m]
u_{in}	Velocity of fluid at valve inlet	[m/s]
U	Velocity of piston	[m/s]
U^*	Non-dimensional $U^* = \frac{U}{d\omega}$	[—]
v_{surf}	Surface velocity of the eccentric shaft relative to the slipper pad	[m/s]
V_A	Velocity of point A, cf. Figure 2.1.6	[m/s]
V_B	Velocity of point B, cf. Figure 2.1.6	[m/s]
$V_{A/B}$	Angular velocity of point A around point B, cf. Figure 2.1.6	[m/s]
V_{p0}	Volume between cylinder and valve	[m ³]
V_H	Volume in high pressure tube	[m ³]
V_L	Volume in low pressure tube	[m ³]
V_{r1}	Variance ratio between two surface	[—]
w	Length applied in calculation of opening area in poppet, cf. Figure 2.2.8	[m]
w_{BR}	Width of the land	[m]
W_A	Asperity load in piston ring	[N/m]
W_{GR}	Groove load in piston ring	[N/m]
W_P	Fluid film load in piston ring	[N/m]
x_c	Cavitation point in fluid film	[m]
x_p, y_p	Coordinate system attached to the cylinder	[m]
x_{pop}	Poppet position	[m]
x_{pop*}	Distortion of spring in poppet	[m]
x_s, y_s, z_s	Coordinate system for the fluid film between piston ring and cylinder	[m]
X	Non-dimensional position through fluid film $X = \frac{2x}{b}$	[—]
X_c	Non-dimensional cavitation point in the fluid film $X = \frac{2x_c}{b}$	[—]

Introduction¹

This first chapter consists of a short introduction to wind turbines and a description of the initiating problem and how it is examined.

1.1 Offshore Wind Industry



Figure 1.1.1: Offshore wind turbines [EURO AVIA COMPANY, 2009].

The increasing demand on renewable energy has helped the wind power industry develop into a major growth industry. Especially the offshore wind energy which according to *EURO AVIA* will keep on growing excessively despite the financial crisis [EURO AVIA COMPANY, 2010]. Figure 1.1.2 illustrates the increment in constructions of offshore wind farms.

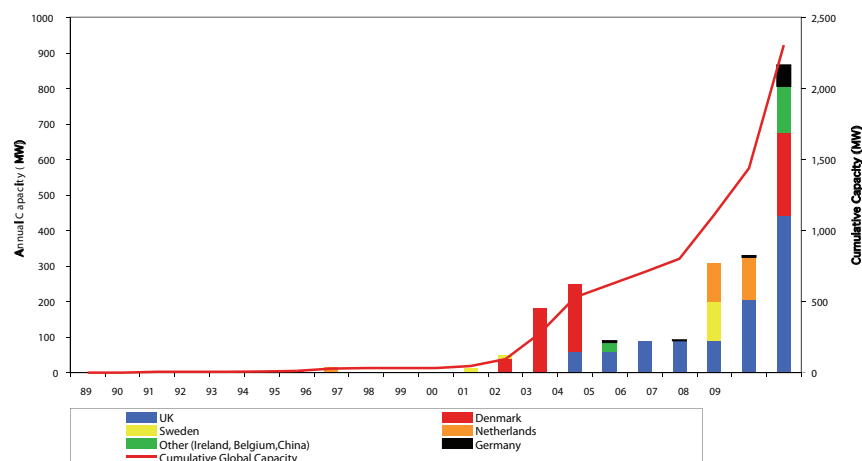


Figure 1.1.2: Global offshore wind build [BWEA, 2010].

The growth can be explained by a number of reasons:

- General increasing demand on renewable energy, e.g. the Danish energy agreement of increment of development of renewable energy in Denmark from [Klima- og Energiministeriet, 2008].
- Public interest in moving the wind turbines offshore. This is among other things to reduce the noise to residents living close to the wind turbines and the visual impact on the landscape.
- More stable and powerful wind speeds at sea.
- The construction of more and larger sea wind farms, e.g. *Horns Rev I & II* in Denmark and a future contract offer from the Danish government to build the next 400 [MW] offshore wind farm at Anholt DK [Energistyrelsen, 2009]. Further and greater wind farms are planned around the world, e.g. in the UK [BWEA, 2010].

Offshore wind farms are therefore subjected to a high degree of development in order to improve the technology and overcome difficulties. In a conventional wind turbine the gear, generator and bearings are installed in the nacelle, and hereby demanding a strong foundation. In fact, a reduction of one [kg] in the nacelle can save two [kg] of foundation [Ilsøy A., 2010]. The cost of the foundation represents 20 % of the cost of a typical large offshore wind farm [WindFacts, 2010]. This is why research into reduction of the weight, is a profitable business.

To reduce this weight, other concepts are considered, e.g. hydraulic power transmission. The basic concept is that the turbine drives a hydraulic pump connected to the shaft. The hydraulic fluid flows down through pipes to a hydraulic motor placed at the foundation, connected to a generator which produces power at grid frequency. A 900 kW prototype of a wind turbine using this technology has been constructed by *ChapDrive A/S*. ChapDrive is currently developing a 5[MW] design with higher efficiency and performance [ChapDrive, 2010].

A pump satisfying the given specifications does not exist, but *PMC Servi Cylinderservice A/S* has developed a pump concept which satisfies the demands [Ilsøy A., 2010]. An illustration of this concept is presented in Figure 1.1.3. The design is based on the concept of a radial piston pump with 14 cylinders, with an inlet and outlet valve for each cylinder. From this concept the initial problem is outlined:

To research the problems involving opening and closing the valve which controls the flow out of the cylinders.

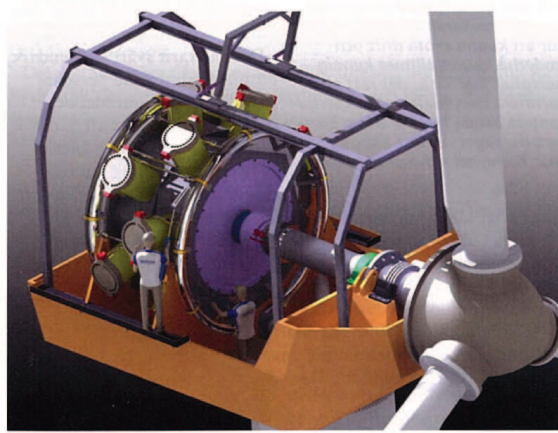


Figure 1.1.3: CAD of PMC Servi's pump design for a 5 MW wind turbine, installed in an appropriate nacelle [Ilsøy A., 2010].

1.2 Application of Hydraulic Transmission in a Wind Turbine

This section describes the requirements and limitations which emerges when considering hydraulic transmission in a wind turbine of the chosen size and power rating. To choose these specifications a technical report by J. Jonkman, S. Butterfield, W. Musial, and G. Scott titled *Definition of a 5-MW Reference Wind Turbine for Offshore System Development* is applied as reference [Jonkman et al., 2009]. The report represents a fictive reference offshore wind turbine project, and is based on a series of reports, case studies etc. from among others *Recommendations of Design of Offshore Wind Turbines Project*(RECOFF) and *US Department of Energy*(DOEs).

The report dictates that, to compete with existing conventional wind turbines and to be attractive for an installation at sea, the output power rating is required to be 5 [MW] [Jonkman et al., 2009]. This power rating is chosen since it has precedence and is widely chosen as the size of the offshore wind turbines [Jonkman et al., 2009].

A wind turbine of this size has, according to [Jonkman et al., 2009] the following specifications given in Table 1.2.1.

Parameter	Value	Unit
Power rating	5	[MW]
Rotor orientation & configuration	Upwind & 3 blades	-
Control	Variable speed, collective pitch	-
Transmission	High Speed, multiple-stage gearbox	-
Rotor & hub diameter	126, 3	[m]
Hub Height	90	[m]
Cut-in, Rated, Cut-Out Wind Speed	3, 11.4, 25	[m/s]
Cut-In, Rated Rotor Speed	6.9, 12.1	[rpm]
Rated Tip Speed	80	[m/s]
Overhang, Shaft Tilt, Precone	5, 5, 2.5	[m], °, °
Rotor Mass	110	[t]
Nacelle Mass	240	[t]
Tower Mass	347.46	[t]
Coordinate of Center of Mass	(-0.2, 0.0, 64)	[m]
Electrical Generator Efficiency	94.4	%

Table 1.2.1: Properties of NREL 5-MW wind turbine [Jonkman et al., 2009]

When replacing the gearbox with hydrostatic transmission, and installing pipelines through the tower to the ground, the gearbox is eliminated, and the generator can be moved to ground level. As mentioned earlier, this can reduce the weight. The concept, however, also adds another advantage; by moving the generator to ground level servicing and repair is eased, since the space around the components are not limited by the nacelle.

Two versions of hydrostatic transmission are known, closed or open.

If an open-loop system is installed, an unavoidable pressure drop is introduced when dumping the hydraulic oil to the tank. This is unfavourable since it reduces the overall efficiency. When the rotor of the turbine rotates above its rated speed the flow rises and surplus oil is dumped the tank, hereby introducing an energy dissipation. This will require a heat exchanger to cool the hydraulic fluid, which reduces the overall efficiency further [MHL Global Corporation Inc., 2008].

When using a closed-loop system, the tank can be eliminated i.e. the energy dissipation to the tank can be avoided. Instead a booster pump which keeps the pressure at a specific level, is required. The heat exchanger is also needed, as the oil temperature will rise over time, caused by energy dissipation. In addition the system can have difficulties if the rotor runs above its rated speed, due to the increased energy induced into the system. This energy can either be adjusted by the pump or be dissipated to the tank. To solve this a variable displacement motor with a constant velocity controller can be installed and connected to the generator. However, the problem of overrunning is still not solved if the flow increases massively [MHL Global Corporation Inc., 2008]. This is solved by pitch control of the wind turbine. This adjusts the angular velocity of the shaft, such that it does not change dramatically. Since this project focuses on the pump design, the velocity of the rotating shaft in the wind turbine is assumed to be constant.

1.3 The PMC Servi Pump

This section describes the concept of a radial piston pump and the complete hydraulic system. In the end of the section the PMC-Servi pump is described in detail for further analysis in the following chapter.

1.3.1 Concept

The PMC Servi pump works on the principal of a radial piston pump with 14 cylinders, divided on two eccentric shafts. A principal of a radial piston pump with seven cylinders is illustrated on Figure 1.3.1 and a hydraulic diagram of the system is illustrated on Figure 1.3.2.

Returning to Figure 1.3.1, *IDC* and *ODC* indicates the *Inner Dead Center* and *Outer Dead Center* of the pistons.

The blue areas on the right-hand side of the Figure refers to decompression and suction mode, where an inlet valve is open and fluid passes *into* the chamber. When the pistons are in these situations the pressure inside the cylinder (P_C) is equal to the low-pressure (P_L), if the pressure loss in the valves is neglected.

The yellow area indicates a compressed fluid with both valves closed. The red areas indicates a high pressure inside the chambers and an open outlet valve, passing fluid *out* of the cylinder. At this point the pressure of the fluid inside the chamber is at the same pressure or above the high pressure (P_H)

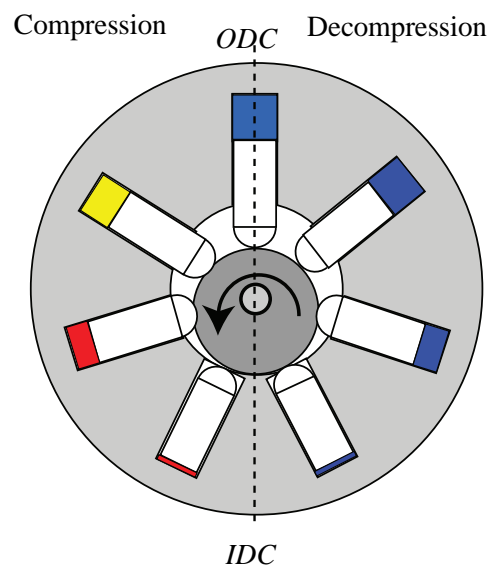


Figure 1.3.1: Radial piston pump.

1.3.2 Hydraulic System

This section describes the hydraulic system shown in Figure 1.3.2 consisting of:

- Radial piston pump - Modulated as 14 individual cylinders with two valves each.
- Motor - Modulated as an orifice between P_H and P_t and connected to a generator.
- Pipes between the components - Modulated as volumes.
- Booster circuit - Modulated by keeping P_L constant.

The system will be described in detail in section 2.2.

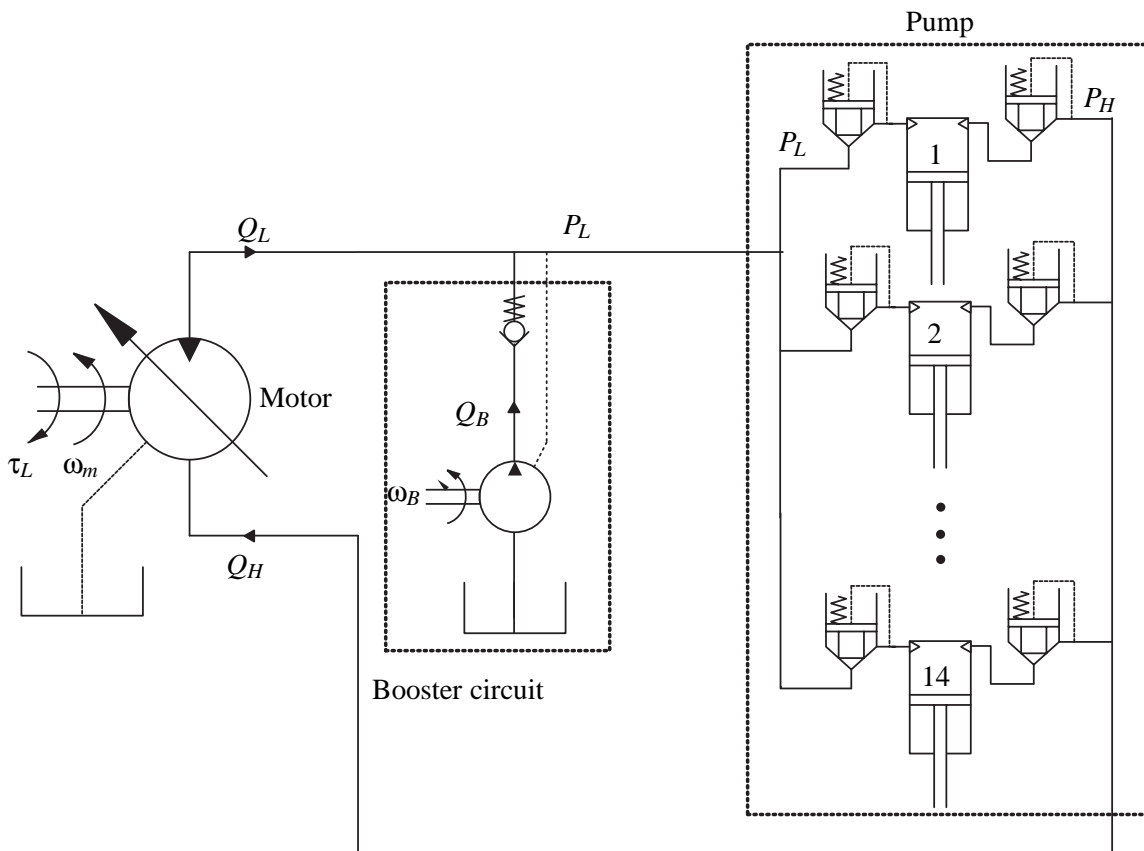


Figure 1.3.2: Hydraulic diagram.

1.3.3 PMC Servi Pump

As mentioned earlier PMC Servi has developed a pump design for a 5[MW] wind turbine which supposedly can fulfil the requirements of this application [Ilsøy A., 2010]. A CAD drawing of the pump is illustrated in Figure 1.3.3, and the specifications are given in Table 1.3.1.

The 14 cylinders are divided onto two eccentric shafts and rotated such that the angle between each cylinder is $2\pi/14$. Each cylinder has a flow output of $92.2 [l/stroke]$, and with a rotational speed of $10 [rpm]$ this results in a flow of $12,908 [l/min]$. When including the volumetric efficiency of 98 % the nominal flow of the pump is lowered to $12,656 [l/min]$ [Ilsøy A., 2010].

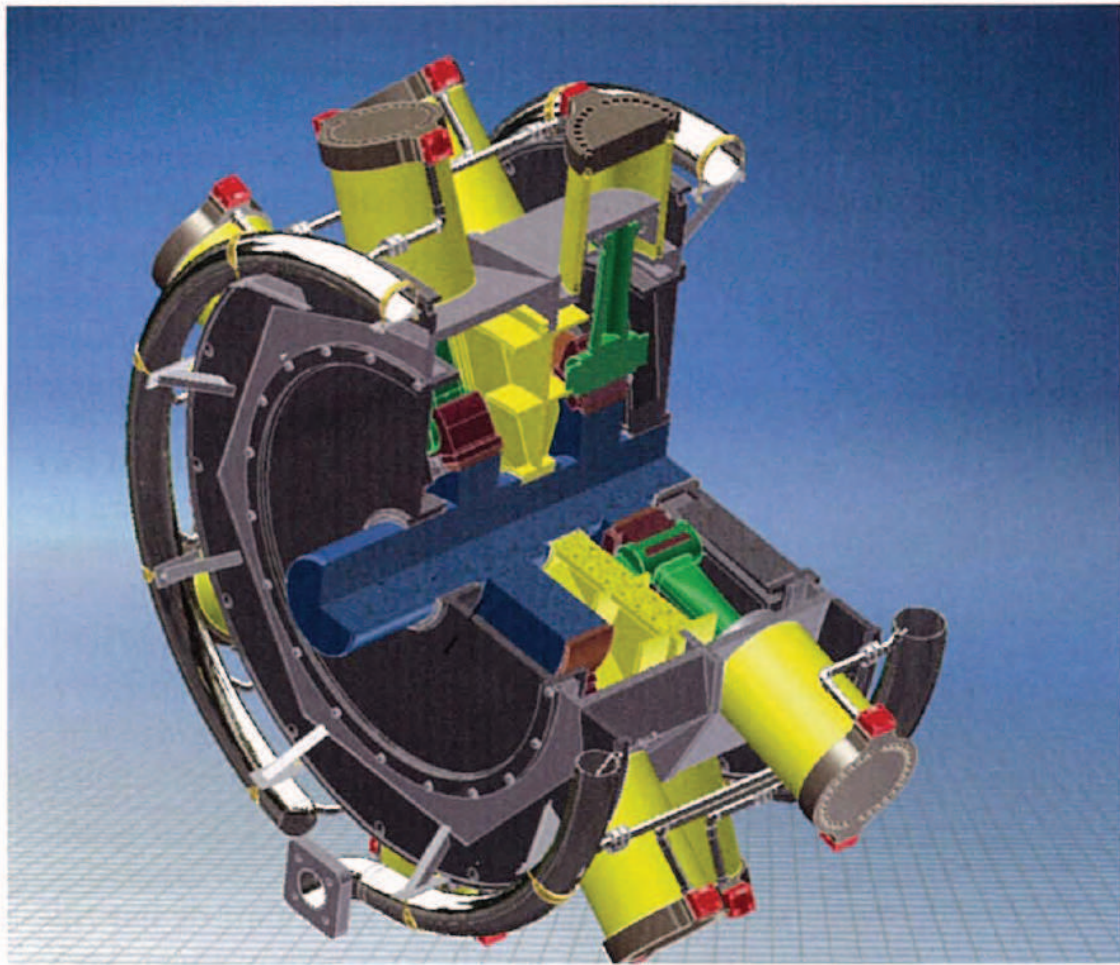


Figure 1.3.3: CAD of PMC Servi's pump design for a 5 MW wind turbine [Ilsøy A., 2010].

A significant factor when considering this pump concept is to evaluate the efficiency compared with existing wind turbines. If the concept is not competitive, it will not be of any interest, thus power losses needs to be minimized. E.g. the efficiency is directly dependent on the in- and outlet valves of the cylinders along with the friction inside the components of the pump so the power loss in these needs to be addressed. PMC Servi suggest using a standard NG40 valve for in and outlet valve of each cylinder. The following chapter analyses the effects of using these valves, and determines the subjects and areas of improvement.

Description	Value	Unit
Rotational speed of wind turbine	10	$[rpm]$
Rotor height	100	$[m]$
Rotor diameter	120	$[m]$
Nacelle mass	300-400	$[t]$
Cylinder diameter	0.450	$[m]$
Cylinder stroke	0.580	$[m]$
Cylinder volume	92.2	$[l]$
Outside diameter of pump	3	$[m]$
Nominal flow of PMC pump	12,656	$[l/min]$
Diameter of inlet pipe	0.254 (10in)	$[m]$
Diameter of outlet port	0.3048 (12in)	$[m]$
Working pressure difference of motor	250	$[bar]$
Volumetric efficiency	98	%
Total efficiency of the pump	96	%

Table 1.3.1: Properties of *PMC Servi* pump, all values are extracted from the article: [Ilsøy A., 2010].

Non-linear Pump Model²

To evaluate the PMC Servi pump, a non-linear model which describes the mechanical and hydraulic parts is formed. Furthermore when the non-linear model is completed it can be applied to evaluate other valve types. The model is based on the information provided by the PMC Servi article, [Ilsøy A., 2010]. This chapter describes this non-linear model, including both the mechanical and hydraulic components.

2.1 Mechanical Model

This section describes the dynamics and kinematics of the rotational movement of the shaft and the linear translation of the pistons. Initially one piston will be described, later this one-piston model will be expanded to a full mechanical description of the pump with 14 cylinders.

The rotating eccentric shaft, and the piston, cf. Figure 2.1.1 and 2.1.2 consists of three links, with two revolute joints in points O and B , and one revolute and translational joint in A . Note that Figure 2.1.1 only illustrates one of the two eccentric shafts each with seven pistons. When implementing this in the full non-linear model, the eccentric shafts will be modelled as a single eccentric shaft with 14 pistons.

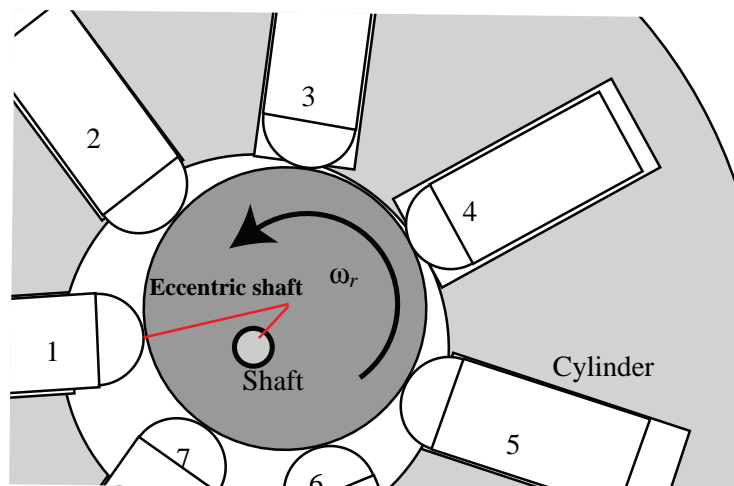


Figure 2.1.1: Kinematic mapping - Red lines indicate the links on Figure 2.1.2a.

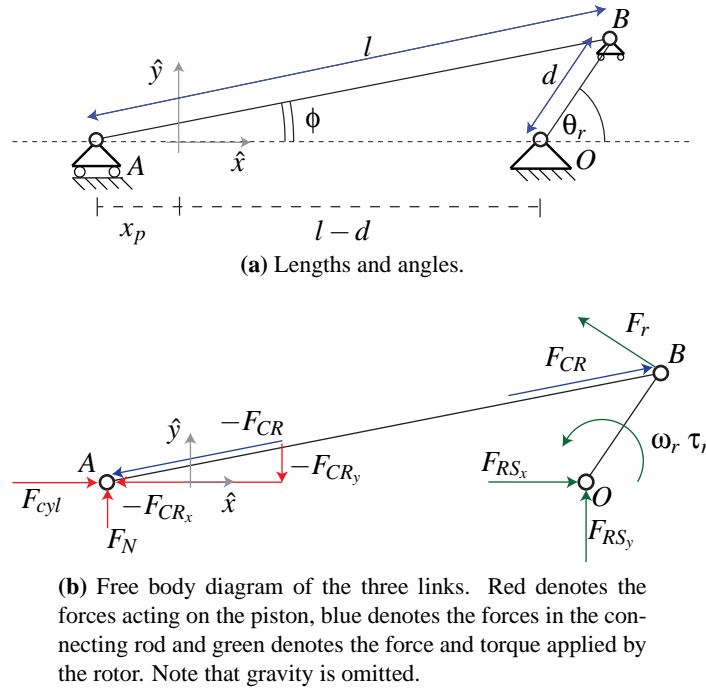


Figure 2.1.2: Kinematic and free body diagram of one piston and shaft.

The forces of Figure 2.1.2b will be described further in the following section.

2.1.1 Dynamics of One Piston

A force equilibrium is established around the piston as illustrated on Figure 2.1.2b in Equation 2.2

$$\begin{aligned} M_p \ddot{\vec{x}}_p &= \vec{F}_{cyl} + (-\vec{F}_{CR}) + \vec{F}_N \\ M_p \ddot{x}_p \hat{x} &= F_{cyl} \hat{x} - (F_{CR} \cos(\phi) \hat{x} + F_{CR} \sin(\phi) \hat{y}) + F_N \hat{y} \end{aligned} \quad (2.1)$$

where:	M_p	Mass of the piston
	$\ddot{\vec{x}}_p$	Acceleration vector of the piston
	\vec{F}_{cyl}	Force acting on the piston due to the pressure in the cylinder.
	\vec{F}_{CR}	Force in the connecting rod
	\vec{F}_N	Normal force
	\hat{x}	Unit vector in the x-direction
	\hat{y}	Unit vector in the y-direction

This results in two equations for the x - and y -direction respectively, as elaborated in Equation 2.2

$$\begin{aligned}
 0 &= (F_{cyl} - F_{CR} \cos(\phi) - M_p \ddot{x}_p) \hat{x} + (F_N - F_{CR} \sin(\phi)) \hat{y} \\
 0 &= F_{cyl} - F_{CR} \cos(\phi) - M_p \ddot{x}_p \quad \vee \quad 0 = F_N - F_{CR} \sin(\phi) \\
 F_{CR} &= \frac{F_{cyl} - M_p \ddot{x}_p}{\cos(\phi)} \quad \vee \quad F_{CR} \sin(\phi) = F_N
 \end{aligned} \tag{2.2}$$

In order to compute the force in the connecting rod, F_{CR} , the cylinder force, F_{cyl} , and the acceleration of the piston, \ddot{x}_p , has to be determined. This will be done in the following and in section 2.1.3 respectively.

The cylinder force originates from the pressure inside the cylinder acting on the area, A_p of the piston which then causes a force as described by Equation 2.3

$$\vec{F}_{cyl} = P_C A_p \hat{x} \tag{2.3}$$

where: P_C Cylinder pressure
 A_p Area of the piston

The cylinder pressure, P_C , will be further elaborated in section 2.2

2.1.2 Torque Equilibrium

To connect the dynamics of the piston with that of the rotor, a torque equilibrium of the rotating shaft is necessary. In this section the torque produced by all 14 pistons is summed and the dynamics of the shaft is established. Equation 2.4 is the torque equilibrium of the shaft.

$$J_r \dot{\vec{\omega}}_r = \vec{\tau}_r + \sum_{i=1}^{14} \vec{\tau}_{CR_i} \tag{2.4}$$

where: J_r Moment of inertia of all the rotating parts connected to the shaft. Excluding the inertia of the eccentric shaft
 $\dot{\vec{\omega}}_r$ Angular acceleration vector of the rotor
 $\vec{\tau}_r$ Rotor torque
 $\vec{\tau}_{CR_i}$ Force on piston i through the kinematics, converted to a torque on the shaft

In order to determine $\vec{\tau}_{CR_i}$, a coordinate system is placed in point O as illustrated in Figure 2.1.3. The vector \vec{OB}_i is considered along with the force in the connecting rod \vec{F}_{CR_i} as presented in Equation 2.5, with $|\vec{OB}_i| = d$ and $|\vec{F}_{CR_i}| = F_{CR_i}$.

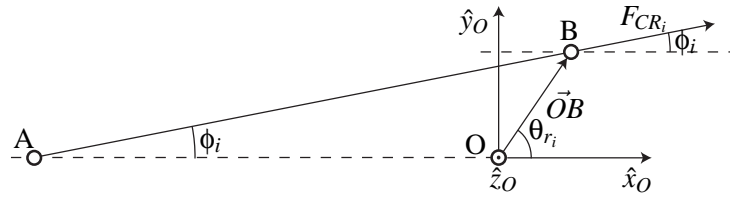


Figure 2.1.3: The force in the connecting rod, F_{CR_i} , displayed along with the vector \vec{OB}_i and their respective angles to the x-axis.

$$\begin{aligned}
 \vec{\tau}_{CR_i} &= \vec{OB}_i \times \vec{F}_{CR_i} \\
 &= d \begin{bmatrix} \cos \theta_{r_i} \\ \sin \theta_{r_i} \\ 0 \end{bmatrix} \times F_{CR_i} \begin{bmatrix} \cos \phi_i \\ \sin \phi_i \\ 0 \end{bmatrix} \\
 &= d F_{CR_i} \sin(\phi_i - \theta_{r_i}) \hat{z}_O
 \end{aligned} \tag{2.5}$$

The implementation of this torque equilibrium is done by implementing a velocity and acceleration controller which ensures that the required torque is available in order to maintain the reference angular velocity, ω_{ref} .

This is a simplification of a real wind turbine; The controller in an actual wind turbine has a more advanced control strategy, where it adjusts the pitch angle of the blades in such a way that a specific power is maintained. The power is a function of torque and angular velocity, hence the controller has two variables to adjust when a power output is chosen [Muljadi et al., 1998]. This controller can be quite complex and is not included in this project. Instead two PI-controllers are implemented as illustrated in Figure 2.1.4.

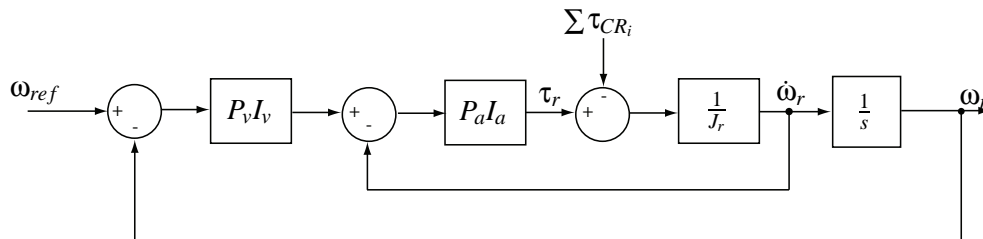
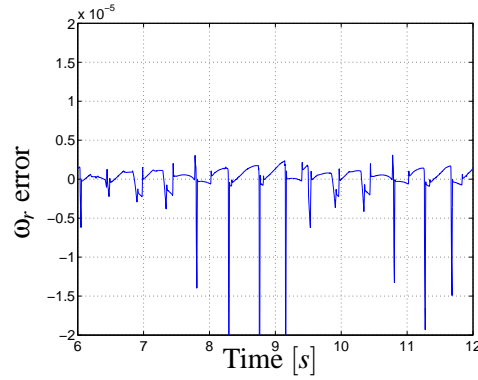


Figure 2.1.4: Velocity and acceleration controller.

A constant angular velocity is initially chosen as ω_{ref} and, as mentioned, the outer PI-Controller, denoted $P_v I_v$, is a velocity controller ensuring constant angular velocity. The inner PI-controller, denoted $P_a I_a$ controls the acceleration which is desired to be zero. These two controllers ensures that the wind always delivers the necessary torque, τ_r , to the shaft. The coefficients of the controllers are given in Table 2.1.1. The size of the values are relatively high, this is to ensure an almost constant angular velocity such that the wind delivers the necessary torque instantaneously. The numerical error, ω_{error} , is kept below $\leq 2 \cdot 10^{-5} [rad/s]$, as presented on Figure 2.1.5.

Parameter	Value
P_a	0
I_a	115926000
P_v	90
I_v	4058

Table 2.1.1: Parameters for the PI-controller.**Figure 2.1.5:** Simulated angular velocity of the shaft, with the reference velocity of 1.0472 [rad/s] subtracted.

The simplification of using this relatively powerful velocity and acceleration controller is legitimate in this analysis. Since the focus of the project is on designing the pump, the control of the rotor blades are assumed to be effective such that the angular velocity is kept constant.

2.1.3 Kinematic mapping

To express the position, velocity, and acceleration of the piston from the angle θ_r , the angle ϕ on Figure 2.1.2a is calculated as a function of the rotational angle of the shaft, θ_r .

$$\phi(t) = \sin^{-1} \left(\frac{\sin(\theta_r(t))}{l} d \right) \quad (2.6)$$

Note that θ_r is a function of time and angular velocity hence:

$$\theta_r(t) = \omega_r t + c\theta_{int} \quad (2.7)$$

Where c is the chosen cylinder no. subtracted by one. θ_{int} is the angle between the cylinders, and ω_r is the rotational velocity.

Now that ϕ is defined from θ_r , a relation for \dot{x}_p as a function of the current rotor angle θ_r and velocity ω_r can be defined. Figure 2.1.6b illustrates the velocity vectors of the cylinder and of the eccentric shaft.

2. Non-linear Pump Model

The velocity of the connecting rod can be considered as follows. The translational velocity of point A, \vec{V}_A , is the vector sum of the translational portion, \vec{V}_B , and the rotational portion, $\vec{V}_{A/B}$, of the velocity of the connecting rod with point B as a reference point, cf. Figure 2.1.6a.

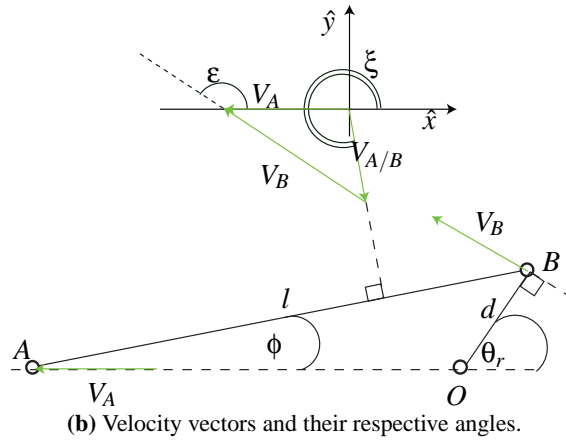
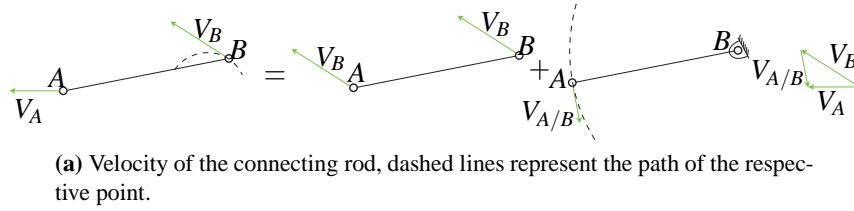


Figure 2.1.6: Velocity diagram and the respective angles between the vectors and the \hat{x} -axis. Velocity vectors are marked with green.

Figure 2.1.6a yields

$$\vec{V}_A(t) = \vec{V}_B(t) + \vec{V}_{A/B}(t) \quad (2.8)$$

From Figure 2.1.6b and the law of sines, Equation 2.9 can be established, note that the sign of $V_{A/B}(t)$ changes.

$$V_{A/B}(t) = \frac{V_B(t) \sin(\epsilon(t))}{\sin(\xi(t))} \quad (2.9)$$

To find the velocity of the piston which only has an x -component, Equation 2.8 can be applied on the x -components of all three vectors with the angles as given in Figure 2.1.6b such that by substituting $\dot{x}_p(t) = -V_A(t)$:

$$\dot{x}_p(t) = -\cos(\epsilon(t)) V_B(t) + \cos(\xi(t)) V_{A/B}(t) \quad (2.10)$$

The angles on Figure 2.1.6b is given as

$$\varepsilon(t) = \frac{\pi}{2} + \theta_r(t) \quad (2.11)$$

$$\xi(t) = \frac{3\pi}{2} + \phi(t) \quad (2.12)$$

By substituting Equations 2.6, 2.7, 2.9, 2.11, and 2.12 into Equation 2.10 and differentiating, the expression for the acceleration of the piston is found to:

$$\begin{aligned} \ddot{x}_p = & \cos(\omega_r(t)t + \theta_{int}) \left(\left(\frac{d}{dt} \omega_r(t) \right) t + \omega_r(t) \right) d \omega_r(t) + \sin(\omega_r(t)t + \theta_{int}) d \left(\frac{d}{dt} \omega_r(t) \right) \\ & - \frac{\cos(2\omega_r(t)t + 2\theta_{int}) \left(\left(\frac{d}{dt} \omega_r(t) \right) t + \omega_r(t) \right) d^2 \omega_r(t) + \frac{1}{2} \sin(2\omega_r(t)t + 2\theta_{int}) d^2 \left(\frac{d}{dt} \omega_r(t) \right)}{l \sqrt{1 - \frac{\sin(\omega_r(t)t + \theta_{int})^2 d^2}{l^2}}} \\ & - \frac{\sin(\omega_r(t)t + \theta_{int})^2 d^4 \omega_r(t) \cos(\omega_r(t)t + \theta_{int})^2 \left(\left(\frac{d}{dt} \omega_r(t) \right) t + \omega_r(t) \right)}{l^3 \left(1 - \frac{\sin(\omega_r(t)t + \theta_{int})^2 d^2}{l^2} \right)^{3/2}} \end{aligned} \quad (2.13)$$

The expression of the velocities given in Equation 2.10 can also be integrated to express the position of the piston. By inserting a constant angular velocity of $\omega_r(t) = 1.04[\text{rad/s}]$, the distances $d = 0.29[\text{m}]$ and $l = 0.7[\text{m}]$ and by choosing cylinder #1 by setting $\theta_{int} = 0$, the positions, velocities, and accelerations presented in Figure 2.1.7 are obtained.

The length, d , is defined as half the stroke length of $0.58[\text{m}]$. The length, l , is the radius of the eccentric shaft and is not defined in the PMC Servi article [Ilsøy A., 2010] so a value has been chosen to $l = 0.7[\text{m}]$.

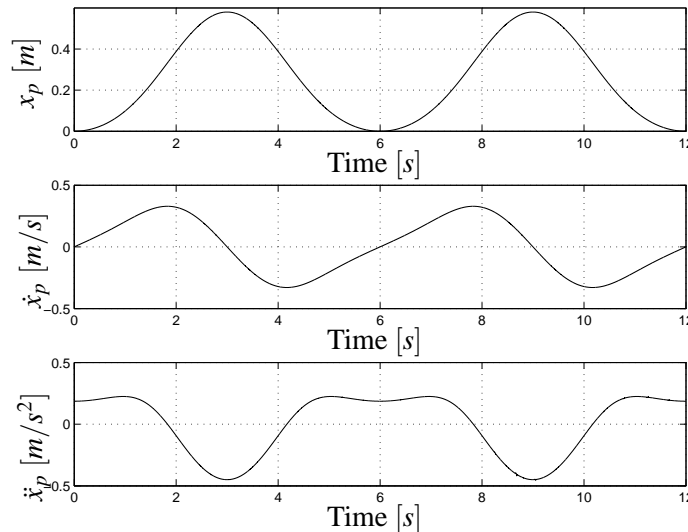


Figure 2.1.7: Position, velocity, and acceleration of piston #1.

2.2 Hydraulic Model

This section describes the hydraulic equations of the cylinders in the radial piston pump, the valves, and the pressures in the tube from the pump to the motor. As described earlier the pump consists of 14 cylinders driven by a rotating shaft at constant angular velocity equal to the rotor speed, ω_r . This forces the pistons to move as described in Equation 2.13. Figure 2.2.1 illustrates the flows and pressures in one cylinder # 1, which will be described thoroughly in this section along with the assumptions.

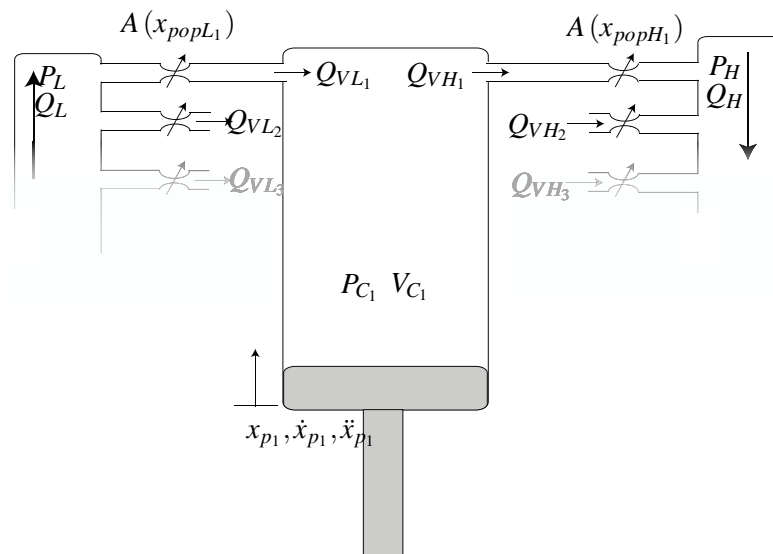


Figure 2.2.1: Hydraulic cylinder with valves and tubes. The fading tubes on each side of the cylinder denotes the in- and outlet valve for cylinder #2 and up.

where:	P_L	Pressure in the low pressure tube
	P_H	Pressure in the high pressure tube
	Q_{VL1}	Flow through low-pressure valve
	Q_{VH1}	Flow through high-pressure valve
	P_{C1}	Pressure inside the chamber of cylinder #1
	x_{p1}	Movement of the piston in cylinder #1

Assumptions:

- Constant angular velocity of the wind turbine shaft with infinite torque. This is done by implementing a velocity and acceleration controller, described in section 2.1.2.
- Equal distributed pressure inside the cylinder chambers.

- No leakage flows in cylinders and valves.

In order to model the two valves which govern the in and outlet flow of the cylinder, a basic understanding of the two valves is necessary. An NG40 cartridge valve from *Parker Hannifin* is chosen as the initial valve applied in the system. This particular valve is constructed such that a pilot pressure in port X, can be chosen from either port A or B of the valve as illustrated in Figure 2.2.2. The pressure of port A works on area A_A , the pressure of port B on area A_B , and likewise for port X and A_X . The areas of the poppet are given in Figure 2.2.3.

The construction of the valve enables it to open when the pressure difference between port A and B is in favour of opening, depending on which pilot pressure has been selected.

In the outlet valve, marked with index v_H , the pressure in the high pressure tube, P_H , is chosen as the pilot pressure. Thus the high pressure valve opens when the pressure in the cylinder, P_C , is larger than the pressure in the high pressure tube. Similarly for the inlet valve, marked with index v_L , the cylinder pressure is chosen as the pilot pressure, thus the valve opens when the pressure in the low pressure tube, P_L , exceeds that of the cylinder.

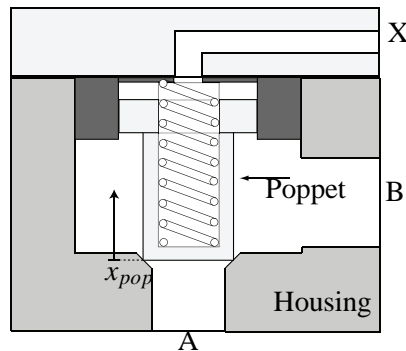
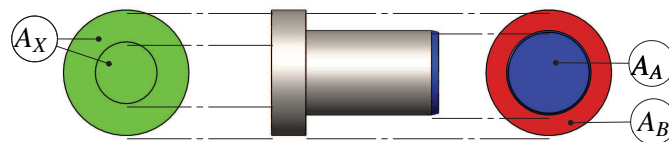
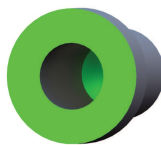


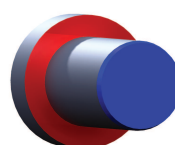
Figure 2.2.2: Principal diagram of the valve, including valve housing, top cover, and spring.



(a) Pressure areas.



(b) Topview



(c) Bot-tomview

Figure 2.2.3: Poppet.

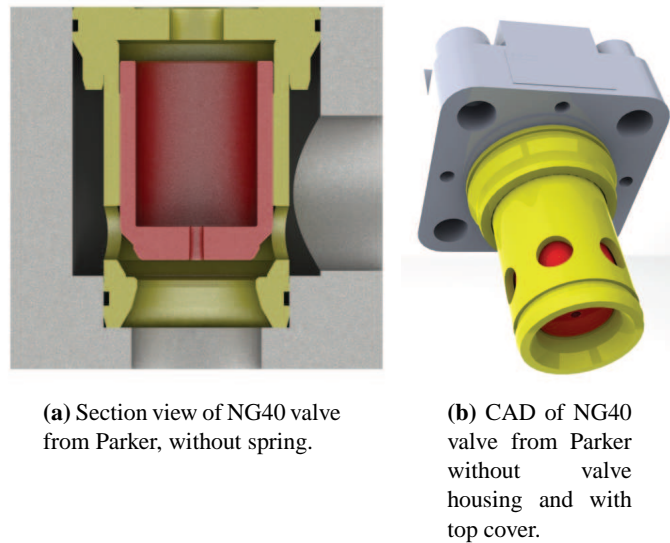


Figure 2.2.4: The actual valve construction in opened position; poppet is marked with red and sleeve with yellow. Figure 2.2.4a illustrates a section view of the actual NG40 valve and Figure 2.2.4b illustrates a 3D-view of the NG40 valve.

Figure 2.2.2, 2.2.3 and 2.2.4 illustrates the simplified and the actual NG40 valve. Several differences between the two exists:

- Opening area - The opening area of the simplified version is modelled as a sharp-edged poppet in contact with a chamfered seat. The actual poppet and seat are round edged.
- The sleeve of the actual poppet has six holes all the way around the poppet, creating a restriction compared to the simplified version. In addition the actual valves has non-cylindrical inlet pipe, which is not equal to the simplified version of the valve.
- The poppet of the actual valve has a hole in the centre. This is often applied as a direct connection to port A, and also works as a damping orifice. If the pilot pressure is chosen from a different source, e.g. port B, the hole in the poppet is sealed or alternatively a different poppet is inserted. In the non-linear model, the pilot pressure is always chosen from Port B, thus the orifice in the poppet is not used and sealed.

The effect of these assumptions is not analysed in this part of the project, however, the opening area and the holes in the sleeve will be examined by means of CFD in section 3.3

2.2.1 The Inlet Valve

The valves are modelled as orifices and the relation between pressure difference and flow is given by the orifice equation as presented in Equation 2.14 [Andersen and Hansen, 2004]

$$Q = C_d A(x_{pop}) \sqrt{\frac{2}{\rho} (P_1 - P_2)} \quad (2.14)$$

where: ρ Density of oil
 P_1 Pressure upstream of orifice
 P_2 Pressure downstream of orifice
 $A(x_{pop})$ Opening area of the orifice
 C_d Discharge coefficient

In the case of the inlet valve for cylinder #1 the orifice equation thus yields

$$Q_{VL_1} = C_d A_{L_1}(x_{pop_1}) \sqrt{\frac{2}{\rho} (P_L - P_{C_1})} \quad (2.15)$$

The area function $A_{L_1}(x_{pop_1})$ will be derived later in section 2.2.3.6.

2.2.2 The Outlet Valve

The outlet valve is modelled as:

$$Q_{VH_1} = C_d A_{H_1}(x_{pop_1}) \sqrt{\frac{2}{\rho} (P_{C_1} - P_H)} \quad (2.16)$$

The area function $A_{H_1}(x_{pop_1})$ will also be derived in section 2.2.3.6.

2.2.3 Force Equilibrium of the Seat Valve

A free body diagram of the poppet is shown in Figure 2.2.5 and from this an equilibrium of forces can be established

$$M_{pop} \ddot{x}_{pop} \hat{x} = \vec{F}_g + \vec{F}_{P_A} + \vec{F}_{P_B} + \vec{F}_{P_X} + \vec{F}_{spr} + \vec{F}_{fl} + \vec{F}_{fr} \quad (2.17)$$

where: M_{pop} Mass of the poppet
 \ddot{x}_{pop} Acceleration of the poppet

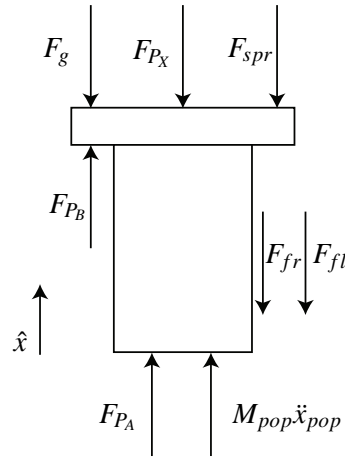


Figure 2.2.5: Free body diagram of the poppet in the cartridge valve.

\vec{F}_g	Gravitational force
\vec{F}_{P_A}	Force exerted by the pressure at port A
\vec{F}_{P_B}	Force exerted by the pressure at port B
\vec{F}_{P_X}	Force exerted by the pressure at the port X
\vec{F}_{spr}	Spring force
\vec{F}_{fl}	Flow forces
\vec{F}_{fr}	Friction forces

These forces are described in the following subsections.

2.2.3.1 Gravitational force, \vec{F}_g

Since the pump is constructed as a radial pump the gravitational force exerted on the poppet varies with the angle from vertical position and the force \vec{F}_g can thus be described by Equation 2.18

$$\vec{F}_g = M_{pop}g \cos(\theta_{int})\hat{x}_i \quad (2.18)$$

where:	g	Gravitational acceleration
	θ_{int}	Angle from horizontal position
	\hat{x}_i	Unit vector in cylinder #i

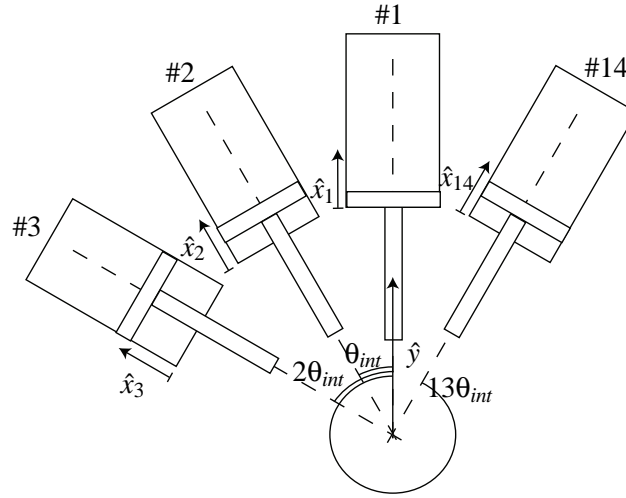


Figure 2.2.6: Position of the cylinders with each individual cylinder denoted by their respective number such that cylinder #1 is aligned with the vertical axis, \hat{y} , cylinder #2 is positioned in an angle, θ_{int} , from \hat{y} , cylinder #3 is positioned at $2\theta_{int}$ and cylinder #14 is positioned at $13\theta_{int}$ from \hat{y} .

2.2.3.2 \vec{F}_{P_A} , \vec{F}_{P_B} , and \vec{F}_{P_X}

The force exerted from the pressures in the cylinder, low pressure tube, and in the high pressure tube on the poppet can be described by

$$\vec{F}_{P_A} = A_A P_A \hat{x}_{pop} \quad (2.19)$$

$$\vec{F}_{P_B} = A_B P_B \hat{x}_{pop} \quad (2.20)$$

$$\vec{F}_{P_X} = A_X P_X (-\hat{x}_{pop}) \quad (2.21)$$

where: P_A Pressure at port A, $P_A = P_L$ for inlet valve and $P_A = P_C$ for outlet valve.

P_B Pressure at port B, $P_B = P_C$ for inlet valve and $P_B = P_H$ for outlet valve.

P_X Pilot pressure, $P_X = P_C$ for inlet valve and $P_X = P_H$ for outlet valve.

The areas, A_A , A_B , and A_X , applied in the equations are presented in Figure 2.2.3a.

2.2.3.3 Spring Force, \vec{F}_{spr}

The spring is distorted a predetermined length, x_{pop*} . This is thus accounted for in the equation for the spring force shown in Equation 2.22

$$\begin{aligned} \vec{F}_{spr} &= k_{spr}(x_{pop*} + x_{pop})(-\hat{x}_{pop}) \\ &= -k_{spr}x_{pop*}\hat{x}_{pop} - k_{spr}x_{pop}\hat{x}_{pop} \end{aligned} \quad (2.22)$$

2. Non-linear Pump Model

where: k_{spr} Spring constant
 x_{pop*} Spring distortion

2.2.3.4 Flow Force, \vec{F}_{fl}

The steady-state flow force can be described by Equation 2.23 [Andersen and Hansen, 2003].

$$\vec{F}_{fl} = -2C_d A(x_{pop}) (P_1 - P_2) \cos(\alpha_j) \hat{x}_{pop} \quad (2.23)$$

where: P_1 Upstream pressure, $P_1 = P_L$ for the inlet valve and $P_1 = P_{C_i}$ for the outlet valve in cyl. # i
 P_2 Downstream pressure, $P_2 = P_{C_i}$ for the inlet valve and $P_2 = P_H$ for the outlet valve in cyl. # i
 α_j Jet angle of the fluid.

The steady-state flow force is caused by a change in the momentum of the fluid when moving through the orifice. The transient flow force is induced by changing the position of the spool and hereby changing the volume, which creates a transient flow rate until the new steady-state conditions are established [Watton, 2009]. The transient flow force is not included in this calculation and is neglected as \dot{x}_{pop} is expected to be low.

2.2.3.5 Viscous Friction Force, \vec{F}_{fr}

The friction force includes viscous friction and is given by

$$\vec{F}_{fr} = \kappa \dot{x}_{pop} (-\hat{x}_{pop}) \quad (2.24)$$

where: κ Friction coefficient

The viscous friction coefficient, κ , originates from the materials used, the surface finish, the oil, and a number of other factors and is usually determined empirically. This is not possible in a non-realised model and thus it is set to a value of $200[Ns/m]$. This value is estimated experimentally in an earlier project regarding an over-center valve and is considered as a *good guess* [Jensen et al., 2008].

2.2.3.6 Area Function

The opening areas of the orifices in both the inlet and the outlet valve are modelled as the opening areas of a sharp-edged valve, cf. Figure 2.2.7. The functions $A_L(x_{pop})$ and $A_H(x_{pop})$ are derived

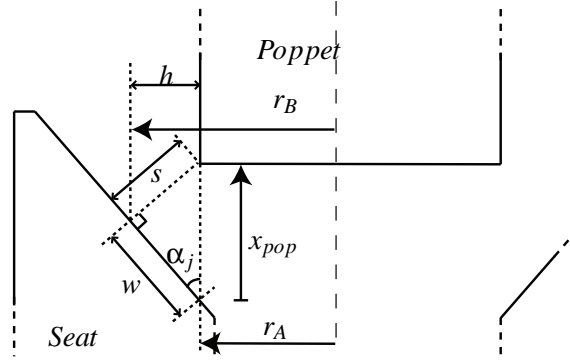


Figure 2.2.7: Illustration of a sharp-edged valve with denominations of the different parameters utilised to derive the area functions.

by analysing the geometry of the valve opening. The opening area will be in the form of a cone frustum as illustrated in Figure 2.2.8. To determine the flows through the orifices, the function which describes the area with respect to the stroke, x_{pop} , is derived. The area of a cone frustum is

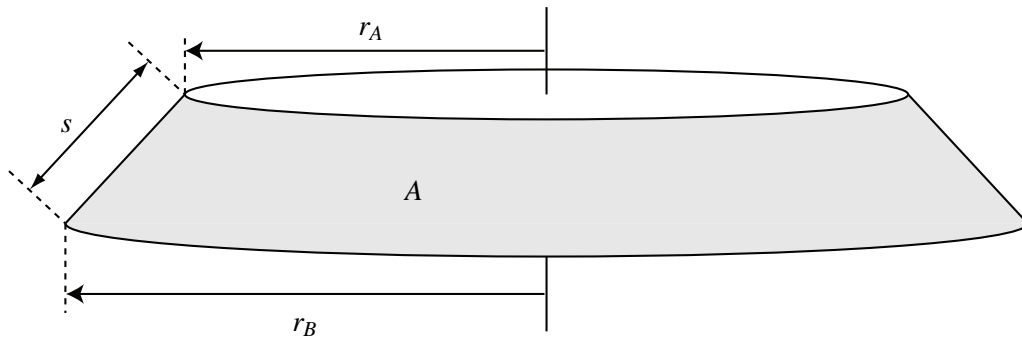


Figure 2.2.8: Cone frustum with area denomination.

given by Equation 2.25

$$A = \pi s(r_B + r_A) \quad (2.25)$$

where:

s	The distance between the two circular peripheries as noted on Figure 2.2.8
r_A	Radius of the large end of the cone frustum as noted on Figure 2.2.8
r_B	Radius of the small end of the cone frustum as noted on Figure 2.2.8

A right triangle as in Figure 2.2.7, with x_{pop} being the hypotenuse and s and w being the catheti, is constructed in order to determine the length of s and w :

$$s(x_{pop}) = x_{pop} \sin(\alpha_j) \quad (2.26)$$

$$w(x_{pop}) = x_{pop} \cos(\alpha_j) \quad (2.27)$$

2. Non-linear Pump Model

where: α_j Angle of the orifice as depicted on Figure 2.2.7

By analysing the area of the triangle the height, h , of the triangle can be found as:

$$A = \frac{1}{2}ws = \frac{1}{2}hx_{pop} \Rightarrow h = \frac{ws}{x_{pop}} \quad (2.28)$$

By substituting Equations 2.26, 2.27, and 2.28 into Equation 2.25 and utilising that $r_B = r_A + h$ the area function for a sharp-edged valve opening is obtained.

$$A(x_{pop}) = \pi x_{pop} \sin(\alpha_j)(2r_A + x_{pop} \cos(\alpha_j) \sin(\alpha_j)) \quad (2.29)$$

This area function is applied in Equations 2.14, 2.16, and 2.23.

2.2.3.7 Cylinder Chamber

The cylinder chamber volume varies depending on the position of the rotor and thus the position of the piston. By utilising the continuity equation, the pressure of the cylinder chamber, P_{C_1} , can be determined as illustrated in Figure 2.2.9. The continuity equation is given as:

$$Q_{VL_1} - Q_{VH_1} = A_p \dot{x}_{p_1} + \frac{V_{p0} + A_p x_{p_1}}{\beta} \dot{P}_{C_1} \quad (2.30)$$

where: A_p Pressure area of the piston
 V_{p0} Minimum volume of cylinder
 β Bulk modulus

2.2.4 Full Model

By combining the equations derived in the preceding sections it is possible to construct a model describing one cylinder with an inlet and outlet valve. This is presented in Figure 2.2.9 as a block diagram to illustrate how the different equations interact.

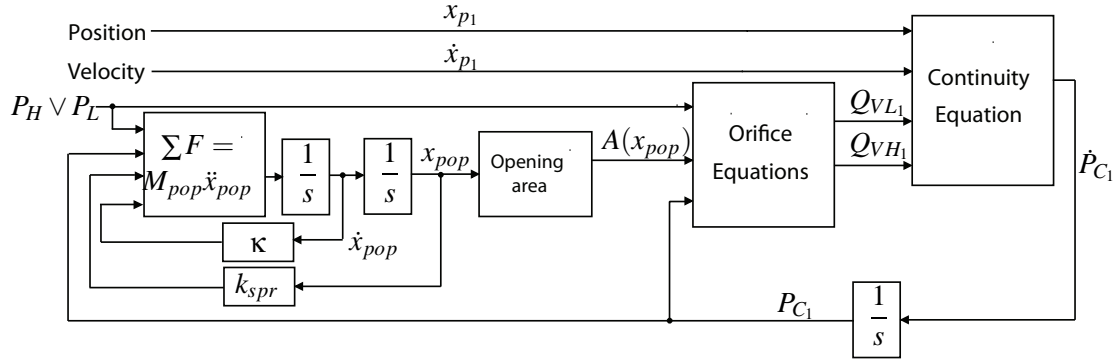


Figure 2.2.9: Relation between the equations of cylinder # 1

By copying the model for one cylinder 14 times, a model for all cylinders is obtained. The input to each specific cylinder with valves is the mechanical movement of the same specific piston derived in section 2.1. However, as each piston moves with a phase difference from the former piston the input of velocity and position is phase shifted $\frac{2\pi}{14}$ compared to the former piston.

In order to calculate the pressure in the high pressure tube, a continuity equation is established for this volume, with the assumption that the pressure is evenly distributed in the entire volume. This assumption is valid as the focus for this project is the design of the pump. In truth there will be a higher pressure at ground level due to the difference in height, and the pressure will not instantaneously adjust in the whole volume but will propagate along transmission lines.

$$\begin{aligned} \sum_{i=1}^{14} (Q_{VH_i}) - Q_M &= \dot{V}_H + \frac{V_H}{\beta} \dot{P}_H \quad | \quad \dot{V}_H = 0 \\ &= \frac{V_H}{\beta} \dot{P}_H \end{aligned} \quad (2.31)$$

where: Q_M Flow through the motor
 V_H Complete volume of the high pressure tube
 \dot{V} Gradient of the volume

To analyse the pressure in the high pressure tube, the flow out of the volume has to be determined. This flow is the flow through the motor which converts potential energy in the oil to kinetic energy. In this model the motor is modelled as an orifice with an adjustable opening area in order to set the average working pressure of the high pressure tube, thus the orifice equation is applied:

$$Q_M = C_d A_M \sqrt{\frac{2}{\rho} (P_H - P_t)} \quad (2.32)$$

2. Non-linear Pump Model

where: A_M Area of the orifice
 P_t Pressure in the tank

P_t is applied as a tank pressure in order to simplify the model. This simplification does not reflect the actual system, but fits the purpose of this model: To determine the behaviour of the pump without any focus on the motor. The equations are presented in a block diagram on Figure 2.2.10.

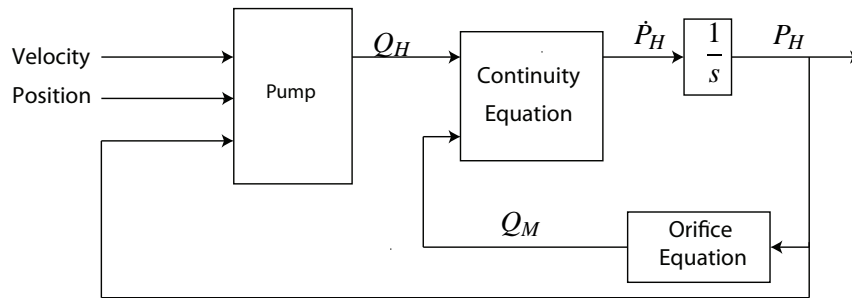


Figure 2.2.10: Block diagram of the equations governing the pressure in the high pressure tube.

2.2.5 Variable Stiffness

When working with high pressure differences between P_L and P_H , it is often necessary to incorporate variable stiffness. This is done by making bulk modulus a function of the current pressure in the volume. The function is described in appendix A.1.

2.3 Simulation

This section contains an analysis of the system with a standard NG40, NG50, NG63, NG80, and NG100 valve from Parker applied as both the high and low pressure valve respectively. Also the efficiency of the hydraulic part of the pump for each applied valve is calculated. All the specifications of the valves, except the mass of the poppet, utilised in the model have been obtained from the datasheets provided by Parker and are presented in Table 2.3.1. The mass of the poppet has been obtained by drawing the poppet in a CAD program from the technical drawings also received from Parker, and estimating the mass from this.

Valve Size	k_{spr}	x_{pop*}	M_{pop}	Maximum Stroke	A_A	A_B	A_X
NG40	430[N/m]	32.3[mm]	0.36[kg]	15.0[mm]	1075[mm ²]	1.2A _A	2.2A _A
NG50	600[N/m]	38.5[mm]	0.60[kg]	20.0[mm]	2206[mm ²]	0.6A _A	1.6A _A
NG63	790[N/m]	51.6[mm]	1.4[kg]	25.0[mm]	3318[mm ²]	0.9A _A	1.9A _A
NG80	1060[N/m]	56.7[mm]	2.1[kg]	30.5[mm]	5281[mm ²]	0.8A _A	1.8A _A
NG100	1370[N/m]	61.1[mm]	3.0[kg]	39.0[mm]	8825[mm ²]	0.8A _A	1.8A _A

Table 2.3.1: The specifications of the valves from Parker applied in the model.

2.3.1 Applied Simplifications

When the simulation is run, a set of simplifications is applied. A selection of these are described in the following.

The value of the discharge coefficient applied in these simulations is based on the results obtained by [Sørensen, 1999]. Here, contrary to spool valves [Andersen and Hansen, 2003], it was discovered that when dealing with poppet valves like the valves in question in this report, the discharge coefficient could be approximated to 0.8 rather than 0.6 as is usual the case. Based on this, C_d has been chosen to $C_d = 0.8$. This fits the purpose of these simulations well as means to assess the effect on the system the different valves induce, mainly evaluated on the overall efficiency of the hydraulic components.

The model has been constructed such that, the first cycle of the cylinders initializes the system such that the different variables has found their level. Because of this, the first cycle ($0 - 6[s]$) of the simulation is utilised as an initialisation cycle and the actual system is not studied until the next cycle. All plots and observations regarding the simulations for the different valves are thus also only conducted after $6[s]$. Also, all valves are modelled as sharp-edged valves.

2.3.2 Presentation of the Results

The simulation was run with a standard NG40, 50, 63, 80, and NG100 valve respectively from Parker. All simulations are executed with ODE3-solver with fixed stepsize of $1 \cdot 10^{-6}$. Figure 2.3.1 illustrates the opening area of the in- and outlet valve of cylinder #1.

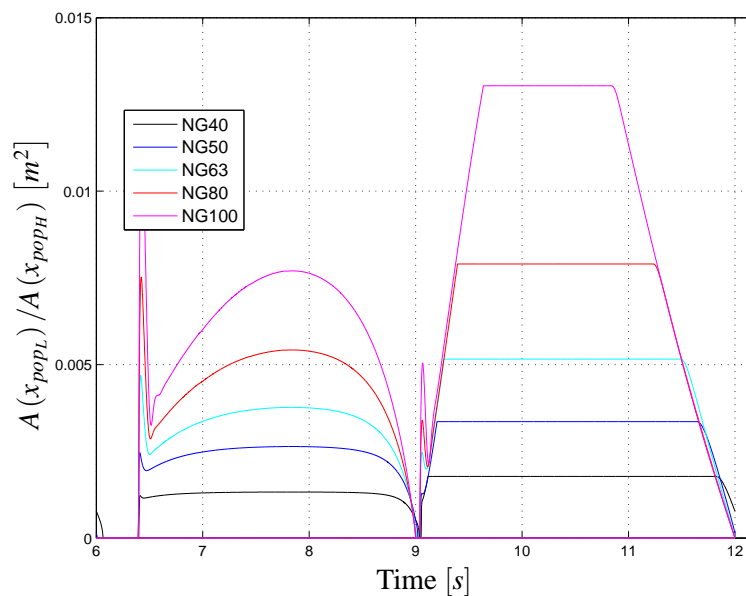


Figure 2.3.1: Valve opening area for both valves of cylinder #1 for NG40, 50, 63, 80, and NG100 valves respectively.

2. Non-linear Pump Model

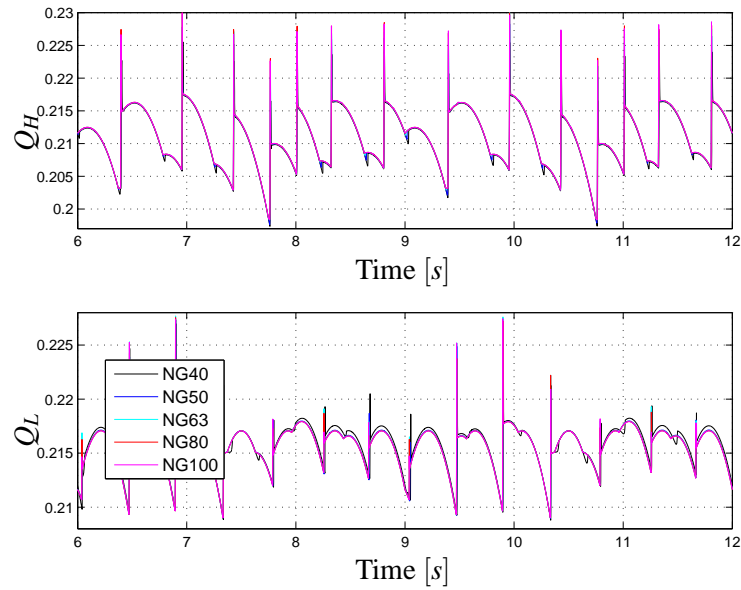


Figure 2.3.2: Flow out and into the pump for NG40, 50, 63, 80, and NG100 valves respectively. Each consisting of the sum of the flow through all the valves on each side of the cylinders.

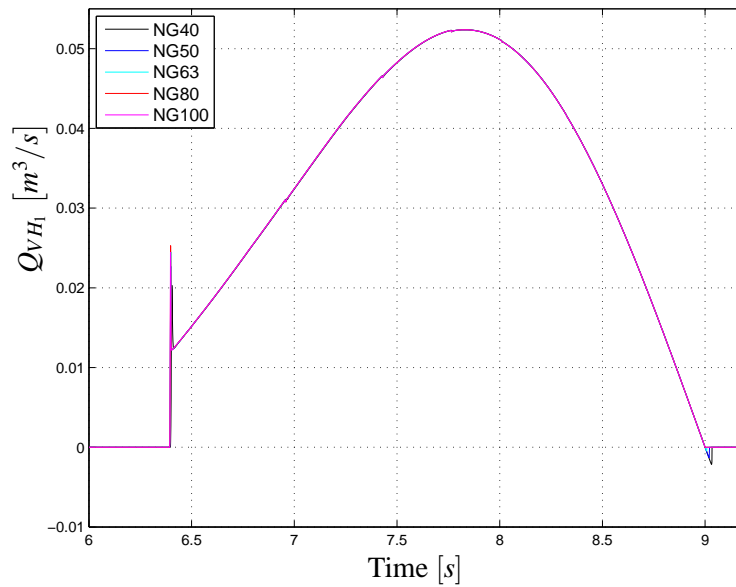


Figure 2.3.3: Flow from one cylinder through the high pressure valve for an NG40, 50, 63, 80, and NG100 valve respectively.

Figure 2.3.3 illustrates the outlet flow of cylinder #1. Because of the nature of the piston movement this flow is very similar for the five valves. This directly influences the total flow out of the pump where the flow from all 14 cylinders are summed as shown in Figure 2.3.2. The resulting pressure in the high pressure tube show fluctuations as depicted in Figure 2.3.4. The pressure in cylinder #1 is also depicted in Figure 2.3.4.

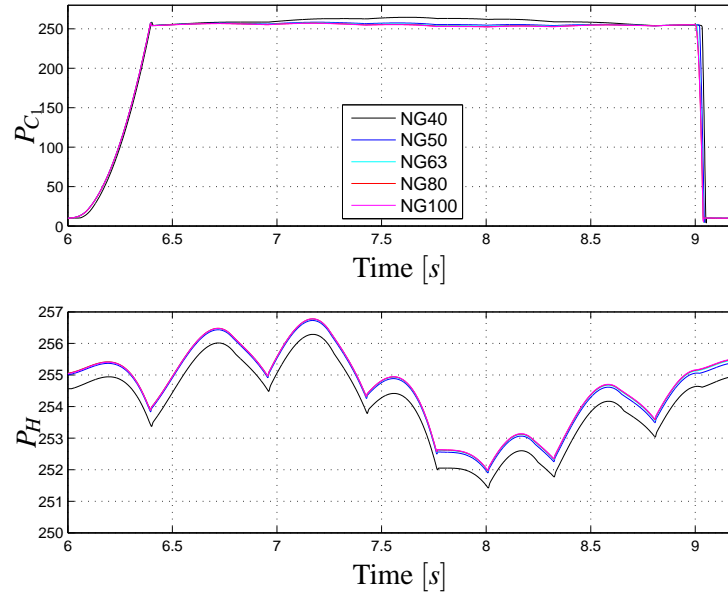


Figure 2.3.4: High pressure and cylinder pressure.

The pressure difference ΔP_{CH} is calculated as

$$\Delta P_{CH} = P_{C_1} - P_H \quad (2.33)$$

This is done for all five valves and is presented in Figure 2.3.5.

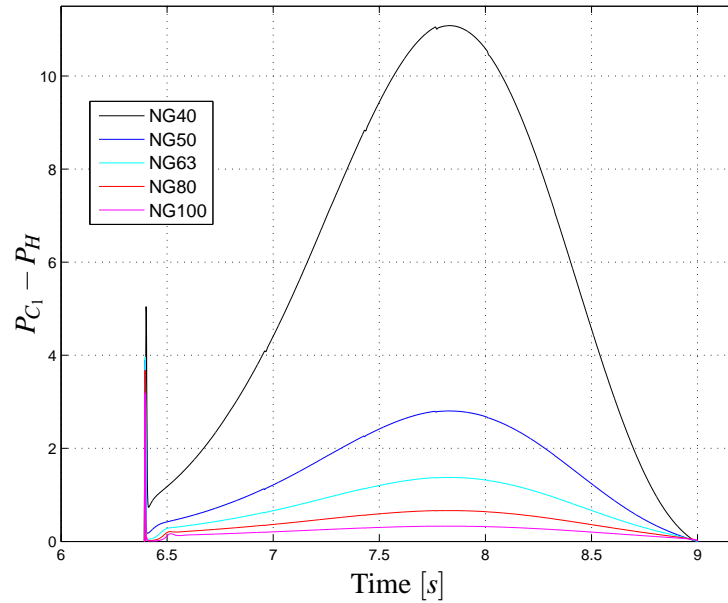


Figure 2.3.5: Pressure difference between P_{C_1} and P_H for an NG40, 50, 63, 80, and NG100 valve respectively.

In order to calculate the efficiency of the pump, the output power of the pump is determined along

2. Non-linear Pump Model

with the total input power. The power is calculated as

$$\mathcal{P} = QP \quad (2.34)$$

so the output power is calculated as:

$$\mathcal{P}_{out} = P_H Q_H \quad (2.35)$$

and the total input power is a sum of the power from the rotor and the power from the fluid through the low pressure valve such that:

$$\mathcal{P}_{in} = P_L Q_L + \tau_r \omega_r \quad (2.36)$$

By applying these equations, it is now possible to establish the efficiency of the systems with the different valves applied:

$$\begin{aligned} \eta &= \frac{\mathcal{P}_{out}}{\mathcal{P}_{in}} \\ \eta_{pump_{NG40}} &= 0.9525 \\ \eta_{pump_{NG50}} &= 0.9837 \\ \eta_{pump_{NG63}} &= 0.9897 \\ \eta_{pump_{NG80}} &= 0.9926 \\ \eta_{pump_{NG100}} &= 0.9941 \end{aligned} \quad (2.37)$$

These are graphically presented in Figure 2.3.6 as a function of the valve inlet diameter.

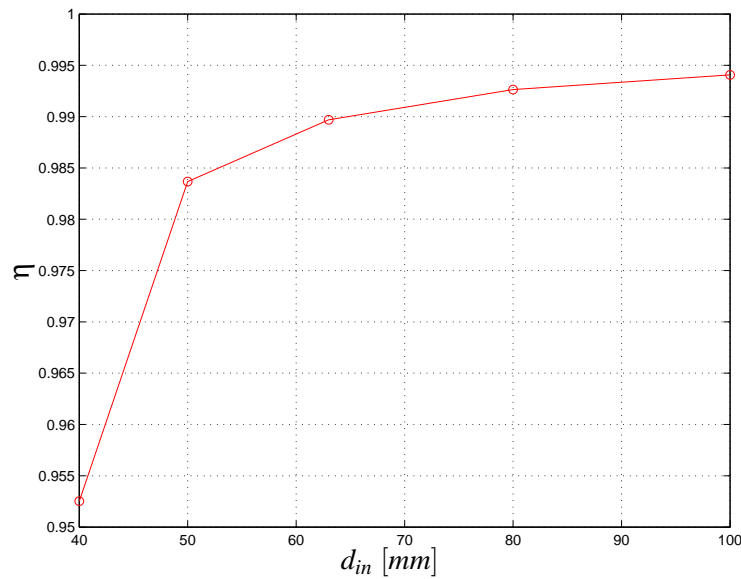


Figure 2.3.6: Efficiency as a function of the inlet diameter

It is noted that these efficiencies does not represent the actual efficiencies as neither leakage nor the mechanical efficiency is taken into account in the model. However, they make it possible to

compare the valves based on the hydraulic components in the pump.

2.4 Problem Analysis and Approach

In Section 2.3 five different sizes of valves has been examined with respect to the efficiency in the pump in which they are applied. The efficiencies increases with increment valve size. This is caused by a smaller pressure difference between the pressure in the cylinder chamber and the pressure in the high pressure tube. It can thus be concluded that this pressure difference has to be minimized in order to obtain a higher degree of efficiency.

As already implied the efficiency can be increased by installing a larger valve. To decide which valve to apply, at least one more parameter has to be taken into consideration. Furthermore there must be a limit to the increment of the size of the valve, due to its sheer size e.g. when the inlet diameter of the valve approaches that of the cylinder or is enlarged. Figure 2.3.6 implies that the gain in efficiency is minor from NG80 to NG100, compared to the gain from NG40 to NG63.

Two possible parameters to take into consideration when choosing the valve size is the weight and the price of the valve. E.g. the cartridge of the NG63(6.9[kg]) valve weighs almost four times that of the NG40(1.8[kg]), and the NG100(24[kg]) weighs almost four times that of the NG63.

All this considered, it can be deemed impossible to produce a pump with an overall efficiency of $\eta_{pump} = 0.96$ with a standard NG40 valve applied on both sides of the cylinder as only the hydraulic part of the pump is modelled. Even without leakage the model only yields an efficiency of $\eta_{pump_{NG40}} = 0.9525$. It might be possible to modify the NG40 valve in order for it to yield a better efficiency, though these modifications applied to a larger valve might also increase the efficiency of the system with this specific valve applied.

In regards to this project a decision was made as to which valve to analyse further. The analyse was based on early calculations which proved that the NG63 valve showed significant improvements of the system. Subsequently the NG80 and the NG100 valve was analysed and these also revealed significant improvements compared to the NG63 valve. However, it was not possible, within the time frame of this project to investigate these valves further.

2.4.1 Demand Specification

From the preceding analysis and the initiating article [Ilsøy A., 2010] the following demands for the valve has been derived.

- Nominal flow from the pump of $0.2 \text{ [m}^3/\text{s}]$ results in a nominal flow of $0.05 \text{ [m}^3/\text{s}]$ through each valve.

2. Non-linear Pump Model

- The working pressure has been selected to a minimum of 250[bar] during pumping.

The main focus in order to obtain a higher efficiency is focused on minimizing the pressure difference across the in- and outlet valves, along with an investigation of the frictions in the mechanical part of the pump and the leakages of the bearings.

2.4.2 Problem Specification

In the problem analysis of the valve design the opening area is derived from a sharp-edged valve, however, the variety of poppets and seats are large. Thus a more thorough examination of the opening area and its performance has to be conducted.

Further development of the hydraulic model is also necessary in order to determine the influence of the specific valve design on the rest of the system. This involves: Expanding the model with leakage flows, including the possible leakage derived from the use of piston rings and slipper pad bearings in order to obtain a more precise efficiency. Also a more thorough investigation of the the pump itself will be conducted in order to determine the efficiency of the mechanical part of the pump. This is done such that an overall efficiency of the entire pump can be presented.

The investigation of the mechanical system includes examining the friction and bearings between the piston and the eccentric shaft, and the friction between the piston and cylinder along with an analysis of the effect of the piston ring.

When the issues determined in the problem analysis are considered, the problem specification can be specified as:

Analyse and determine the efficiency of the PMC Servi pump and suggest modifications for improvement.

This yields a series of subsidiary problems:

Produce a non-linear model of the PMC Servi pump and evaluate the efficiency

Decrease the pressure drop of the valves in order to improve the efficiency.

Consider further valve design, analyse it, and choose an appropriate design.

Expand the hydraulic model with leakage flows.

Analyse the mechanical parts of the pump, and implement frictions for the pump in the model.

Valve Design 3

To increase the accuracy of the predicted efficiency of a standard NG63 valve, it is decided to include a variable discharge coefficient, C_d . This is done by computation of C_d as a function of the inlet velocity and poppet position.

To find the discharge coefficient, a CFD analysis in a series of working points is performed for both a redesigned valve and for the standard NG63 valve. The CFD program computes a pressure loss at each given situation, and these are then used to calculate an appurtenant discharge coefficient.

The structure of this chapter consists of a brief summary of the method applied in the CFD analysis, a description of the valve design, and a CFD analysis of the chosen valve design compared with the NG63 valve. This is followed by implementation of the variable C_d in the non-linear model and an efficiency is computed. In the last section a series of parameters will be varied to improve the efficiency.

3.1 Computational Fluid Dynamics Analysis

The first thing to consider when modelling a valve in CFD is the Reynolds no. as it indicates whether the flow is turbulent or laminar. By extracting the Reynolds no. at the inlet of the valve it can be determined if the flow is laminar or turbulent. Figure 3.1.1 illustrates the Reynolds no. of the sharp-edged NG63 valve, which is calculated as given in Equation 3.1, for $\nu = \frac{\mu}{\rho}$.

$$\begin{aligned} Re &= \frac{Q_{VH} D_h}{\nu A_{in}} \\ &= \frac{Q_{VH} D_h \rho}{A_{in} \mu} \end{aligned} \quad (3.1)$$

where:	Re	Reynolds no.
	D_h	Hydraulic diameter/length
	A_{in}	Inlet area of the valve
	ρ	Density
	μ	Dynamic viscosity
	ν	Kinematic viscosity

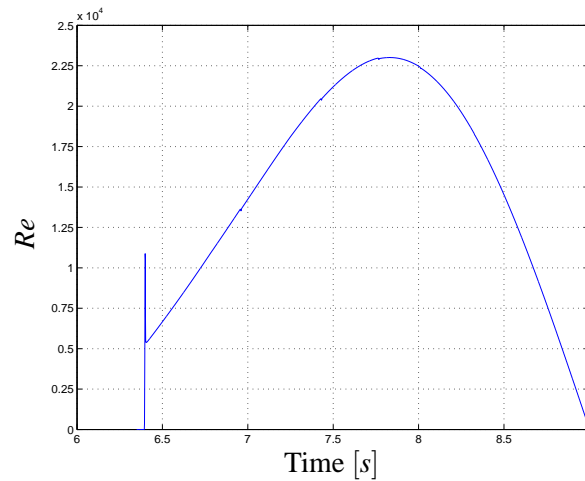


Figure 3.1.1: Reynolds no. at valve inlet for a NG63 valve mounted as outlet valve of the cylinder.

The Figure states that a turbulent flow is expected, due to the fact that the flow in a seat valve is typically considered turbulent when the Reynolds no. is above 900 and here the Reynolds no. is primarily above 1000 [Sørensen, 1999]. From this it is concluded that a turbulent solver for the CFD analysis is necessary.

To perform the CFD-analysis ANSYS Fluent is used and the CAD of the fluid is computed in SolidWorks. The method applied along with some of the results is described in appendix B.

The structure of appendix B is as follows:

- A brief introduction to the Navier-Stokes equations and fluid dynamics is described in section B.1.
- To approximate these equations the $k - \epsilon/RNG$ turbulence model is used, and is explained briefly in section B.1.1.
- To discretise and calculate the turbulence the SIMPLE algorithm is used, which is explained in section B.1.2, and the convergence of this solver is described in section B.1.3.
- The mesh of both the NG63 valve and the deflector valve is explained in appendix B.3
- The results of the CFD analysis is illustrated in section 3.3 and explained further in appendix B.4

Before making any conclusions from a CFD simulation, it is important to understand the application of the results. In this project the results are used to examine relative improvements of the valve design compared with the standard NG63 valve. If the results of a CFD analysis were to give a realistic picture of the flow through the valve, the settings of the mesh, solver etc. were to be adjusted to fit measured experimental test results of the situation. This would be a massive iterative process and is deemed not to be necessary when the application of the results are considered.

However before this analysis can be fulfilled the deflector valve designed, will be explained and an opening area function will be derived.

3.2 Deflector Design

This section describes the valve design with emphasis on the outlet valve of the cylinders. It is a result of iterated simulations, and is based on some of the main conclusions of a Ph.d. project which describes the fluid-mechanic design of a seat valve [Sørensen, 1999]. A specific deflector design is designed and measured in a large amount of steady-state situations. These results will be evaluated to formulate a discharge coefficient depending on the given operating point.

A deflector deflects the flow such that the total pressure increases locally and thus forces the poppet upwards hence opening the valve. By doing so, the deflector will compensate for some of the closing flow force caused by the increasing momentum of the fluid. The local increment in pressure is illustrated later on the pressure plot on Figure 3.3.3.

According to Sørensen a series of ratios between the dimensions of the deflector must be fulfilled [Sørensen, 1999]. Figure 3.2.1 illustrates the lengths and notations of the valve, and the according values are given in Table 3.2.1. The ratios from the work of Sørensen are all fulfilled in the design, and are given in Table 3.2.2. If the valve design was to be fitted closer to the ratios suggested by [Sørensen, 1999], an iterative design process is necessary. However, the purpose of the design is not to prove that the suggestions are accurate, only that the flow force compensation method stated by Sørensen is applicable and can improve the efficiency in the designated application.

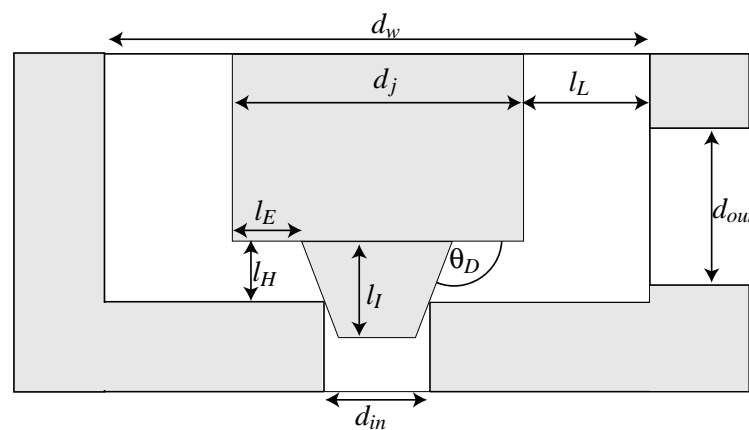


Figure 3.2.1: Lengths and names of the deflector.

Parameter	l_H	l_E	$d_{in} = d_{out}$	d_w	d_j	l_I	l_L	θ_D
Values	12.75[mm]	30[mm]	63[mm]	220[mm]	132[mm]	20[mm]	43.86[mm]	110°

Table 3.2.1: Lengths of the designed deflector.

3. Valve Design

Ratios	l_H/d_{in}	l_E/d_{in}	d_w/d_j	l_L/d_{in}	d_w/d_{in}
Suggested	max 0.45	min 0.25	min 1.5	min 0.35	min 2.0
Designed	0.202	0.476	1.66	0.69	3.5

Table 3.2.2: Geometrical relations of the deflector. The suggested ratios are taken from the PHD. project by Sørensen [Sørensen, 1999].

The parameters for the designed deflector valve is given in Table 3.2.3. At this point the spring constant and the distortion is a set of initial guesses, but these are later varied in order to improve of the efficiency, cf. section 3.5. The mass is calculated by drawing the poppet in SolidWorks and setting the material. In this case the choice is aluminium.

Symbol	Description	Value	Unit
M_{pop}	Mass of poppet	3.6	$[kg]$
k_{spr}	Spring constant	1000	$[\frac{N}{m}]$
x_{pop*}	Distortion	50	$[mm]$
A_A	Pressure area in port A	3117	$[mm^2]$
A_B	Pressure area of port B	10625	$[mm^2]$
A_X	Pressure area in port X ($A_A + A_X$)	13742	$[mm^2]$

Table 3.2.3: Specifications of the deflector.

From these specifications the opening area of the poppet can be calculated, and is explained in the following section.

3.2.1 Opening Area of Deflector Valve

The opening area of the deflector valve differs significantly from that of the standard sharp-edged NG63 valve. The opening area is divided into two stages: Stage 1, where the lowest edge of the poppet is still suspended into the inlet opening. Stage 2, where the lowest edge of the poppet is above the top edge of the seat, and hereby massively increases the inlet area compared to stage 1. The two stages are described in detail including a mathematical expression in in appendix C.

Figure 3.2.2 illustrates the opening of the valve. The blue line is the area function as a discontinuous function, meaning that the transitional region between the two stages is not modelled. If a more accurate function was needed, this area would have to be modelled more precisely as well. Instead a rate-limiter function is inserted to prevent any discontinuity. The rate limiter, limits the first derivative of the opening area to a certain value, illustrated with the red line on Figure 3.2.2.

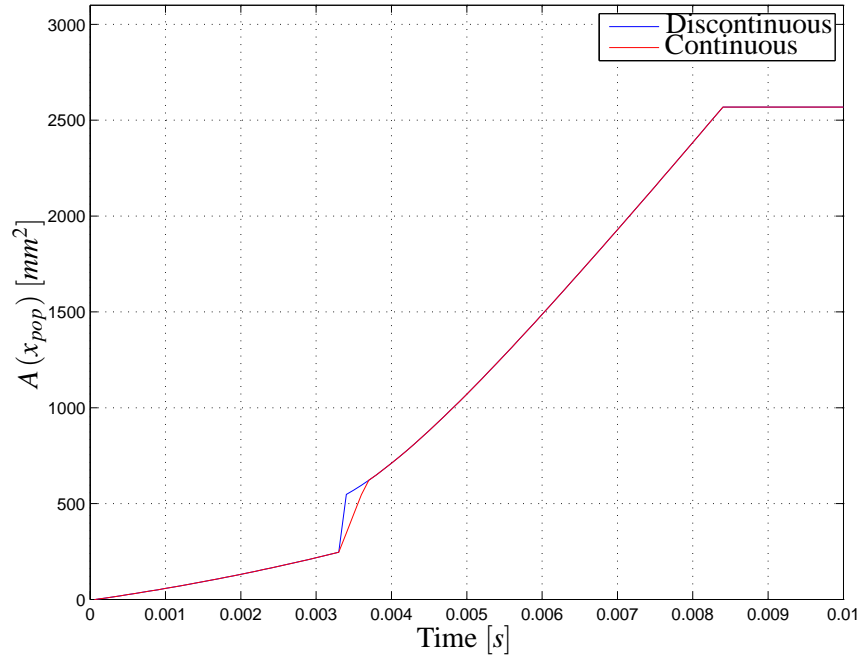


Figure 3.2.2: Opening area function.

3.2.2 Dimensional Analysis

The flow required to test a single valve is up to approximately $0.05[m^3/s]$. This flow is not available in the laboratory, thus it is necessary to determine if the system is scalable; this involves a dimensional analysis of the valve and to determine the relation between the small scale model and the prototype.

If the Reynolds no. of a model and a prototype are equal, they are dynamically similar, assuming that the tolerances and surface roughnesses can be produced at downsized level [Szirtes, 2006]. By equating the Reynolds no. at the inlet of the downsized model and the prototype, a relation can be derived:

$$\begin{aligned}
 Re_m &= Re_p \\
 \frac{Q_{in_m} D_{h_m}}{v A_{in_m}} &= \frac{Q_{in_p} D_{h_p}}{v A_{in_p}} \\
 \frac{Q_{in_m} D_{h_m}}{A_{in_m}} &= \frac{Q_{in_p} D_{h_p}}{A_{in_p}}
 \end{aligned} \tag{3.2}$$

where: $D_{h_{m/p}}$ Hydraulic diameter of model/prototype

By inserting the inlet area $A_{in} = D_h^2 \pi / 4$, the hydraulic inlet diameter of the model can be isolated.

3. Valve Design

Note that the hydraulic diameter of a circular tube is equal to the tube diameter.

$$\begin{aligned}\frac{Q_{in_m} D_{h_m}}{D_{h_m}^2 \frac{\pi}{4}} &= \frac{Q_{in_p} D_{h_p}}{D_{h_p}^2 \frac{\pi}{4}} \\ \frac{Q_{in_m}}{D_{h_m}} &= \frac{Q_{in_p}}{D_{h_p}} \\ D_{h_m} &= \frac{Q_{in_m} D_{h_p}}{Q_{in_p}}\end{aligned}\tag{3.3}$$

The maximum flow through the prototype valve is $0.05 \text{ [m}^3/\text{s}]$, and the diameter of the prototype inlet area is 63 [mm] . E.g. if the laboratory has a maximum flow of $0.005 \text{ [m}^3/\text{s}]$, this will result in an inlet diameter of 6.3 [mm] . When producing a downsized model with this ratio, another problem will arise governing the production of downsized fillet radius and surface roughness. E.g. the prototype has a fillet radius of 1 [mm] , which sets the fillet radius of the model to 0.1 [mm] . This cannot be produced in the associated workshop. Hence the CFD analysis will not be verified with experimental results.

3.2.3 Discharge Coefficient

To derive a discharge coefficient, C_d , from the computed pressure losses, the orifice equation is applied. By substituting $Q_{in} = A_{in} u_{in}$ and isolating C_d , the discharge coefficient is found:

$$Q_{in} = C_d A(x_{pop}) \sqrt{\frac{2}{\rho} \Delta P}\tag{3.4}$$

$$C_d = \sqrt{\frac{\rho}{2 \Delta P}} \frac{A_{in} u_{in}}{A(x_{pop})}\tag{3.5}$$

where: A_{in} Inlet area of the valve
 u_{in} Average velocity at valve inlet
 ΔP Pressure across the valve
 $A(x_{pop})$ Valve opening area

3.3 CFD Results

This section describes the CFD results of the NG63 valve and the deflector valve. First a series of Figures illustrates how the fluid flows through the NG63 valve and the deflector valve, secondly the calculated pressure losses of the two valves are compared. The two discharge coefficients are then implemented in the non-linear model to calculate the complete efficiency. Notice that all CFD

simulations are done under the assumption of steady state conditions.

3.3.1 Standard NG63 Valve

The streamlines in Figure 3.3.1 and 3.3.2 illustrates the flow through the NG63 valve at 10 and 25[mm] opening respectively. The black lines indicates the general wireframe of the valve, cf. Figure B.3.2 with the illustrated mesh. The two Figures have equal colormapping, meaning that the colors indicating the magnitude of the velocity of the particles are the same on both Figures.

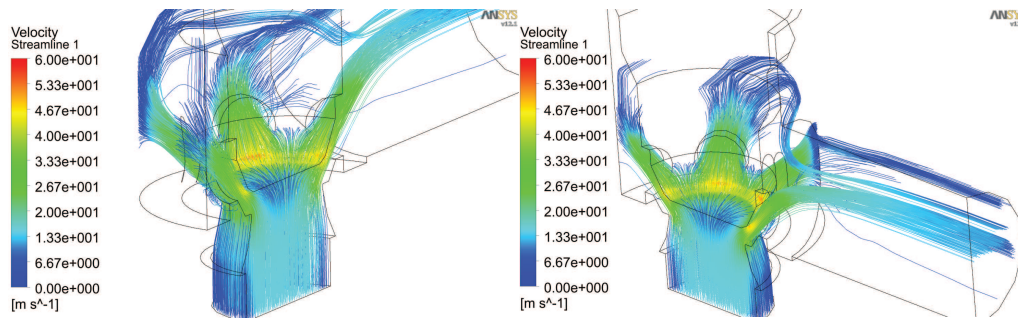


Figure 3.3.1: Streamline for a 10[mm] opened NG63 valve at inlet velocity of 15[m/s].

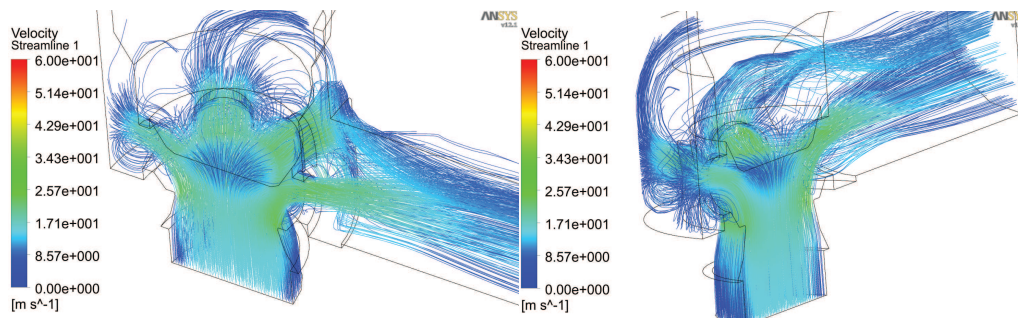


Figure 3.3.2: Streamline for a 25[mm] opened NG63 valve at inlet velocity of 15[m/s].

From these Figures it is clear that by increasing the opening, the velocity of the fluid in the opening decreases along with the pressure drop across the valve.

The velocity and the pressures at the symmetry plane is illustrated in Figure 3.3.3 for a 10[mm] opened valve at $u_{in} = 4.5 \left[\frac{m}{s} \right]$ and $u_{in} = 15 \left[\frac{m}{s} \right]$. And Figure 3.3.4 illustrates the same two velocity situations for a 25[mm] opened valve. The colormapping of the Figures follows the inlet velocity, meaning that the colors of the topmost contours of Figure 3.3.3 and 3.3.4 are identical, and likewise for the bottom contours.

3. Valve Design

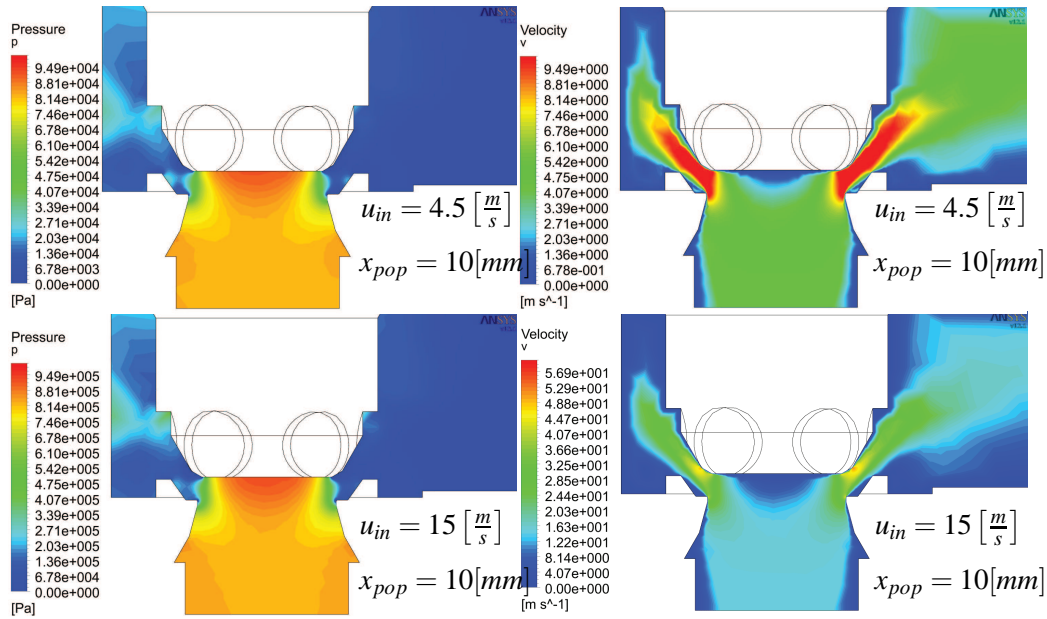


Figure 3.3.3: Velocity and pressure contours for a 10[mm] opened NG63 valve at inlet velocity of 4.5[m/s] (upper contours) and 15[m/s] (lower contours). Pressures in the left-hand side and velocity at the right-hand side. Notice the different colormapping when fluid inlet velocity is altered. The colormapping on the upper contours on this Figure and the upper contours of Figure 3.3.4 have equal pressure and velocity intervals: [0; 1][bar] and velocity [0; 10] [$\frac{m}{s}$]. Likewise for the lower contours: [0; 10][bar] and [0; 60] [$\frac{m}{s}$]

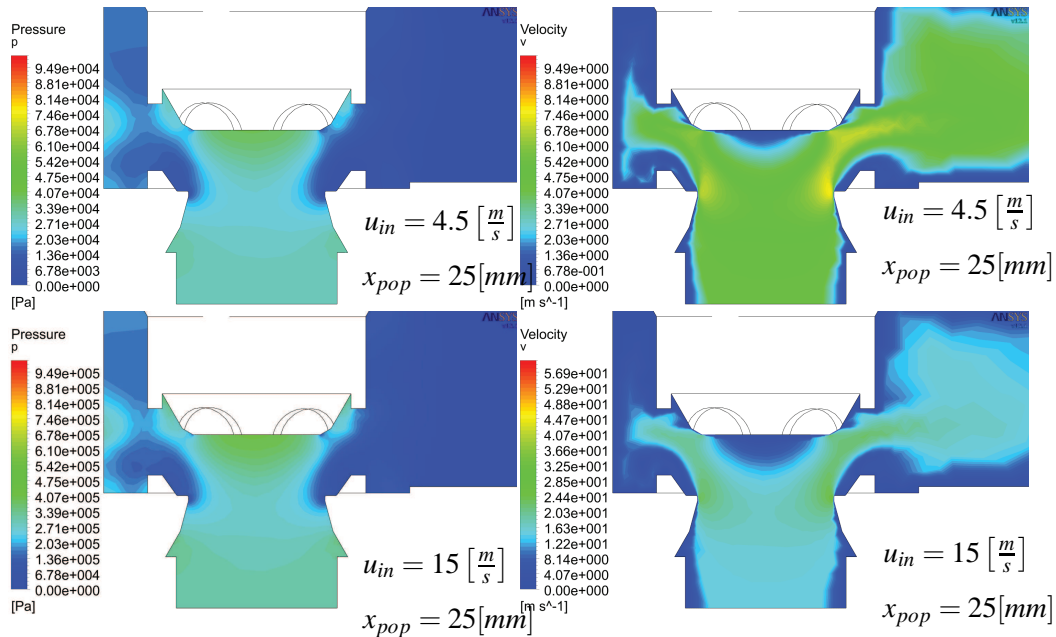


Figure 3.3.4: Velocity and pressure contours for a 25[mm] opened NG63 valve at inlet velocity of 4.5[m/s] and 15[m/s]. Notice the different colour mapping when fluid inlet velocity is altered.

When the pressures of the four cases are compared it is clear that the pressure is almost identical

in distribution but not in magnitude, when increasing the velocity. This means that design features implemented and examined at a given velocity will have a similar effect when the velocity is increased.

The pressure differences from the inlet to the outlet are calculated at a series of inlet velocities and poppet positions, given in Table 3.3.1. The pressure differences are then utilised to compute the discharge coefficient. However, to do this the opening area of the valve is required.

$u_{in} [m/s]$ \ $x_{pop} [m]$	0.005	0.01	0.015	0.025	0.030
4.5	2.65	0.83	0.44	0.33	0.30
9	9.75	3.10	1.67	1.28	1.15
12.5	18.33	5.83	3.16	2.43	2.20
15	26.14	8.30	4.51	3.47	3.13

Table 3.3.1: Pressure drop across the NG63 standard valve in $[bar]$.

3.3.2 Opening Area of NG63 Valve

In the previous analysis of the non-linear model, the opening area of the standard NG63 valve was implemented as a sharp-edged valve. This is now altered to a more accurate version by measuring the opening area of the valve as a function of the poppet position in SolidWorks. The opening area is measured between the edge of the poppet and the seat. However, it should be noted that when the valve is in its maximum position the restriction between seat and poppet is bigger than the restriction created by holes on the sleeve. This opening area in the sleeve is slightly smaller than the sharp-edged opening area applied so far. This is illustrated in a section view of the NG63 valve on Figure 3.3.5, where $s_{A(x_{pop})}$ is the distance used to calculate the current opening area, and d_{hole} is the diameter of the holes. The sleeves has five holes with a diameter of each $26[mm]$ creating a complete opening area of $2645.7[mm^2]$, which is less than the opening area of the valve when $x_{pop} > 18[mm]$. This means that the holes are the smallest restriction in a large amount of the cycle. However modulation of these restrictions can be complicated and is not included in this project. The former version of the opening area of the sharp-edged valve and the corrected version using a lookup table are both illustrated in Figure 3.3.6.

Another complication when calculating the opening area is that the distance marked with $s_{A(x_{pop})}$, in Figure 3.3.5, is not the shortest distance throughout the movement of the poppet. The distance s_C is actually the shortest distance between the poppet and the sleeve in the illustrated position, $x_{pop} = 25[mm]$. Likewise the holes are not applied when the opening area of the valve is calculated, due to the complexity of the function. If further accuracy of the opening was needed, a different opening area function could be calculated from the mentioned relations.

The lack of accuracy by using $s_{A(x_{pop})}$ instead of the smallest gab at s_C means that the opening area is an optimistic estimate in regards to efficiency. This calculates a higher efficiency than what is

3. Valve Design

actually the case, since a larger opening area means lower pressure drop, cf. Table 3.3.1.

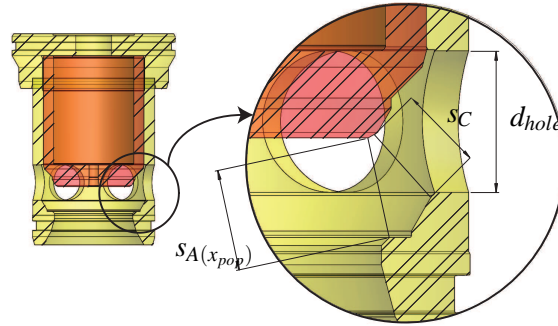


Figure 3.3.5: Sleeve and poppet of the NG63 valve opened 25[mm]. The sleeve is marked with yellow and the poppet is marked with red.

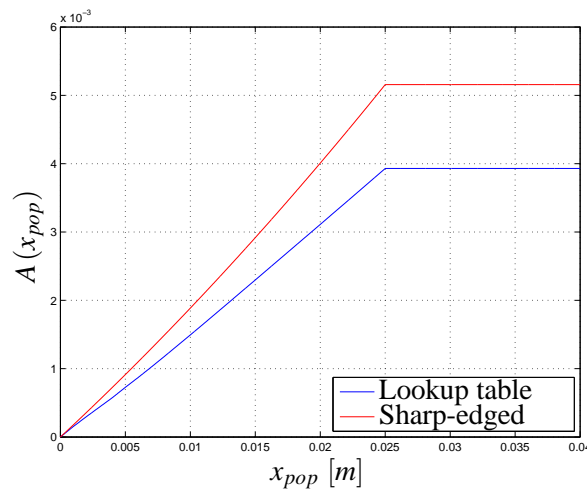


Figure 3.3.6: Opening area of a standard NG63 valve.

The opening area is applied along with Equation 3.5 to form the C_d given in Table 3.3.2 and is plotted as a function of the Reynolds no. in Figure 3.3.7. The C_d -value is significantly lower at maximum opening compared to the first assumption, $C_d \approx 0.8$. This indicates that a constant value of 0.8 can not be applied when the valve is analysed.

$x_{pop} [m] \rightarrow$		0.005000	0.01000	0.01500	0.02000	0.02500
$u_{in} [m/s]$	$A(x_{pop}) [m^2]$	0.0007270	0.001494	0.002298	0.003111	0.003930
		0.800	0.696	0.619	0.526	0.440
4.5		0.833	0.719	0.637	0.538	0.448
9		0.844	0.729	0.643	0.543	0.451
12.5		0.848	0.733	0.646	0.544	0.454
15						

Table 3.3.2: Discharge coefficient in an NG63 valve.

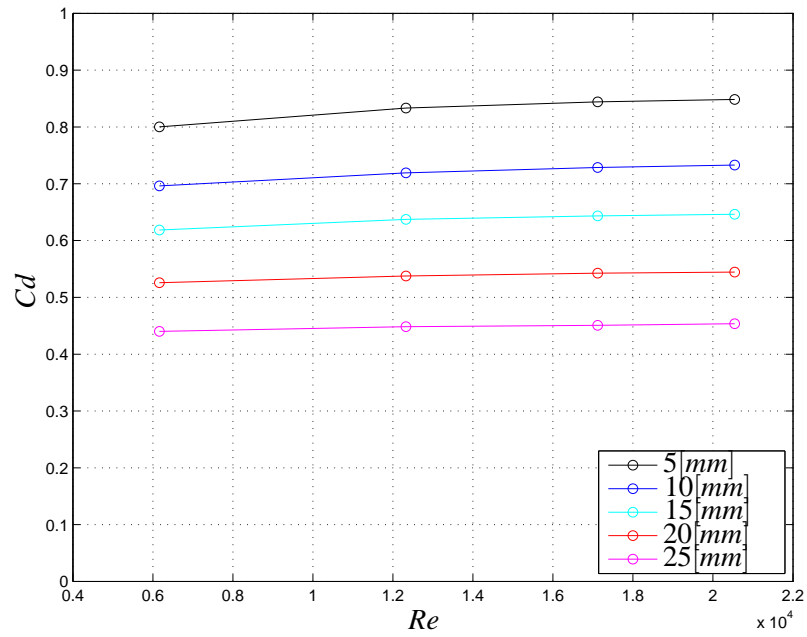


Figure 3.3.7: C_d of the NG63 valve as a function of the Reynolds no.

3.3.3 Deflector Valve

This section describes the CFD analysis of the deflector valve.

The streamlines of Figure 3.3.8 and 3.3.9 illustrates two situation of the deflector valve at $x_{pop} = 15[mm]$ and $x_{pop} = 30[mm]$ respectively at $u_{in} = 15 \left[\frac{m}{s} \right]$. Notice that the fluid is partially blocked by the deflector, and hereby increases the total pressure due to the increment in dynamic pressure.

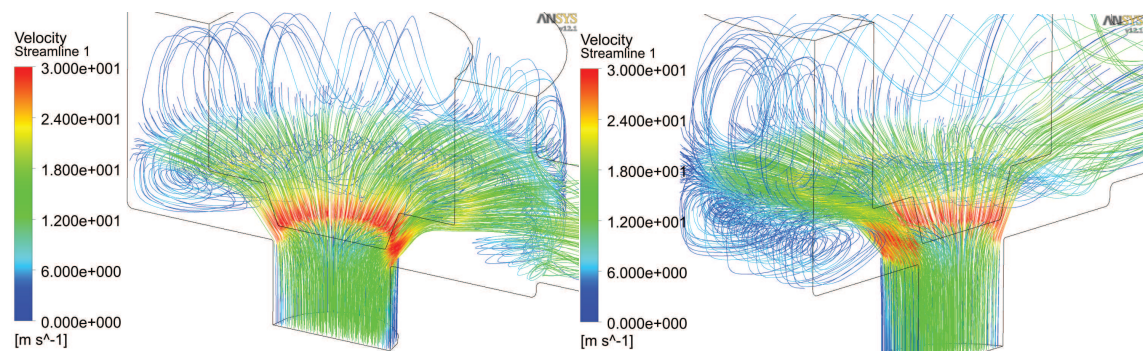


Figure 3.3.8: Streamline for a 15[mm] opened deflector valve at an inlet velocity of 15 $\left[\frac{m}{s} \right]$.

3. Valve Design

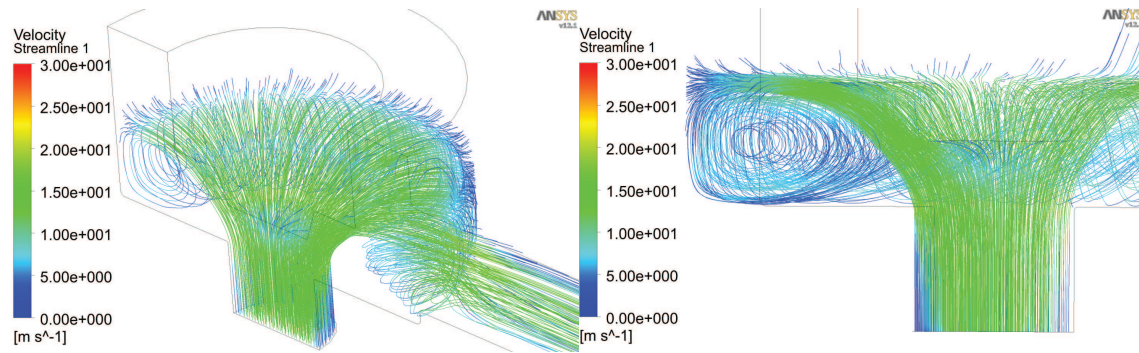


Figure 3.3.9: Streamline for a 30[mm] opened deflector valve at an inlet velocity of 15 $\left[\frac{m}{s}\right]$.

Figure 3.3.10 illustrates velocity and pressure contours of a 15[mm] opened deflector valve at $u_{in} = 4.5 \left[\frac{m}{s}\right]$ and $u_{in} = 15 \left[\frac{m}{s}\right]$. Notice that the pressure locally increases around the deflector at both velocities, this confirms the intention of the deflector.

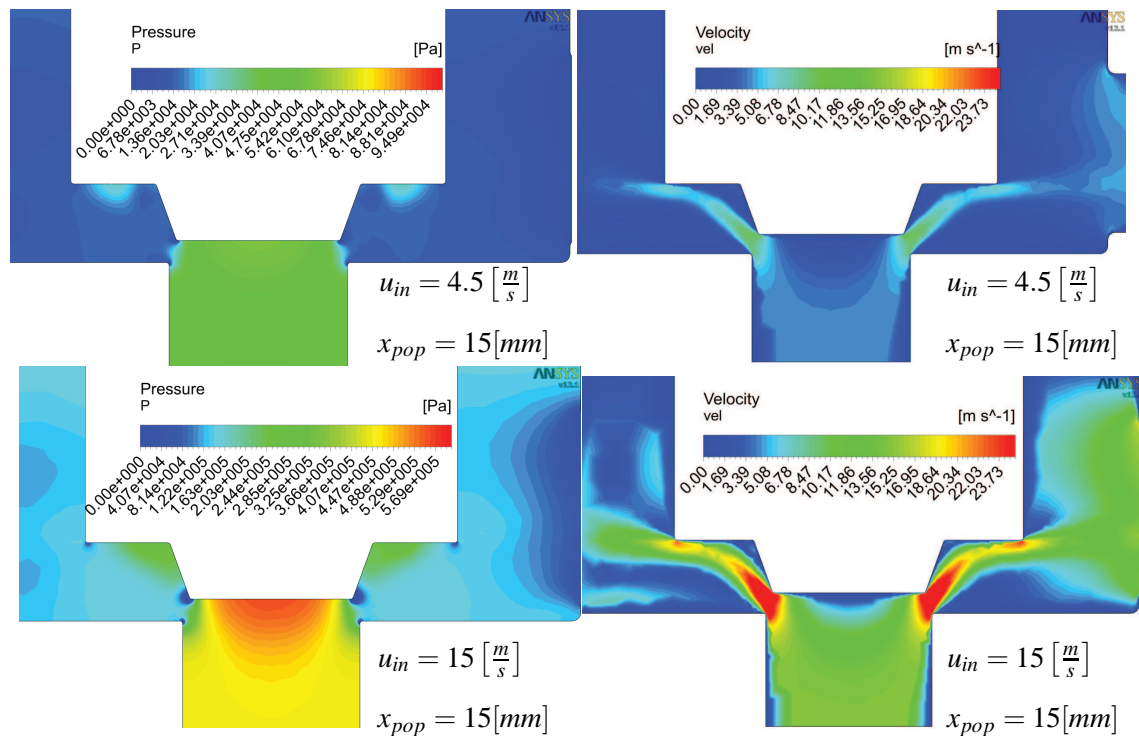


Figure 3.3.10: Velocity and pressure contours for a 15[mm] opened deflector valve at an inlet velocity of 4.5 $\left[\frac{m}{s}\right]$ and 15 $\left[\frac{m}{s}\right]$. Pressures in the left-hand side and velocity at the right-hand side. Notice the different colour mapping when the fluid inlet velocity is altered.

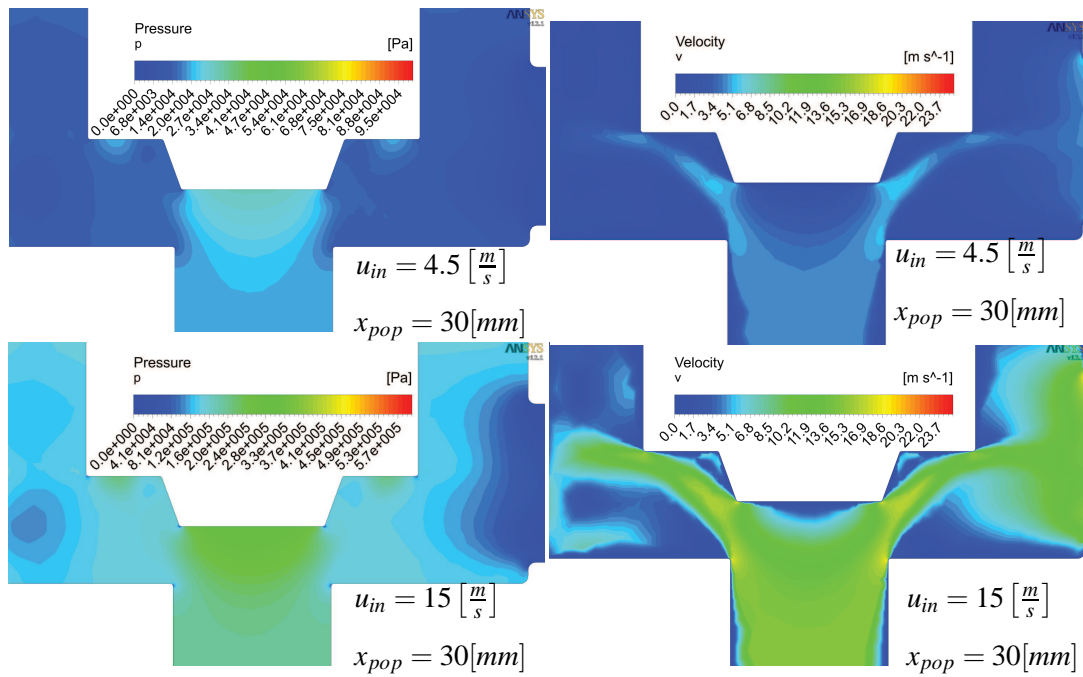


Figure 3.3.11: Velocity and pressure contours for a 30[mm] opened deflector valve at an inlet velocity of 4.5 [$\frac{m}{s}$] and 15 [$\frac{m}{s}$]. Pressures in the left-hand side and velocity at the right-hand side. Notice the different colormapping when the fluid inlet velocity is altered.

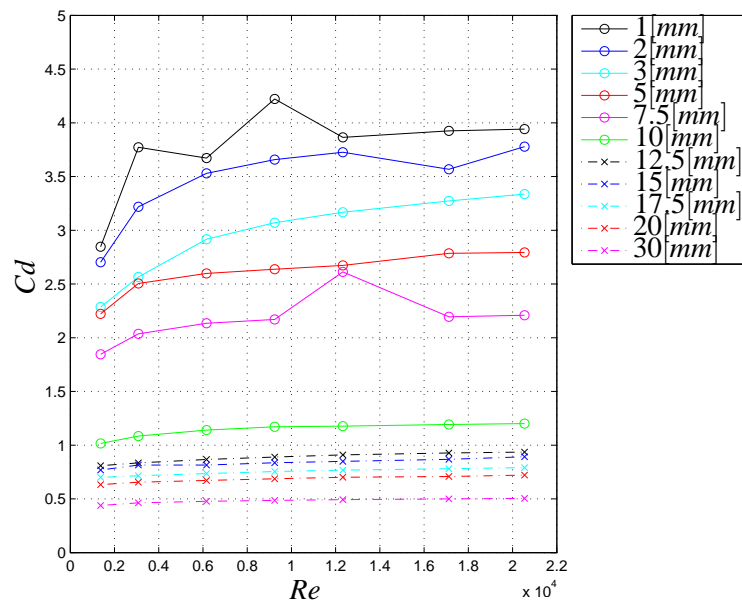


Figure 3.3.12: C_d of the deflector valve as a function of the Reynolds no. The different markers of the lines are used to illustrate the difference between the colours of the plot, since only six colours are utilised.

Like with the NG63 valve the discharge coefficient is calculated from the pressure drop at each situation. The pressure drop and the discharge coefficient are given in Table B.4.1 and B.4.2 re-

spectively in appendix B.4.

3.4 Variable C_d Implementation

A variable C_d as a function of the poppet position and the inlet velocity is now implemented in the non-linear model.

The variable C_d -coefficient is implemented as a lookup table, cf. Table 3.3.2 and B.4.2 in appendix for NG63 and deflector valve respectively. The pressure drops with the two valves mounted as high pressure valves in the non-linear model are illustrated in Figure 3.4.1.

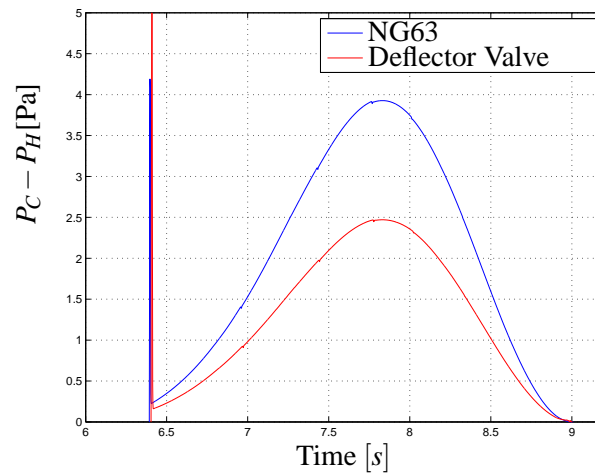


Figure 3.4.1: Pressure drop in the high pressure valve, for the NG63 and the deflector valve

The efficiency computed in the non-linear model with the NG63 and the deflector valve is given in Equation 3.6 and 3.7.

$$\eta_{NG63.Var.C_d} = 0.975862 \quad (3.6)$$

$$\eta_{Def.Valve.Var.C_d} = 0.983127 \quad (3.7)$$

By implementing variable C_d and a more accurate opening area, the efficiency of the NG63 valve has decreased by 1.3838 percentage points compared with constant C_d . This means that the first calculation of the efficiency for the pump with an NG63 valve applied with an opening area modelled as sharp-edged and constant C_d , was an optimistic calculation of the efficiency.

The deflector valve improves the efficiency by 0.7 percentage points compared with the NG63 valve. From this it can be concluded that the designs applied in the deflector valve improves the efficiency compared with a standard NG63 valve.

In this section, a valve was designed and compared with the standard NG63 valve. The spring tension and distortion will, in the following section, be altered to search for an optimum set of

variables. Likewise the mass will be varied, since this also can be altered within certain limits.

3.5 Parameter Variation

To determine the parameters of the valve which has not been found through the CFD analysis, a variation of parameters is conducted. Thus some specific parameters are chosen and implemented in the non-linear model with the deflector valve to evaluate the effect on the overall efficiency. Each parameter is varied in a chosen interval and the efficiency is calculated so that an optimum can be extracted. Each variation will be described in the following and a conclusion of the variation will be conducted at the end of the section. Only one parameter is varied at any given situation and when a new parameter is to be varied, all parameters are reset to the initial values.

3.5.1 Variation of Volume V_{p0}

A variation of the volume between the cylinder and the valve, V_{p0} , will be conducted.

First a variation of V_{p0} from $0.25 \cdot 10^{-3} [m^3]$ to $5.25 \cdot 10^{-3} [m^3]$ with steps of $1 \cdot 10^{-3} [m^3]$ was made and then a further variation from $15 \cdot 10^{-3} [m^3]$ to $90 \cdot 10^{-3} [m^3]$ with steps of $15 \cdot 10^{-3} [m^3]$ was conducted. The variation is illustrated in Figure 3.5.1.

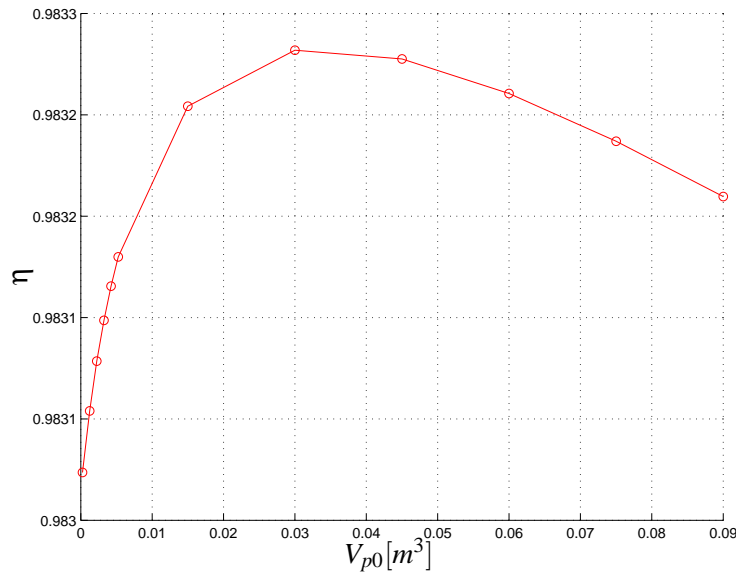


Figure 3.5.1: Efficiency plotted with respect to the volume V_{p0} .

From Figure 3.5.1 it is clear that an optimum volume in regard to efficiency is located around $30 \cdot 10^{-3} [m^3]$. A further analysis regarding the added weight by these volumes compared with the increment in efficiency, should be conducted. However since no specific requirement to weight is outlined in this project, $V_{p0} = 30 \cdot 10^{-3} [m^3]$ is still chosen as the optimum value for this parameter in the following analyses

3.5.2 Variation of the Mass of the Poppet M_{pop}

The mass of the poppet might affect the efficiency, as the equilibrium of forces of the poppet is dependent on the mass of the poppet. Therefore a variation of this parameter is conducted in the following.

A variation of M_{pop} was conducted as a series of simulations of the non-linear model and the efficiencies was computed for each run. The variations was done from 1[kg] to 18.5[kg] with steps of 0.5[kg] and the resulting efficiencies are presented in Figure 3.5.2.

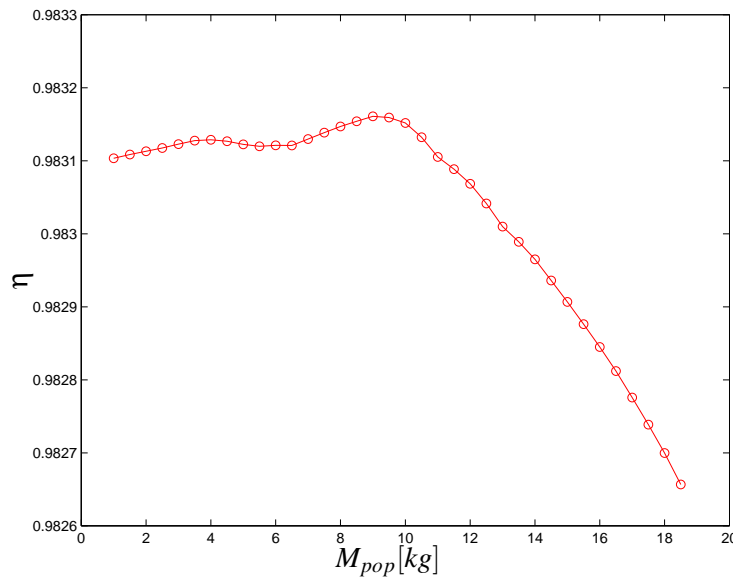


Figure 3.5.2: Efficiency with respect to the mass of the poppet M_{pop} .

From Figure 3.5.2 it is noticed that an optimum can be achieved at a mass of the poppet of $M_{pop} = 9$ [kg], however, it is also noticed that a local optimum is present at $M_{pop} = 4$ [kg]. The lower efficiency at low mass, can be explained by the dynamics of the pump: a low mass of the poppet or a low V_{p0} will enable the valve to react on high frequency influences from the pressure in the cylinders. A M_{pop} of 18[kg] is not desired since this will make the valve too slow.

Since the optimal efficiency is at a mass of $M_{pop} = 9$ [kg], this mass has to be considered. The current design yields a mass of the poppet of $M_{pop} = 5.5$ [kg] if produced in steel and $M_{pop} = 3.6$ [kg] if produced in aluminium, both estimated from SolidWorks. By comparing the efficiencies of the local minimum at $M_{pop} = 4$ [kg] and the global minimum at $M_{pop} = 9$ [kg] the difference is:

$$\eta_{9[kg]} - \eta_{4[kg]} = 0.0032 \quad \text{percentage points} \quad (3.8)$$

Should the poppet be produced in steel at a mass of $M_{pop} = 9$ [kg], placement of the spring would be a problem due to lack of space above the poppet. Considering the rather small difference in efficiency between $M_{pop} = 9$ [kg] and $M_{pop} = 4$ [kg], and the fact that the mass of the poppet in aluminium is easier altered to meet the local optimum of 4[kg]; the poppet with the lowest mass is

chosen.

3.5.3 Variation of Spring Constant k_{spH} and distortion x_*

The spring force can be affected by changing the spring constant which in turn affects the opening profile of the poppet. Since the spring force acts against the poppet opening, it is highly likely that altering this could improve the overall efficiency. However, the distortion must be taken into account as well.

The spring constant is varied from $100[N/m]$ to $10100[N/m]$ and the distortion is varied from $x_* = 0[m]$ to $x_* = 405 \cdot 10^{-3}[m]$ which yields the plot presented in Figure 3.5.3

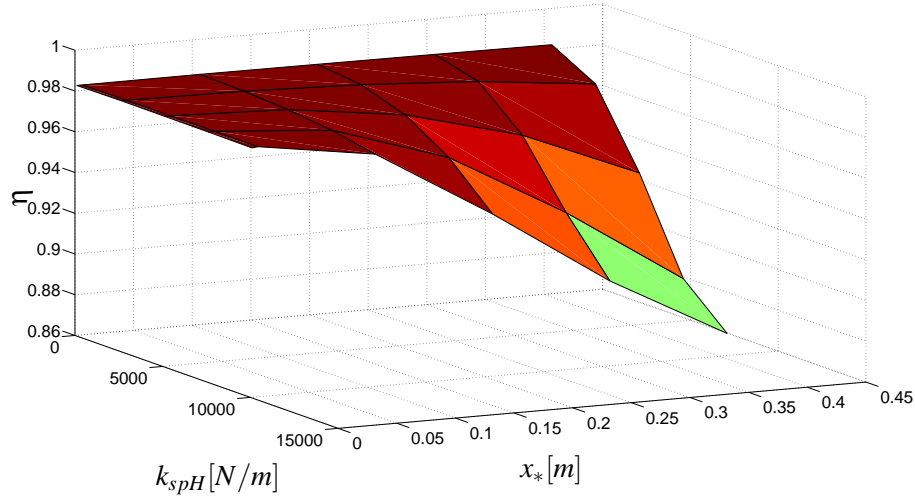


Figure 3.5.3: Efficiency with respect to the spring constant, k_{spH} , and the distortion, x_* .

From Figure 3.5.3 the maximum efficiency is:

$$\eta_{max} = 0.98325$$

for a spring constant of $k_{spH} = 2600[N/m]$ and a distortion of $x_* = 0[m]$. To implement a spring with zero distortion is difficult, since the spring will likely either be compressed by an unknown distance or not be compressed at all, introducing a clearance. Neither of the two situations are desirable, thus a spring with a distortion of $x_* = 1 \cdot 10^{-3}[m]$ is chosen to avoid movement of the poppet independently of the spring. The spring constant is set to the mentioned optimum value of $k_{spH} = 2600[N/m]$.

3.5.4 Final Parameters

From the preceding sections it has been determined that the values given in Table 3.5.1 will be applied as the final parameters for the deflector valve. These values might not be the actual optimum

3. Valve Design

though. In order to find this, an examination of the correlation between the varied parameters will have to be conducted. This will not be fulfilled in this project, since the goal of this analysis is merely to give an understanding of which parameters significantly affects the efficiency of the pump. The chosen values should however yield a better efficiency than the initial set of parameters.

Parameter	V_{p0}	M_{pop}	k_{spH}	x_*
Value	$30 \cdot 10^{-3} [m^3]$	$4 [kg]$	$2600 [N/m]$	$1 \cdot 10^{-3} [m]$

Table 3.5.1: The final values chosen for the analysed parameters of the deflector valve.

When a simulation in the non-linear model is conducted with the parameters presented in Table 3.5.1 the efficiency for the deflector valve is compared with that of the NG63 valve from Parker.

$$\begin{aligned}
 \eta_{NG63} &= 0.975862 \\
 \eta_{Deflector} &= 0.983288 \\
 \eta_{Deflector} - \eta_{NG63} &= 0.007425
 \end{aligned} \tag{3.9}$$

From this it is noticed that a total improvement of 0.7425 percentage points is achieved through the new design, including a deflector to shape the flow force and a parameter variation. As stated earlier this can possibly be improved even more if an optimisation analysis is conducted. The set of parameters given in Table 3.5.1, with the mass altered to $M_{pop} = 9 [kg]$, was also implemented in the non-linear model to examine if the efficiency was actually higher. This simulation yielded an efficiency of $\eta = 0.983233$ which is smaller than the efficiency of the chosen parameters with $M_{pop} = 4 [kg]$. This underlines the fact that the optimal value of each parameter is not necessarily the optimal value of the system.

3.5.5 Examination of the effect of the viscous friction κ

The effect of the viscous friction on the efficiency has yet to be determined. This is not a parameter which can be altered as easily as the spring stiffness, however it may give an idea of which effect the viscous friction has on the efficiency. This makes it possible to strive for a particular viscous friction, e.g. by designing the surface roughness. This is done by changing the viscous friction κ from $\kappa = 0 [Ns/m]$ to $\kappa = 2000 [Ns/m]$ with steps of $100 [Ns/m]$. The efficiency is presented in Figure 3.5.4.

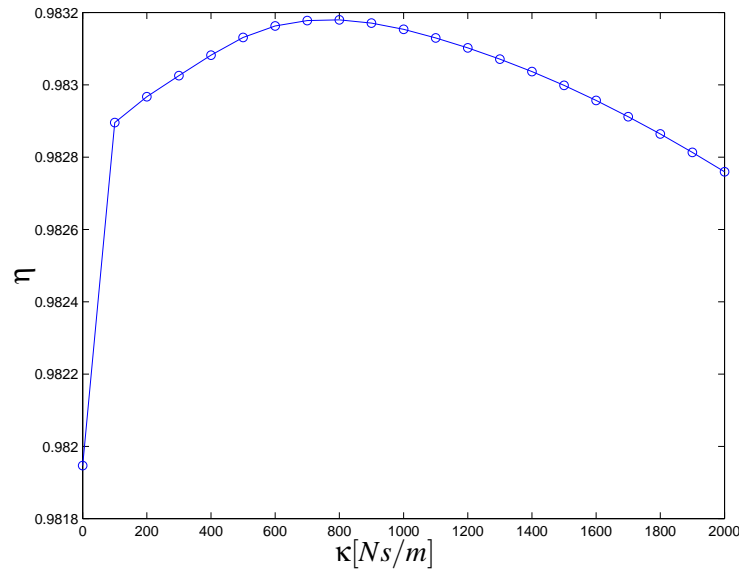


Figure 3.5.4: Efficiency plotted with respect to the viscous friction, κ .

The maximum efficiency is at a viscous friction of $\kappa = 800 [Ns/m]$. This is not necessarily easily obtained but it gives an indication of which viscous friction is the optimum value. The viscous friction is a function of the viscosity, surface roughness and clearances between poppet and valve. More research has to be conducted in order to determine the method to shape the viscous friction κ .

3.5.6 Examination of the effect of the Flow Force F_{fl}

The effect of the flow force on the overall efficiency is explored in the following to determine how the flow force could be shaped in order to optimise the efficiency. This is done by varying the flow force by multiplying the flow force with a factor between 0 and 1 in steps of 0.05. The result is presented in Figure 3.5.5

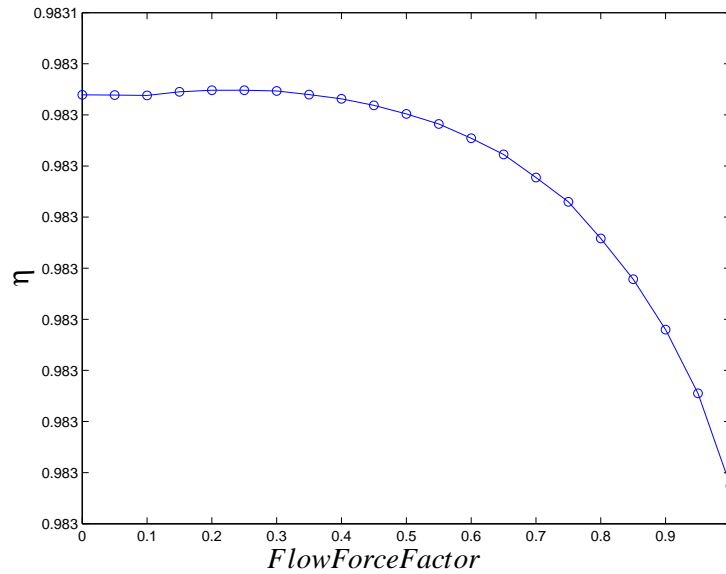


Figure 3.5.5: Efficiency plotted with respect to the flow force factor.

The maximum efficiency is at a flow force of 20% of the original flow force. As with the viscous friction, this flow force is not necessarily as easily obtained as e.g. choosing a specific spring constant. Several methods for flow force compensation exists, and one of these has been explained earlier in this chapter. The applied method did not reach the exact optimum. To reach this, several deflector designs are to be designed such that the compensation can reach this optimum. However, the results from this variation still complies with the result of inserting a flow force compensated valve. This means that flow force compensation improves the efficiency.

3.5.7 Examination of the Effect of Implementing Several Valves

The effect of implementing several identical valves at both the in- and outlet for each cylinder is here examined. This is believed to improve the efficiency, as the opening area is larger for the same flow. Thus a pump with two NG63 valves implemented as both out- and inlet valves are examined, and next the two deflector valves are implemented at both out- and inlet. After this the effect of further increasing the number of valves is investigated as up to four deflector valves are implemented as both in- and outlet valves. The valves are implemented in the model with a parallel coupling.

When this is implemented on an actual pump, a manifold would have to distribute the flow between the valves and a minor loss should be expected in this manifold. Thus the efficiency calculated is expected to be higher than the actual efficiency. All simulations are run with the optimal parameters for the deflector valve given in Table 3.5.1.

3.5.7.1 Comparison Between One and Two Valves Implemented

The difference in the efficiency of the pump after implementation of two NG63 and two deflector valves is presented here:

$$\begin{aligned}\eta_{2NG63} &= 0.990290 \\ \eta_{2Deflector} &= 0.992038 \\ \eta_{2Deflector} - \eta_{2NG63} &= 0.001748\end{aligned}\quad (3.10)$$

The difference in efficiency between the two types of valves is 0.1748 percentage points. This is a smaller difference between the NG63 and deflector valve compared with the single valve installation. A significant increase in absolute efficiency is noticed. For the deflector valve a total increase of 0.8750 percentage points is noted and for the NG63 valve the increase is 1.44280 percentage points compared with the single valve installation.

3.5.7.2 Further Increment of Valves

Given the results from section 3.5.7.1, the effect of further increasing the number of valves in both the in- and outlet of the cylinder is investigated. As the deflector valve yielded the highest efficiency with two valves, this is the foundation of the investigation. In Figure 3.5.6 three and four valves has been tested as well, and the efficiencies are presented.

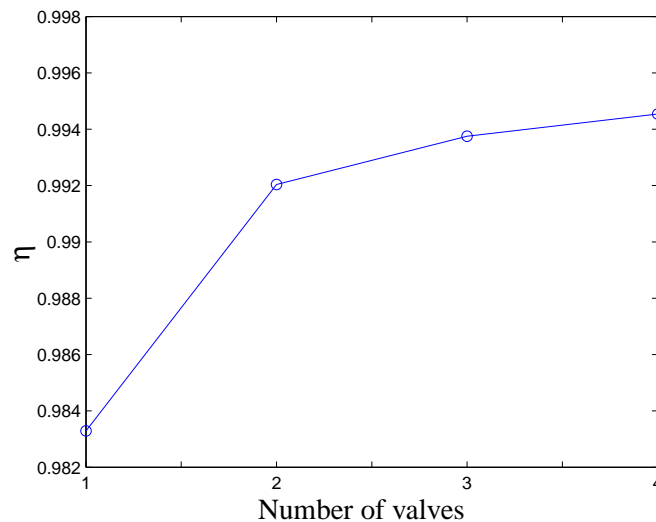


Figure 3.5.6: Efficiency plotted with respect to the number of valves.

In Figure 3.5.6 it is clear that an increase in the number of valves applied also increases the efficiency of the pump. It is also noticed that the increase in efficiency from two to three valves is less than from one to two valves, and the increase from three to four is less than from two to

three valves. Thus another parameter has to be taken into account in order to decide the number of valves. Two valves are chosen for the subsequent simulations in this project.

3.6 Summary

The valve design analysis showed several significant factors to be considered when designing a valve for the non-linear pump.

- Larger valve opening means lower pressure drop. This means that in a second iterative design procedure more focus should be on the maximum displacement of the poppet.
- Altering the mass of the poppet does not improve the efficiency significantly. As long as the mass of the poppet is between $[4;9]$ [kg] the efficiency is not changed substantially. From this it is concluded that low focus should be on lowering the mass of the poppet.
- Sharp-edges near high fluid velocities can create cavitation in the fluid. This should be examined by experiments, since cavitation in the fluid can cause system failure. A single simulation of the deflector valve in $x_{pop} = 30[mm]$, $u_{in} = 15[\frac{m}{s}]$ was done with increment of the fillet radius from $1[mm]$ to $3[mm]$ and the total pressure drop across the valve was lowered by 23.5%, from $2.02[bar]$ to $1.55[bar]$. However the force on the poppet was also lowered by 10.6%, from $1278[N]$ to $1143[N]$. This means that focus should be on finding the correct optimum between flow force compensation and pressure drop, by altering the fillet radius.
- Flow force compensation - The deflector works as expected and increases the local pressure on the poppet, hereby forcing the poppet to open. To evaluate if the flow force compensation has the correct value, e.g. examine if it overcompensates, a more undergoing analysis with different poppet sizes is needed. In this way the optimum between compensation and pressure drop due to the design can be found. However it can still be concluded that flow force compensation will increase the efficiency. In the analysis of the magnitude of the flow force it was established that a reduction to 20% of the original flow force obtained with the deflector valve is optimal. This indicates that a better efficiency can be obtained with further research into the flow force compensation.
- A valve with a high bandwidth will magnify the higher frequencies of the oscillations of the system. This will decrease the overall efficiency, as the dependency between the efficiency and M_{pop} and V_{p0} showed. Thus focus should be on keeping the bandwidth at an appropriate level. This is further emphasised by the analysis of the viscous friction κ which showed that an increase to $\kappa = 800[Ns/m]$ also yielded the best efficiency.
- The number of valves applied in the pump has to be closer examined with regard to the cost and the weight. It has been shown that an increase in the number of valves for both in- and

outlet of the cylinder increases the efficiency. This can be applied to gain a higher efficiency for the hydraulic part of the pump, however the increased number of valves also raises the cost which has to be compared to the profit from the gained energy due to increased efficiency.

This completes the analysis of the valves of the hydraulic part of the PMC Servi pump concept. The statements given above can be used as a guideline when performing the next design procedure in the future. It is desired to more accurately find the efficiency of the pump and thus in the next chapter the frictions and leakages of the pump are analysed.

3. Valve Design

Friction and Leakage Analysis⁴

As mentioned in the problem specification it is desired to further develop the non-linear model such that a more accurate efficiency can be calculated. This chapter consists of an analysis of the friction in the pump; more specifically the bearing between the piston rod and the eccentric shaft, and the friction and leakage between the piston and the cylinder.

4.1 System Description

This section briefly describes the frictions and leakages for implementation in the non-linear model.

The bearing between the rotating shaft and the piston-rod can be fulfilled in a number of ways, e.g. with hydrostatic lubrication in a slipper pad, marked with green on Figure 4.1.1. The principal is to decrease the friction by creating a thin oil film between the two surfaces. The friction in this slipper pad is described in section 4.3.

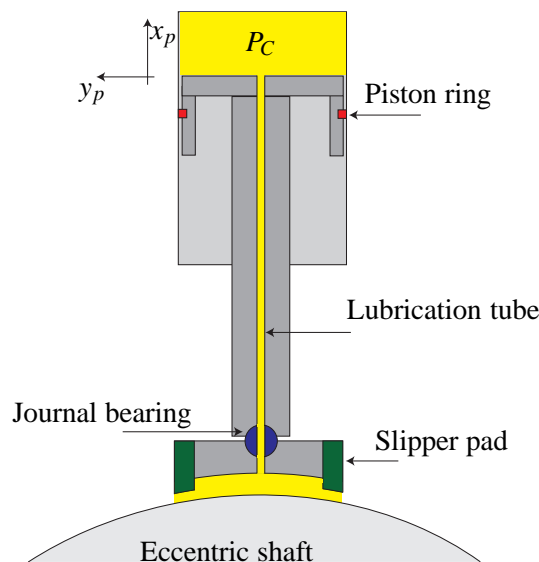


Figure 4.1.1: Piston, cylinder and piston rod connected with eccentric shaft. Yellow indicates the chambers containing oil, red indicate a piston ring, blue marks journal bearing, and green marks the slipper pad.

To reduce the leakage between piston and cylinders, piston rings can be installed; marked with red on Figure 4.1.1. Piston rings have high friction compared to washers but less leakage due to smaller clearances. The advantage of using piston rings instead of washers is the dynamic movement caused by the changing pressure in the piston groove behind the ring. This movement will decrease

the slit height between the ring and the cylinder wall during compression, and increase the height during decompression. This is consistent with the fact that if the cylinder compresses the pressure difference across the piston ring is high and low when the cylinder decompresses. The pressure and slit height development together is expected to keep the leakage to a minimum, thus this solution is examined in this project.

In Figure 4.1.1 only one piston ring is illustrated. If more rings were to be installed in the piston ring friction model, the complexity of the model would increase. By among others, a pressure would be added between the two rings largely increasing the simulation time. Since the computation time with one piston ring is high, e.g. two days, only one ring is applied here.

If more rings were added, the frictional force would increase due to larger surface area. However, if the rings were designed properly, the film height would also increase, hereby lowering the friction. This relation is not further examined in this project, but will be an area of interest if the piston ring model was to be expanded.

The journal bearing in Figure 4.1.1 is necessary, since the bearing will tilt due to the nature of the connection between the eccentric shaft and the slipper pad. The journal bearing is not included in the friction analysis of this project, and will therefore not be explained further. Instead the connection between the slipper pad and the piston rod is implemented as a rigid connection, which is aligned perfectly with the surface of the shaft.

4.2 Piston Ring Friction and Leakage

This section describes the piston ring friction model and the leakage between the cylinder and piston. The first section describes a selection of theories applicable for piston friction modelling. The next describes the chosen method and the way it is implemented as a model.

4.2.1 Piston Friction Theory

This section describes the piston ring friction model, and starts by summarising a selection of state-of-the-art methods resulting in a choice of model which is applied in this project. All methods available are derived from internal combustion engines (ICE), which in comparison to the PMC Servi pump, works at a significant lower pressure. E.g. the motor examined in [Akalin and Newaz, 2001] has a peak pressure of 5[bar] in approximately $1/12$ of a cycle, where as in the PMC Servi pump the pressure is 250[bar] in approximately $1/2$ of the cycle. This difference is due to the fact that an ICE is driven by a high-pressure explosion in a short period, where as the pump is driven by a continuous wind. Keeping the difference in mind the model can still be applied on the PMC Servi pump since the piston rings are similar.

The methods can roughly be separated into three groups:

1. Normal friction model by applying an approximated coefficient of friction and multiplying

this by the velocity.

2. Axisymmetrical piston and piston ring with a variable slit height between the piston ring and the cylinder wall.
3. Nonaxisymmetrical piston and piston ring. I.e. non-concentric slit height and a movement of the piston in the y -direction and the z -direction, cf. Figure 4.1.1.

The first method is the simplest and is often used in simple calculations. However, this cannot be applied in the modulation of piston ring friction, as the coefficient of friction is often experimentally determined.

The friction depends on piston velocity, slit height, cylinder pressure, surface roughness, and oil film temperature and viscosity. Thus the friction can be modelled more precisely by calculating the friction at each working point throughout the cycle.

A method produced by Patir and Cheng involves utilising a modified average Reynolds equation for rough surfaces [Patir and Cheng, 1979]. The method predicts the lubrication film thickness and the friction force, by including surface and shear-flow factors. This is the foundation of several other methods, e.g. by Rohde who formed a dynamically mixed lubrication model for piston rings, including asperity contact points [Rohde, 1980]. The average Reynolds equation for rough surfaces and asperity contacts will be applied in this project, and explained in the subsequent sections.

The axisymmetrical piston ring friction model is applied by Akalin and Newaz in a study of friction in the mixed lubrication regime [Akalin and Newaz, 2001]. In this model the piston is fixed and the piston ring can move radially as a function of the pressure on each side of the ring. By applying a non-dimensional numerical analysis they developed a dynamic model calculating the slit height, the slit height velocity, and the friction. This axisymmetrical model is chosen as the foundation of the friction model applied in this report.

A nonaxisymmetrical piston ring friction model was developed by Hu and Cheng [Hu and Cheng, 1994] which introduced a deflection of the piston ring. This introduces a more detailed modulation of the slit height but is also more demanding since the height is variable in the slit around the cylinder. A newly developed model was derived by Livanos and Kyrtatos [Livanos and Kyrtatos, 2007], introducing force and torque equilibrium of the piston. This model is one of the most advanced piston ring friction models available, as the piston can move and tilt in all directions inside the cylinder. If further development of the model presented in this project was desired, this method could be useful.

4.2.2 Chosen Lubrication Model

As mentioned the chosen lubrication model for this project is based on the axisymmetrical piston ring friction model developed by Akalin and Newaz [Akalin and Newaz, 2001].

4. Friction and Leakage Analysis

Note that this section has a different convention than the rest of the report: Capital P is dimensionless pressure, and lower case p marks pressure with dimensions.

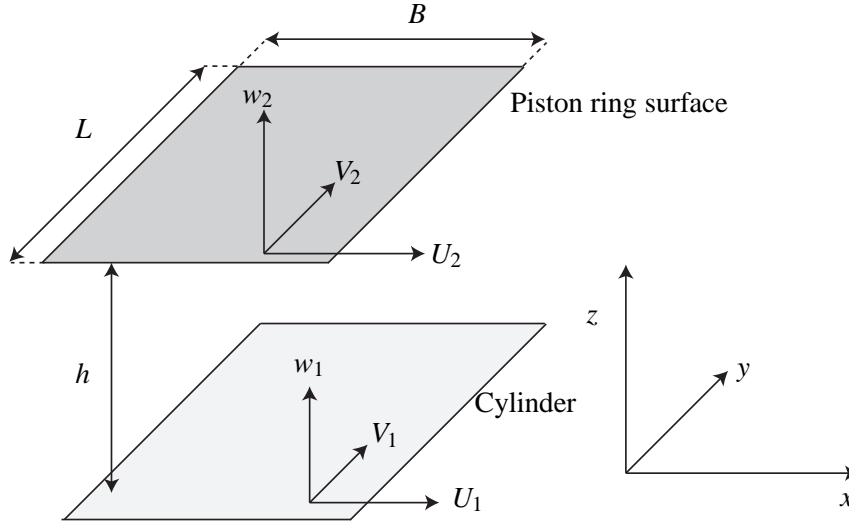


Figure 4.2.1: Flow between two plates.

The flow between two plates as illustrated in Figure 4.2.1 can be described by the Reynolds equation presented in Equation 4.1

$$\frac{\partial}{\partial x} \left[\frac{\rho h^3}{\mu} \frac{\partial p}{\partial x} \right] + \frac{\partial}{\partial y} \left[\frac{\rho h^3}{\mu} \frac{\partial p}{\partial y} \right] = 6 \left\{ \frac{\partial}{\partial x} \left[\rho h (U_1 + U_2) + \frac{\partial}{\partial y} \rho h (V_1 + V_2) \right] + 2 \frac{d}{dt} (\rho h) \right\} \quad (4.1)$$

where:	ρ	Density
	h	Fluid film height
	μ	Dynamic viscosity
	p	Pressure
	U	Velocity in x -direction
	V	Velocity in y -direction
	w	Velocity in z -direction

This equation is based on the following assumptions written with comments [Gohar and Rahnejat, 2008].

1. Oil film has negligible mass, such that gravity forces can be neglected. This assumption is valid since the mass of the fluid in the slit is low compared to the mass of the piston.
2. Pressure is constant in z -direction due to low film height compared with the length of the slit,

- cf. Figure 4.2.1. This assumption is valid since the distance in z -direction is significantly smaller than in x - or y -direction.
3. Newtonian fluid, which is valid since hydraulic fluid is a newtonian fluid.
 4. Lubricant flow is laminar due to low Reynolds no: The leakage flow is expected to be very low and so is the correctional opening area around the slit, thus it can be assumed to be laminar.
 5. Inertia and surface tension forces are negligible compared with viscous forces.
 6. Shear stress and velocity gradients are only significant in the z -direction. This is a valid assumption since the only movement is in the x -direction.
 7. Constant viscosity in the z -direction, is an acceptable assumption in this initial analysis as the height of the lubrication layer is much smaller than the dimensions in the the other directions.

Reynolds equation can be further simplified by assuming constant density and viscosity throughout the regime, but due to friction and movement of the fluid, the temperature will rise and hereby decrease the viscosity. The fluid film pressure is highly dependent on this and thus some analysis of the viscosity development throughout the cycle is necessary. However, due to constant replacement of the fluid, the assumption is considered acceptable. Density also changes with temperature and pressure, but due to the afore mentioned assumption the density can be assumed constant as well. This simplifies Equation 4.1 to:

$$\frac{1}{\mu} \frac{\partial}{\partial x} \left[h^3 \frac{\partial p}{\partial x} \right] + \frac{1}{\mu} \frac{\partial}{\partial y} \left[h^3 \frac{\partial p}{\partial y} \right] = 6 \left\{ \frac{\partial}{\partial x} \left[h(U_1 + U_2) + \frac{\partial}{\partial y} h(V_1 + V_2) \right] + 2 \frac{dh}{dt} h \right\} \quad (4.2)$$

When the flow in the slit between the piston ring and the cylinder is considered, the pressure distribution in the y -direction, equal to the z -direction on Figure 4.2.2, is also assumed to be constant, thus the Reynolds equation now becomes one-dimensional. To assume constant pressure in the y -direction, is a valid assumption, since no velocity components are present in that direction. Furthermore the piston ring only moves in one direction, and the cylinder is stationary, which simplifies Equation 4.2 to:

$$\begin{aligned} \frac{1}{\mu} \frac{\partial}{\partial x} \left[h^3 \frac{\partial p}{\partial x} \right] + \cancel{\frac{1}{\mu} \frac{\partial}{\partial y} \left[h^3 \frac{\partial p}{\partial y} \right]} &= 6 \left\{ \frac{\partial}{\partial x} \left[h \left(\cancel{U_1} + U_2 \right) + \cancel{\frac{\partial}{\partial y} h(V_1 + V_2)} \right] + 2 \frac{dh}{dt} h \right\} \\ \frac{1}{\mu} \frac{\partial}{\partial x} \left[h^3 \frac{\partial p}{\partial x} \right] &= 6 \left\{ \frac{\partial}{\partial x} \left[h U_2 + 2 \frac{dh}{dt} h \right] \right\} \end{aligned} \quad (4.3)$$

4. Friction and Leakage Analysis

Patir and Cheng modified the Reynolds equation to include the effects of surface roughness by introducing pressure and shear flow factors [Patir and Cheng, 1979]. This alters Equation 4.3 to:

$$\frac{1}{\mu} \frac{d}{dx} \left(\phi_x h^3 \frac{d\bar{p}}{dx} \right) = 6U \left(\frac{d\bar{h}_T}{dx} + \sigma \frac{d\phi_s}{dx} \right) + 12 \frac{d\bar{h}_T}{dt} \quad (4.4)$$

where:	ϕ_x	Flow factor comparing the average pressure flow on a rough surface to that of a smooth surface
	\bar{p}	Average pressure in a small area, $dydx$
	ϕ_s	Flow factor representing additional flow due to sliding in a rough bearing
	σ	Surface roughness
	U	The only velocity component in the equation, representing the movement of the piston with velocity U_2
	\bar{h}_T	Average height in a small area, $dydx$. Defined in Equation 4.5

All flow factors used in this chapter are described briefly in appendix D.

The pressure and heights in Equation 4.4 are approximated across a small area where the flow factors are well-defined; the flow factors are derived from mean flow quantities hence the pressures in Equation 4.4 are averaged across a small area. The fluid film height is approximated using the surface profiles of each surface, and is defined as in Equation 4.5. The exact formulas utilised for the flow factors are explained later in appendix D.1

$$h_T = h + \delta_1 + \delta_2 \quad (4.5)$$

where:	h_T	Fluid film height between two rough surfaces
	δ_1/δ_2	Surface roughness profiles of surface one and two respectively

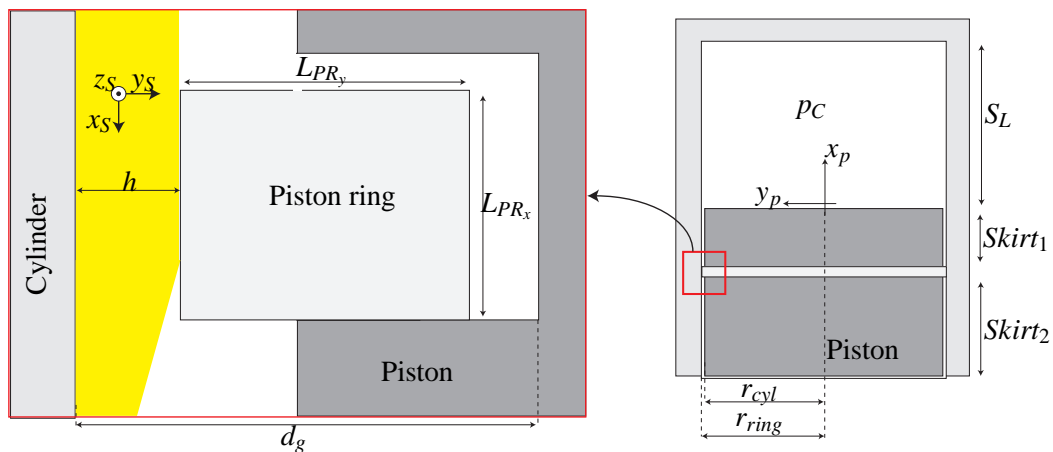


Figure 4.2.2: Piston ring. Lubricant film marked with yellow.

4.2.3 Altering the Chosen Model

The basic principle of Reynolds equation is now derived. To form a mathematical description of the piston ring illustrated on Figure 4.2.2, the problem can be converted to dimensionless [Akalin and Newaz, 2001]. To do this, the piston ring is illustrated with its respective notation in Figure 4.2.3.

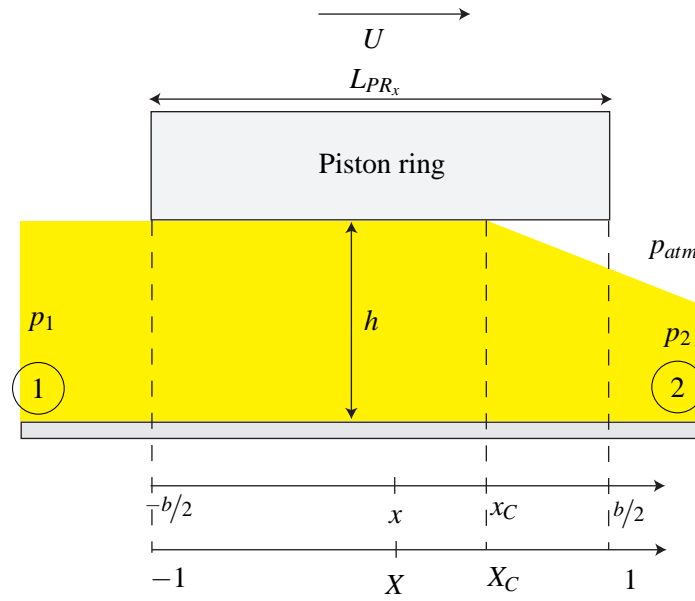


Figure 4.2.3: Piston ring geometry. x_c marks cavitation.

The boundary conditions are defined with dimensions in lower case letters and dimensionless in capital letters.

- At inlet, denoted as point 1, the pressure, pressure gradient, and position is defined as $p = p_1$, $x = -b/2$, $\partial p / \partial x = 0$ with dimensions and $P = P_1$, $dP/dX = 0$ and $X = -1$ as dimensionless.
- If cavitation occurs, the pressure in the fluid film is approximated by assuming atmospheric pressure, p_{atm} . This is widely accepted as an appropriate approximation if cavitation occurs in the film [Akalin and Newaz, 2001]. The cavitation point is denoted as x_c , and the pressure is set to p_{atm} with dimensions and X_C and P_{atm} as dimensionless.
- At outlet, denoted as point 2, the pressure, pressure gradient and position is defined as $p = p_2$, $\partial p / \partial x = 0$ $x = b/2$ with dimensions and $P = P_2$, $dP/dX = 0$, and $X = 1$ as dimensionless.

To convert Reynolds Equation, cf. Equation 4.4, to dimensionless form, a series of conversion

constants are defined:

$$X \equiv \frac{2x}{b} \quad H \equiv \frac{h}{c} \quad T \equiv t\omega \quad \beta \equiv \frac{b}{d} \quad (4.6)$$

$$U^* \equiv \frac{U}{d\omega} \quad P \equiv \bar{P} \frac{c^2}{3\mu d\omega b} \quad \sigma^* \equiv \frac{\sigma}{c} \quad \frac{dH}{dT} \equiv \dot{H} \quad (4.7)$$

These are substituted into Equation 4.4 along with contact flow factor, ϕ_f , cf. Equation D.2, and yields:

$$\frac{d}{dX} \left(\phi_x H^3 \frac{dP}{dX} \right) = U^* \left(\phi_c \frac{dH}{dX} + \sigma^* \frac{d\phi_s}{dX} \right) + \beta \phi_c \dot{H} \quad (4.8)$$

Note that the derivatives are not partial any more. This is done by assuming that H is only dependent on X and time. By integrating Equation 4.8 the pressure distribution is given in Equation 4.9:

$$\phi_x H^3 \frac{dP}{dX} = U^* \int_{-1}^{X'} \phi_c \frac{dH}{dX} dX + U^* \sigma^* \int_{-1}^{X'} \frac{d\phi_s}{dX} dX + \beta \dot{H} \int_{-1}^{X'} \phi_c dX + C_1 \quad (4.9)$$

where: X' Variabel upper integration limit

C_1 Integration constant

The dimensionless fluid film height, H , is in this design independent on X , since the fluid height is constant throughout the slit. This assumption can only be done if the surface of the piston ring is aligned perfectly with the cylinder surface, and if the ring profile is completely flat. If this was not the case the fluid film height would be a function of X , and further examinations of friction, lubrication, and wear should be conducted in order to design an appropriate ring profile. These examinations are not a part of this project, thus H is constant along the X -direction.

H and the flow factors ϕ_c and ϕ_s are independent of X , and are moved out of the integrals. Furthermore, integration of $\frac{dH}{dX}$ with respect to X results in H , and by isolating $\frac{dP}{dX}$ in Equation 4.9, Equation 4.10 occurs.

$$\frac{dP}{dX'} = \frac{U^* (\phi_c H + \sigma^* \phi_s)}{\phi_x H^3} + \frac{\phi_c \beta \dot{H} (X' + 1)}{\phi_x H^3} + \frac{C_1}{\phi_x H^3} \quad (4.10)$$

By integrating with respect to X' , and by recalling that H is constant for any X' , Equation 4.11 is derived.

$$P(X'', T) = \int_{-1}^{X''} \frac{U^* (\phi_c H + \sigma^* \phi_s)}{\phi_x H^3} dX' + \int_{-1}^{X''} \frac{\beta \dot{H} \phi_c (X' + 1)}{\phi_x H^3} dX' + \int_{-1}^{X''} \frac{C_1}{\phi_x H^3} dX' + C_2 \quad (4.11)$$

where: C_2 Integration constant

where: X'' Variabel upper integration limit

Returning to Equation 4.11, the flow factors and fluid film height are, as mentioned earlier, not dependent on X and are moved outside of the integrals along with H .

$$P(X'', T) = U^* \underbrace{\frac{(\phi_c H + \sigma^* \phi_s)}{\phi_x H^3} \int_{-1}^{X''} dX'}_{J_1(X'')} + \underbrace{\frac{\beta \frac{dH}{dT} \phi_c}{\phi_x H^3} \int_{-1}^{X''} (X' + 1) dX'}_{J_2(X'')} + C_1 \underbrace{\frac{2}{\phi_x H^3} \int_{-1}^X dX'}_{J_3(X'')} \quad (4.12)$$

The integral marked with $J_1(X'')$ in Equation 4.12 is calculated in Equation 4.13.

$$J_1(X'') = \frac{(\phi_c H + \sigma^* \phi_s)}{\phi_x H^3} \int_{-1}^{X''} dX' = \frac{(\phi_c H + \sigma^* \phi_s)}{\phi_x H^3} (X'' + 1) \quad (4.13)$$

$J_2(X'')$ in Equation 4.12 is calculated in Equation 4.14.

$$J_2(X'') = \int_{-1}^{X''} (X' + 1) dX' = \left[\frac{1}{2} X'^2 + X' \right]_{-1}^{X''} = \frac{1}{2} (X'')^2 + X'' + \frac{1}{2} \quad (4.14)$$

$J_3(X'')$ in Equation 4.12 is calculated in Equation 4.15.

$$J_3(X'') = \frac{1}{\phi_x H^3} \int_{-1}^{X''} dX' = \frac{1}{\phi_x H^3} (X'' + 1) \quad (4.15)$$

Inserting the integrals into Equation 4.12, and replacing X'' with X , since X'' is the only remaining version of X , the dimensionless pressure distribution is defined as:

$$P(X, T) = \frac{U^* (\phi_c H + \sigma^* \phi_s) (X + 1)}{\phi_x H^3} + \frac{\beta \dot{H} \phi_c \left(\frac{1}{2} (X)^2 + X + \frac{1}{2} \right)}{\phi_x H^3} + \frac{C_1 (X + 1)}{\phi_x H^3} + C_2 \quad (4.16)$$

The two integration constants can be defined from the boundary conditions mentioned earlier:

C_2 must satisfy that the pressure at $X = -1$ is equal to P_1 , resulting in $C_2 = P_1$. C_1 must satisfy that the pressure at $X = 1$ or $X = X_C$ is equal to P_2 , for fully flooded or cavitation condition respectively.

C_1 for fully flooded and C_{1x_C} for cavitation are respectively defined as:

$$\begin{aligned} C_1 &= \frac{P_2 - P_1 - U^* J_{1(X=1)} - \beta \dot{H} J_{2(X=1)}}{J_{3(X=1)}} \\ &= \frac{P_2 - P_1 - U^* \frac{(\phi_c H + \sigma^* \phi_s)}{\phi_s H^3} 2 - \beta \dot{H} 2}{\frac{1}{\phi_s H^3} 2} \end{aligned} \quad (4.17)$$

$$\begin{aligned} C_{1x_C} &= \frac{P_2 - P_1 - U^* J_{1(X=X_C)} - \beta \dot{H} J_{2(X=X_C)}}{J_{3(X=X_C)}} \\ &= \frac{P_2 - P_1 - U^* \frac{(\phi_c H + \sigma^* \phi_s)}{\phi_s H^3} (X_C + 1) - \beta \dot{H} \left(\frac{1}{2} (X_C)^2 + X_C + \frac{1}{2} \right)}{\frac{1}{\phi_s H^3} (X + 1)} \end{aligned} \quad (4.18)$$

The pressure distribution is now derived and will be applied in the following section to describe the force equilibrium.

4.2.4 Force Equilibrium of Piston Ring

To complete the piston ring model, a force equilibrium of the forces acting on the ring is needed. A segment of the piston ring is illustrated on Figure 4.2.4 with forces acting on it.

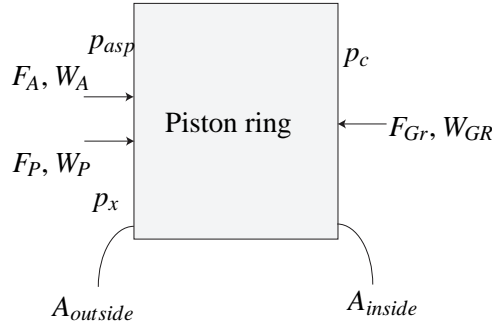


Figure 4.2.4: Force equilibrium.

where:	F_{GR}	Force caused by pressure between piston ring and piston, denoted groove force.
	W_{GR}	Dimensionless load form of F_{GR}
	F_A	Force caused by contact with asperities
	W_A	Dimensionless load form of F_A
	F_P	Force caused by pressure in fluid film
	W_P	Dimensionless load form of F_P
	p_{asp}	Contact pressure caused by asperities

p_x	Fluid film pressure
A_{inside}	Inside surface area of piston ring
$A_{outside}$	Outside surface area of piston ring

The inside and outside area are defined in Equation 4.19 and 4.20 respectively. Note that the enlargement of the ring is neglected when the surface area is calculated. This is valid, as the surface area increment due to increased radius is small compared with the size of the surface areas.

$$A_{inside} = d\theta(r_{ring} - L_{PR_y})L_{PR_x} \quad (4.19)$$

$$A_{outside} = d\theta r_{ring} L_{PR_x} \quad (4.20)$$

The force equilibrium is written in dimensional form in Equation 4.21 and as a load equilibrium in Equation 4.22. The mass of the piston is neglected such that the sum of forces always equals zero.

Furthermore no distortion force is included: This means that the piston ring is not pressed towards the cylinder wall and hereby does not create a tension force towards the cylinder wall, thus lowering the fluid film height additionally. If this force was to be implemented in the force equilibrium, it could be modelled as an equivalent spring force. This spring force has a stiffness deduced from the material and geometry of the ring, and has a distortion equal to the deflection of the ring with atmospheric fluid film pressure. By not including this force, the calculated power loss will be an optimistic estimate in regards to the overall efficiency.

$$\sum F_{PR} = F_P + F_A + F_{GR} = 0 \quad (4.21)$$

$$\sum W_{PR} = W_P + W_A + W_{GR} = 0 \quad (4.22)$$

The forces are described in the following.

4.2.4.1 Force Caused by Pressure in Fluid Film F_P

As mentioned earlier, the cavitation pressure is set to p_{atm}/P_2 , hence all pressures after the cavitation point, X_C , are set to p_{atm} . To implement this, two functions, ψ_P and ψ_{atm} monitoring $P(X, T)$ are applied, as explained in Equation 4.23 and 4.24.

$$\psi_P(P) = \begin{cases} 1 & \text{for } P(X, T) > P_2 \\ 0 & \text{for } P(X, T) < P_2 \end{cases} \quad (4.23)$$

$$\psi_{atm}(P) = \begin{cases} 0 & \text{for } P > P_2 \\ 1 & \text{for } P < P_2 \end{cases} \quad (4.24)$$

These functions are applied when the load W_P is calculated:

$$W_P = \int_{-1}^1 P(X, T) \psi_P(P) + P_2 \psi_{atm}(P) dX \quad (4.25)$$

When the force F_P is calculated, the constants used under the derivation of $P(X, T)$, cf. Equation 4.6 and 4.7, are now reinserted.

$$F_P = L \cdot \int_{-1}^1 P(X, T) \psi_P(P) + P_2 \psi_{atm}(P) dX \cdot \frac{b}{2} \cdot \frac{3\mu d\omega b}{c^2} \quad (4.26)$$

where: L Length of an arcpiece on the outside surface of the ring, equal to $d\theta r_{ring}$

4.2.4.2 Force Caused By Asperities, F_A

If the fluid film height is below a certain ratio, Ω , the asperities of the surface are in contact with each other and the asperity force F_A is present. A model was derived by Greenwood and Tripp concerning this force, which was later approximated by Hu and Cheng [Tripp, 1971] [Hu and Cheng, 1994]. The approximated model is explained briefly here, and all constants are copied directly from [Hu and Cheng, 1994].

The average contact pressure p_{asp} is defined in Equation 4.27

$$p_{asp} = K \cdot E' \cdot F_{2.5}(H_\sigma) \quad (4.27)$$

Where the constants are given in Equation 4.28, 4.29 and 4.30

$$K = \frac{8\sqrt{2}}{15} \pi (N\beta'\sigma) \sqrt{\frac{\sigma}{\beta'}} \quad (4.28)$$

where: (N) Number of asperities per unit area
 β' Asperity radius of curvature
 $(N\beta'\sigma)$ Constant 0.04

$$\sqrt{\frac{\sigma}{\beta'}} \quad \text{Constant } 0.001$$

$$E' = \frac{2}{\left(\frac{1-\nu_1^2}{E_1} + \frac{1-\nu_2^2}{E_2}\right)} \quad (4.29)$$

where: $\nu_{1/2}$ Possions ratio of material 1 or 2
 $E_{1/2}$ Young's Modulus of material 1 or 2

$$F_{2.5}(H_\sigma) = \begin{cases} A(\Omega - H_\sigma)^Z & \text{for } H_\sigma \leq \Omega \\ 0 & \text{for } H_\sigma > \Omega \end{cases} \quad (4.30)$$

where: Ω Constant 4.0
 A Constant $4.4068 \cdot 10^{-5}$
 Z Constant 6.804

The constants are inserted in the contact pressure in Equation 4.27 and integrated through the slit to form the load W_A and the force F_A :

$$W_A = \int_{-b/2}^{b/2} p_{asp} dx \quad (4.31)$$

$$F_A = L \cdot \int_{-b/2}^{b/2} p_{asp} dx \quad (4.32)$$

From Equation 4.30 it is clear that when $H_\sigma > 4$, as $\Omega = 4$, p_{asp} is equal to zero, and only viscous friction is present.

4.2.4.3 Groove Force, F_{GR}

The groove force caused by the pressure in the piston groove forces the ring towards the cylinder wall. The pressure in the groove is assumed to be equal to the cylinder pressure. This assumption is valid if the pressure does not change significantly across the slit marked with $Skirt_1$ on Figure 4.2.2. $\frac{dp}{dx}$, cf. Equation 4.8, in this slit is significantly lower, than $\frac{dp}{dx}$ across the piston ring due to a higher fluid film height which is approximated to: $r_{cyl} - r_{ring} \approx 1[mm]$. Since $\frac{dp}{dx}$ has a $\frac{1}{h^3}$

dependency, the pressure drop across $Skirt_1$ and $Skirt_2$ is considerably lower than across the ring.

$$W_{GR} = L_{PR_x} p_c \quad (4.33)$$

$$F_{GR} = A_{inside} p_c \quad (4.34)$$

where: A_{inside} Inside area of piston ring, cf. Equation 4.19

The forces acting on the piston ring is now defined and a numerical method will be applied to solve it. This is explained in the following section.

4.2.5 Implementation of the Piston Ring Friction Model

To solve the force equilibrium the current fluid height, h , and squeeze film, \dot{h} , is needed. No exact formula for calculating \dot{h} , such that the force equilibrium equals zero, exists. Instead a numerical method is applied and is explained in the following:

1. Initial guess of fluid film height h_{ini} is chosen.
2. Two guesses of squeeze film are made: \dot{h}_{min_1} and \dot{h}_{max_1} , and in the center between these \dot{h}_{mid_1} is set. All illustrated in Figure 4.2.5.
3. The force equilibrium is calculated three times with $h = h_{ini}$ and with \dot{h} equal to each of the guesses.
4. To examine if one of the three chosen \dot{h} is within the converge criteria of the force equilibrium, C_{con} , the latter is compared with each of the three \dot{h} . If the result of the force equilibrium is above zero, a plus is inserted in the sign vector, \vec{e}_{sign_1} , and likewise for minus, illustrated in Figure 4.2.5. The converge criteria is defined as an interval of $\pm C_{con}$ around \dot{h}_{sol} .
5. If the sign of \vec{e}_{sign_1} is changing, as between \dot{h}_{min_1} and \dot{h}_{mid_1} . A solution exists between these two \dot{h} . The solver now sets a new set of \dot{h} guesses: \dot{h}_{min_2} and \dot{h}_{max_2} and computes \dot{h}_{mid_2} .
6. The solver now calculates a new sign vector, \vec{e}_{sign_2} , from the force equilibrium and iterates this step 3 to 5 until the solution is within the converge criteria, C_{con} , or hits the exact solution \dot{h}_{sol} . In iteration no. 3 in Figure 4.2.5, \dot{h}_{mid_3} is within C_{con} and a satisfactory solution is found.

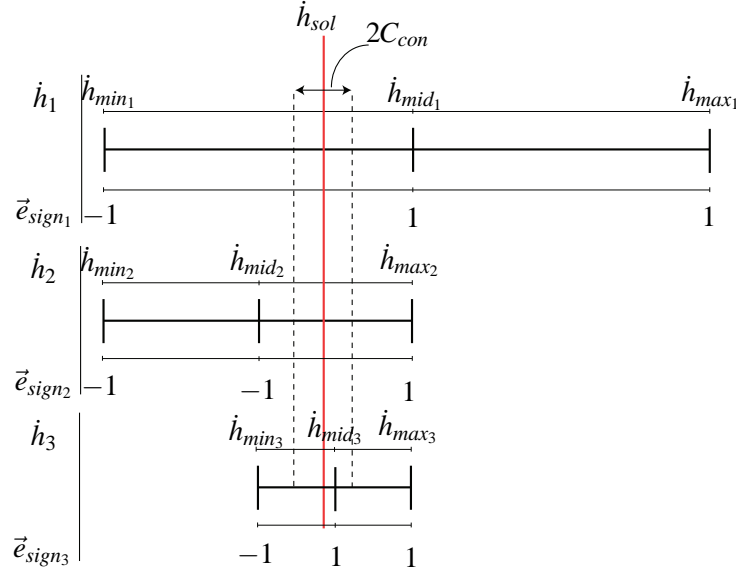


Figure 4.2.5: Numerical method explanation.

The \dot{h} solution to the force equilibrium is the output of this function and is integrated to obtain the fluid film height, as illustrated in the block diagram on Figure 4.2.6.

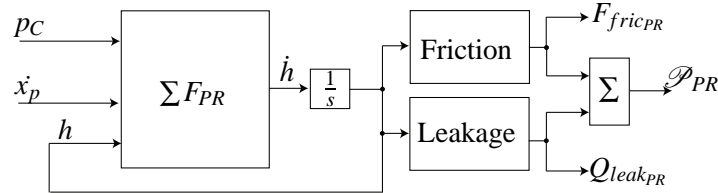


Figure 4.2.6: Piston ring friction model.

The leakage from the gap between the piston ring and cylinder wall is calculated in Equation 4.35, by assuming steady laminar flow. This assumption is valid due to small cross-sectional area and expected low leakage flow.

$$Q_{leak_{PR}} = \frac{\Delta p 2\pi r_{cyl} h^3}{12\mu L_{PR_x}} \quad (4.35)$$

where: Δp Pressure difference across piston ring, equal to $p_{cyl} - p_{atm}$

The friction force is calculated from Equation 4.36 [Hu and Cheng, 1994].

$$F_{fric} = -sign(U) \left\{ \frac{\mu|U|}{h} [(\phi_f - \phi_{fs}) + 2V_{r1}\phi_{fs}] + c_f p_{asp} \right\} 2\pi r_{cyl} L_{PR_x} \quad (4.36)$$

4. Friction and Leakage Analysis

where:	U	Velocity of the piston ring, equal to \dot{x}_p
	ϕ_f	Shear stress flow factor which concerns the average of the sliding velocity component of the shear stress, c.f. section D.1.4 in appendix for a calculation of this.
	ϕ_{fs}	Shear stress flow factor which concerns the combined effect of the roughness and the sliding, c.f. section D.1.4 in appendix for a description. This is equal to zero when the surface roughnesses of both surfaces are equal.
	V_{r1}	Variance ratio between the two surfaces, this is equal to 1 when the surface roughnesses of both surfaces are equal

The friction caused by the skirts of the piston, cf. $Skirt_1$ and $Skirt_2$ in Figure 4.2.2, is distinctively smaller than for the piston ring, since the clearance is significant larger. e.g. in the order of 10-1000 times larger.

The leakage is feedback to the continuity Equation of the cylinder chamber, and the friction is feedback to the force equilibrium of the piston in the mechanic. The total power loss due to leakage and friction, \mathcal{P}_{PR} , is calculated in Equation 4.37

$$\mathcal{P}_{PR} = Q_{leak_{PR}}(p_{cyl} - p_{atm}) + F_{fric_{PR}}\dot{x}_p \quad (4.37)$$

The piston ring friction model has now been derived and is connected to the non-linear model by inserting the frictional force $F_{fric}\hat{x}$ into the force equilibrium of the cylinder, cf. Equation 2.2. The leakage is inserted as a flow out of the cylinder chamber in the continuity equation of the cylinder, cf. Equation 2.30.

4.3 Slipper Pad Friction and Leakage

The friction between the piston rod and the eccentric shaft is an essential part of the power loss, which needs to be accounted for when the pump is analysed, thus this will be the main focus for the subsequent section.

Slipper pads have been used in several applications where a piston presses against a planar surface. Cunningham and McGillavary explored the slipper pad bearing applied in a radial piston motor and have established several design criteria for that particular design [Cunningham and McGillavary, 1965]. Koc and Hooke conducts an experimental investigation of orifice compensated slipper pad bearings in axial piston pumps and motors [Koč and Hooke, 1996]. It is here established that with larger orifice diameter, the clearance between the surfaces is increased compared to bearings with no orifice. Furthermore, it is determined that sufficient oil jet pressure is required to prevent oil starvation. Koc and Hooke also analyses a swash plate pump where it is shown that for successful operation, the slipper pad needs to have small amounts of non-flatness on the running surface [Koč and Hooke, 1998]. None of the latter investigates the friction derived from the use of these bearings. This is investigated by Canbulat, Sinanglu, and Koc in an experimental analysis where frictional power losses are found to be caused by surface roughness, capillary tube diameter, the

size of the hydrostatic bearing area, supply pressure, and the relative velocity [Canbulut et al., 2009]. It is concluded that the frictional loss decreases with increasing capillary tube diameter and supply pressure. In the following the friction model obtained in section 4.2 will be applied to model the friction between the eccentric shaft and the piston rod with a capillary compensated slipper pad bearing.

4.3.1 Capillary Compensated Slipper Pad Bearing

The bearing between the eccentric shaft and the piston rod is a capillary compensated slipper pad bearing. This kind of bearing is supplied with a lubricant from the cylinder chamber through a capillary tube into a pocket under the bearing, this is illustrated in Figure 4.3.1. The slipper pad pocket ensures a great reduction in friction and thus only the friction between the eccentric shaft and the lands are taken into account. This is valid as the height of the lubrication layer is substantially larger within the pocket than under the lands, and thus the friction from this part is substantially smaller. The argument for this is the same as with the friction of the piston skirt compared to the piston ring, cf. section 4.2.5. The friction from the pocket is thus neglected in the overall calculation of the friction. The pocket stands for the major part of the force which acts on the piston from the lubricant. Because of the afore mentioned height of the lubrication layer, the pressure drop from the exit of the capillary tube to the lands is also very small and is neglected so that the pressure in the pocket is constant. An essential part of the design of the slipper pad bearing is the assumption of constant height through the slit under the land. This requires the profile of the slipper pad bearing to have the same curvature as the eccentric shaft. This can also be seen on Figure 4.3.1 where the lands as well as the ceiling of the pocket have the same curvature as the eccentric shaft. Note that capital P now is referring to pressure with dimensions.

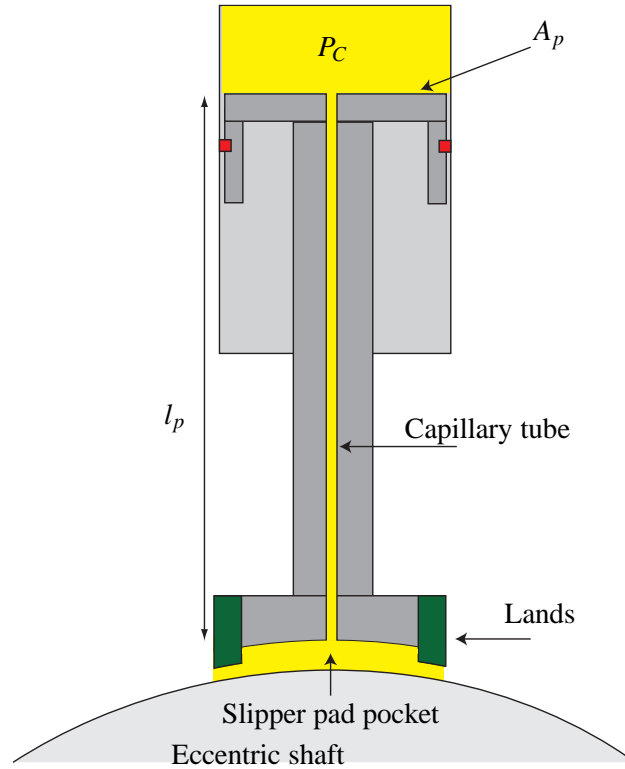


Figure 4.3.1: One piston with the capillary compensated slipper pad bearing illustrated. Fluid is denoted with yellow.

The friction is modelled by analysing the flow in and out of the slipper pad pocket to determine the pressure in the pocket and from this determine the force which acts on the piston. First the flow under the lands, i.e. the leakage flow, is determined by use of [Watton, 2009]:

$$Q_{Land_i} = \frac{L_i h_{land}^3 (P_{BP} - P_{atm})}{12 \mu w_{BR}} \quad (4.38)$$

where:

Q_{Land_i}	Leakage flow under land i .
i	Denotes the land in question
w_{BR}	Width of the land.
h_{land}	Height of the fluid film between the eccentric shaft and the land.
P_{BP}	Pressure in the pocket.
L_i	Length of the land. Equal to L_1, L_2, L_3 or L_4

Equation 4.38 is applied on all four parts of the land with the lengths and widths as denoted on Figure 4.3.2. The pressure distribution is nonlinear through the corners [Cunningham and McGillavary, 1965] and it is thus modelled by applying the lengths L_{1-4} depending on the land in question. L_1

and L_2 is given as $L_H - w_{BR}$ and L_3 and L_4 is given as $L_W - w_{BR}$ as illustrated on Figure 4.3.2. The flow out under land 1 and 2 can be written as a sum of the Couette flow caused by the surface velocity and the Poiseuille caused by the pressure difference across the land.

$$\begin{aligned} Q_{Land_1} &= -Q_{Poiseuille} - Q_{Couette} \\ Q_{Land_2} &= -Q_{Poiseuille} + Q_{Couette} \\ Q_{Land_1} + Q_{Land_2} &= -2Q_{Poiseuille} \end{aligned} \quad (4.39)$$

$Q_{Poiseuille}$ for land 1 and 2 are equal due to the pressure difference across the land and the width are equal, cf. Figure 4.3.2. $Q_{Couette}$ is equal for land 1 and 2, but with different sign, due to equal surface velocity. But from the perspective of the slipper pad pocket, one is directed into the pocket and the other outwards.

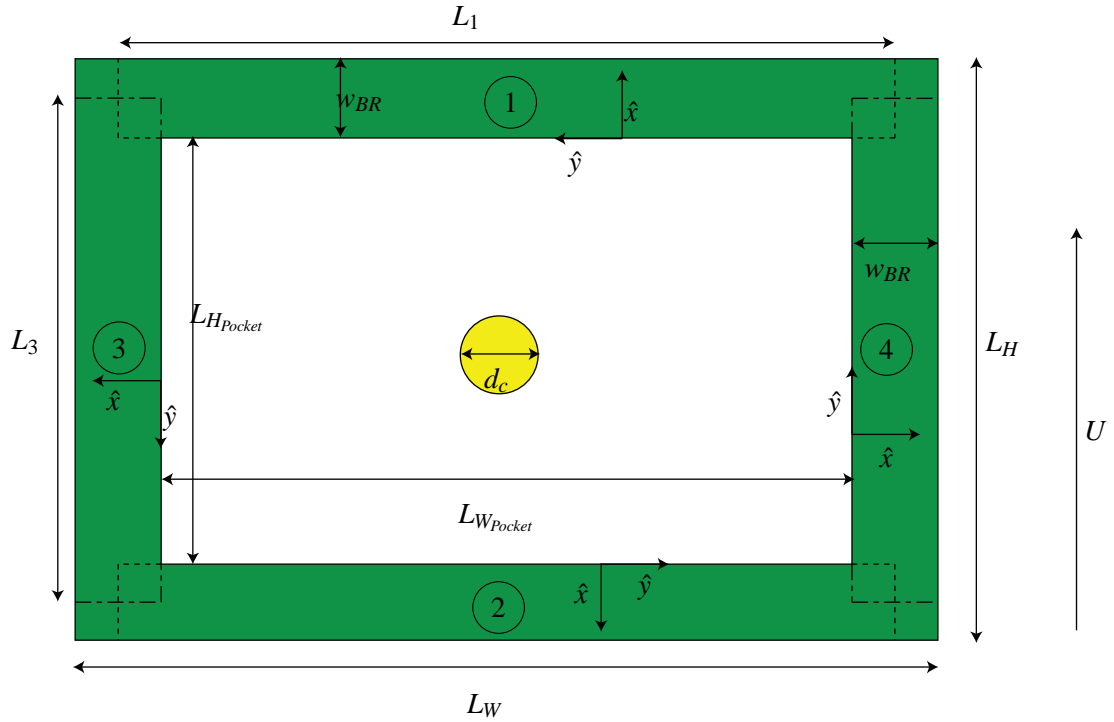


Figure 4.3.2: Slipper pad bearing from below. Lands are illustrated with green. $L_1 = L_2$ and $L_3 = L_4$ though only L_1 and L_3 are presented on the Figure. The unity vectors on the lands indicate the directions applied in Equation 4.46.

$$Q_{leak_{sp}} = 2Q_{Land_1} + 2Q_{Land_3} \quad (4.40)$$

The flow through the capillary tube from the cylinder chamber to the slipper pad pocket is deter-

4. Friction and Leakage Analysis

mined by Equation 4.41 and by isolating P_{BP} , Equation 4.42 is obtained [Watton, 2009]:

$$Q_{Cap} = \frac{\pi d_c^4 (P_C - P_{BP})}{128 \mu l_p} \quad (4.41)$$

$$P_{BP} = -\frac{Q_{Cap} 128 \mu l_p}{\pi d_c^4} + P_C \quad (4.42)$$

where: Q_{Cap} Flow through capillary tube.
 d_c Diameter of capillary tube
 l_p Length of piston and piston rod.

By assuming that the volume in the slipper pad pocket is sufficiently small as the height of the slipper pad pocket is small, the pressure inside the pocket can be said to adjust instantaneously such that the continuity requires equal flow in and out of the pocket at all times:

$$Q_{Cap} = Q_{leak_{tot}} \quad (4.43)$$

By assuming that the mass of the piston is negligible due to the small accelerations relative to the eccentric shaft, an equilibrium of forces can be established as:

$$F_{cyl} = F_{pocket} + F_{Lands} \quad (4.44)$$

where: F_{pocket} Force from pocket acting on the piston.
 F_{Lands} Force from lands acting on the piston.

F_{cyl} is defined as given in Equation 2.3.

Recall that P_{BP} is constant then the force from the pocket acting on the piston is given as:

$$F_{pocket} = (L_W - 2w_{BR})(L_H - 2w_{BR})P_{BP} \quad (4.45)$$

The force from the lands are calculated by applying the same method as described in section 4.2.4.1 such that:

$$F_{Lands-i} = \int \int P_{Land-i}(x_i, y_i) dx_i dy_i \quad (4.46)$$

where: $P_{Land-i}(x_i, y_i)$ Pressure as a function of the position under land no. i

The pressure distribution for each land, is calculated from the P_{BP} -pressure side to the P_{atm} -side

in the \hat{x} -direction cf. Figure 4.3.2. Land 3 and 4 contributes to the pressure distribution due to the velocity of the surface under the land, this is illustrated in Figure 4.3.4. This contribution is calculated as given in section 4.3.5, but with the boundaries stated as in Figure 4.3.4. The length of the land given in Figure 4.3.4 is applied in order to calculate the pressure in the corners, as illustrated in Figure 4.3.2 and 4.3.3.



Figure 4.3.3: Close-up of the corner of the land, the white part of the corner shows where no pressure distribution is modelled. The dark grey part represents the part of the corner where only the horizontal land is modelled. The light grey represents a part where only the vertical land is modelled, and in the black part, both lands are modelled.

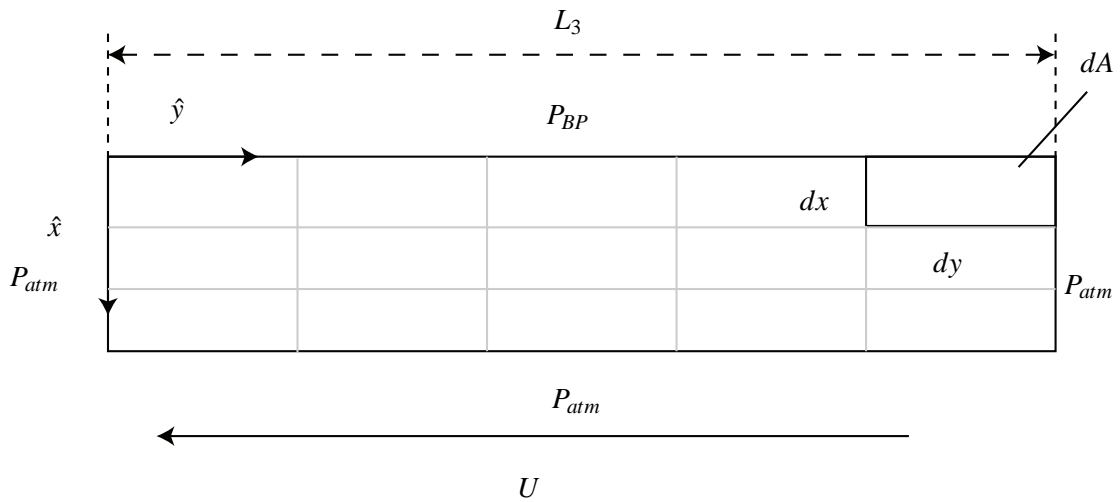


Figure 4.3.4: Land 3 with emphasis on the pressure distribution. For clarity dx and dy are made larger than what is actually utilised in the calculation.

By taking the sum of the pressure distribution in both the \hat{x} -direction and the \hat{y} -direction the total pressure under the land is found at all (x,y) -coordinates, illustrated in Figure 4.3.5. From this it is possible to calculate the total force caused by the pressure by applying Equation 4.46. Note that Land 1 and 2 only has the contribution from the \hat{x} -direction as the surface velocity and the direction of the pressure drop is parallel.

4. Friction and Leakage Analysis

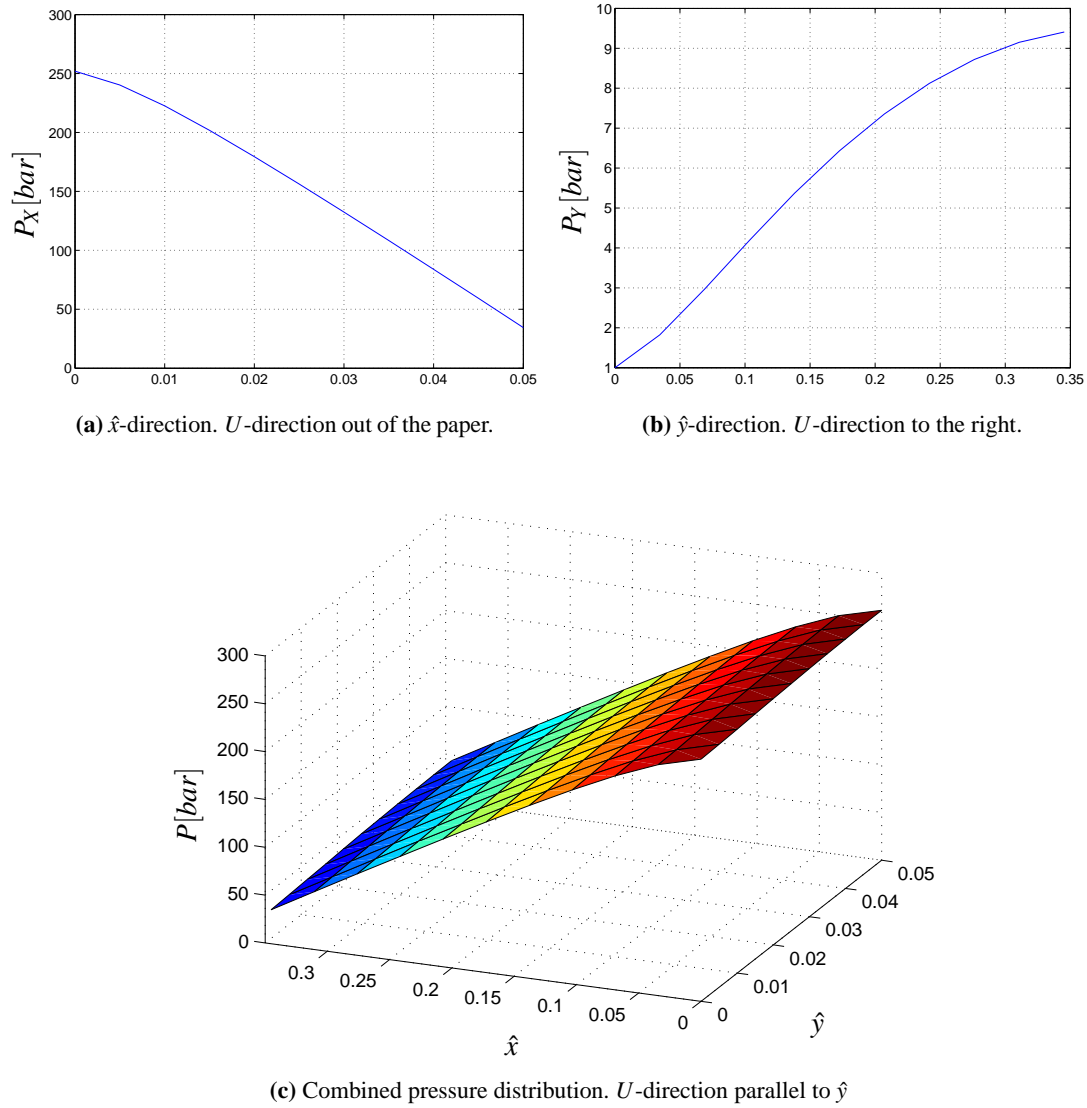


Figure 4.3.5: Pressure distribution in Land 3. Figure (c) illustrates the combined pressure distribution from (a) and (b).

The force from all the lands are summed to a total force, F_{Lands} . By substituting Equation 4.45 and 4.46 into Equation 4.44 and applying the same numeric solver as described in section 4.2.5, \dot{h}_{land} and h_{land} can be determined. This is illustrated in a block-diagram presented in Figure 4.3.6.

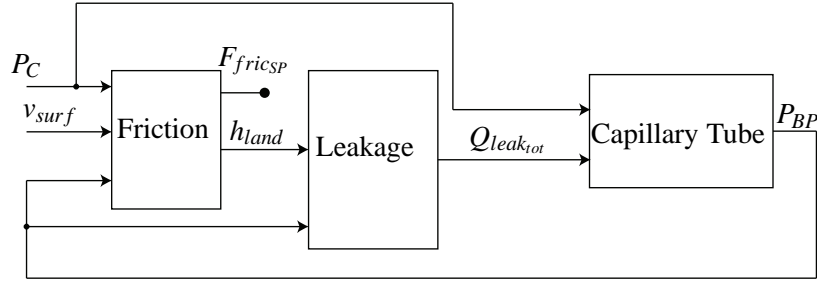


Figure 4.3.6: Block diagram which illustrates the friction and leakage flow of the slipper pad bearing. The friction block contains the friction computation, force equilibrium, and the numeric solver.

Now the friction force of the slipper pad can be determined by applying Equation 4.36 such that

$$F_{fric_{sp}} = -\text{sign}(v_{surf}) \frac{\mu |v_{surf}|}{h_{land}} \{ [(\phi_f - \phi_{fs}) + 2V_{r1}\phi_{fs}] + P_{asp_{land}} c_f \} (L_W L_H - (L_W - 2w_{BR})(L_H - 2w_{BR})) \quad (4.47)$$

where: $F_{fric_{sp}}$ Friction force between slipper pad bearing and eccentric shaft.
 v_{surf} Velocity of the surface of the eccentric shaft relative to the slipper pad bearing.
 $P_{asp_{land}}$ Contact pressure between land and eccentric shaft.

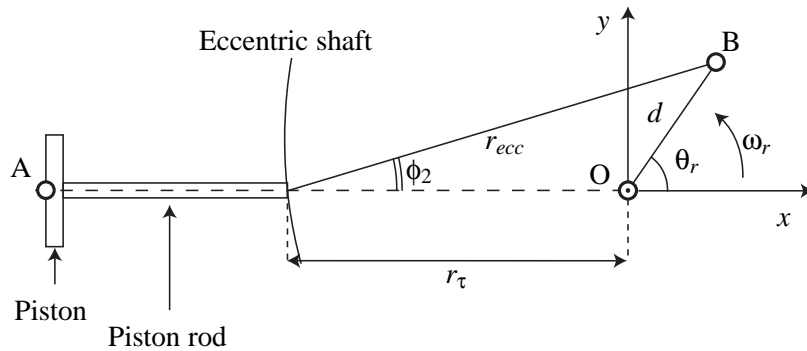


Figure 4.3.7: Illustration of the angles and lengths utilised to compute the surface velocity of the eccentric shaft.

The surface velocity relative to the slipper pad bearing is determined by calculating the distance from point O to the surface of the eccentric shaft as a function of θ_r . By applying the angles and lengths illustrated in Figure 4.3.7 and with ϕ_2 given as $\phi_2 = \sin^{-1}(\sin(\theta_r, d)/r_{ecc})$ the surface velocity,

v_{surf} , is:

$$r_\tau = r_{ecc} \cos(\phi_2) - d \cos(\theta_r) \quad (4.48)$$

$$v_{surf} = r_\tau \omega_r \quad (4.49)$$

The surface velocity is plotted in Figure 4.3.8.

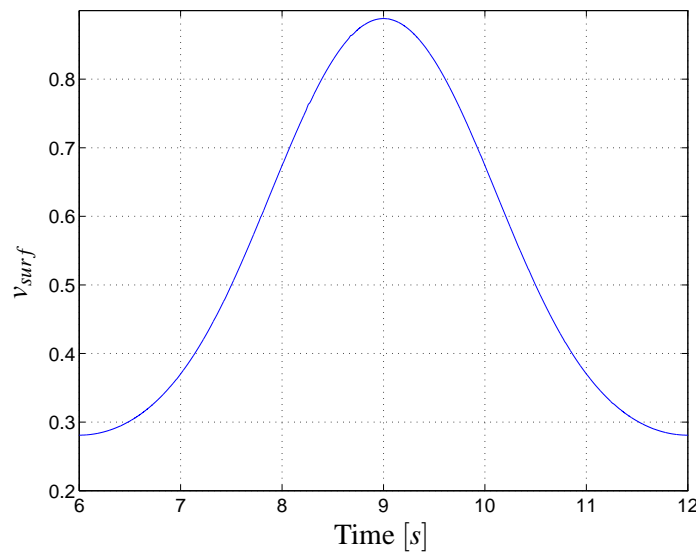


Figure 4.3.8: Surface velocity of the eccentric shaft at the slipper pad.

Now that the losses in the slipper pad are fully defined, the friction force and the leakage flow are connected to the rest of the non-linear model: The friction force, in Equation 4.47, is connected to the torque equilibrium around the rotor by multiplication with r_τ , cf. Equation 4.48, and the leakage, in Equation 4.40 is connected to the continuity equation, cf. Equation 2.30, as a flow out of the cylinder.

4.3.2 Optimal Film Height

The total power loss of the slipper pad is a function of leakage and frictional losses. If the fluid film height is high, the leakage is high, and if the fluid film height is low the frictional force is high, as illustrated in Figure 4.3.9

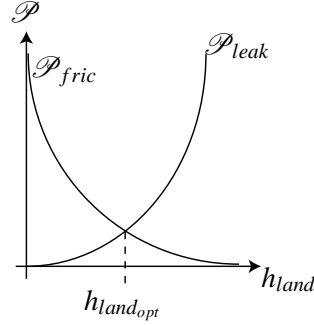


Figure 4.3.9: Power loss as a function of fluid film height for two arbitrary friction and leakage losses.

This indicates that some optimum h_{land} exists, but before evaluating this optimum $h_{land_{opt}}$, a choice of dimensioning constants are required. First the total power loss is found:

$$\mathcal{P}_{SP} = Q_{leak_{SP}} (P_C - P_{atm}) + F_{fric_{SP}} v_{surf} \quad (4.50)$$

From Equation 4.38 and 4.47 respectively, the leakage flow and the magnitude of the frictional force can be found to:

$$Q_{leak_{SP}} = 2 \frac{L_1 h_{land}^3 (P_{BP} - P_{atm})}{12 \mu w_{BR}} + 2 \frac{L_3 h_{land}^3 (P_{BP} - P_{atm})}{12 \mu w_{BR}} \quad (4.51)$$

$$F_{fric_{SP}} = \frac{\mu v_{surf}}{h_{land}} (L_W L_H - (L_W - 2w_{land})(L_H - 2w_{land})) \quad (4.52)$$

Notice that $P_{asp_{land}} = 0$, since the optimum is expected to be outside of the asperity region.

The optimisation parameters are, the ratio between the area of the piston and the pocket area of the slipper pad, r_{pp} , and the diameter of the capillary tube, d_c . r_{pp} is defined as:

$$r_{pp} = \frac{L_{W_{pocket}} L_{H_{pocket}}}{A_p} \quad (4.53)$$

Furthermore the ratio between the length and the width of the pocket area, r_{WH} , is applied such that.

$$L_{W_{pocket}} = r_{WH} L_{H_{pocket}} \quad (4.54)$$

By substitution of Equation 4.54 into 4.53 and by solving for $L_{H_{pocket}}$ Equation 4.55 occurs.

$$L_{H_{pocket}} = \sqrt{\frac{r_{pp} A_p}{r_{WH}}} \quad (4.55)$$

4. Friction and Leakage Analysis

The outside length of the slipper pad can be calculated by applying Equation 4.54 and 4.55.

$$\begin{aligned} L_W &= L_{W_{pocket}} + 2w_{BR} \\ &= \sqrt{\frac{r_{pp}A_p}{r_{WH}}} r_{WH} + 2w_{BR} \end{aligned} \quad (4.56)$$

By substituting Equation 4.51, 4.52, 4.54, 4.55, and 4.56 into Equation 4.50 and then differentiate with respect to the fluid film height, h_{land} , an expression of the optimal fluid film height can be derived. The leakage and frictional parts of the power loss are differentiated separately, starting with the leakage power loss.

$$\begin{aligned} \frac{d}{dh} Q_{leaksp} (P_C - P_{atm}) &= \frac{d}{dh} \left(\frac{(L_H - w_{BR})h_{land}^3 (P_{BP} - P_{atm})}{6\mu w_{BR}} \right. \\ &\quad \left. + \frac{(L_W - w_{BR})h_{land}^3 (P_{BP} - P_{atm})}{6\mu w_{BR}} \right) (P_C - P_{atm}) \\ &= \frac{h_{land}^2 (P_{BP} - P_{atm}) \left(2w_{BR} + \sqrt{\frac{r_{pp}A_p}{r_{WH}}} (r_{WH} + 1) \right) (P_C - P_{atm})}{2\mu w_{BR}} \end{aligned} \quad (4.57)$$

Next the frictional loss is differentiated with respect to h_{land} :

$$\begin{aligned} \frac{d}{dh} F_{fricsp} v_{surf} &= \frac{d}{dh} \frac{v_{surf}^2 \mu}{h_{land}} (L_W L_H - (L_{H_{pocket}} L_{W_{pocket}})) \\ &= \frac{-v_{surf}^2 \mu}{h_{land}^2} \left(2w_{BR} \left(2w_{BR} + \sqrt{\frac{r_{pp}A_p}{r_{WH}}} (r_{WH} + 1) \right) \right) \end{aligned} \quad (4.58)$$

Then by combining Equation 4.57 and 4.58, equating by zero, solve for h_{land} , and then choose the real positive solution, Equation 4.59 is obtained.

$$h_{land_{opt}} = \frac{\sqrt{2\sqrt{(P_{cyl} - P_{atm})(P_{BP} - P_{atm})} w_{BR} \mu v_{surf}}}{\sqrt{(P_{cyl} - P_{atm})(P_{BP} - P_{atm})}} \quad (4.59)$$

The optimum fluid film height is now obtained, and the ratio between the frictional loss and the leakage loss can be evaluated. $h_{land_{opt}}$ is inserted as h_{land} and after some simplifications the ratio can be found to be:

$$\frac{\mathcal{P}_{fric}}{\mathcal{P}_{leak}} = \frac{\frac{-v_{surf}^2 \mu}{h_{land_{opt}}^2} \left(2w_{BR} \left(2w_{BR} + \sqrt{\frac{r_{pp}A_p}{r_{WH}}} (r_{WH} + 1) \right) \right)}{\frac{h_{land_{opt}}^2 (P_{BP} - P_{atm}) \left(2w_{BR} + \sqrt{\frac{r_{pp}A_p}{r_{WH}}} (r_{WH} + 1) \right) (P_{cyl} - P_{atm})}{2\mu w_{BR}}} = 3 \quad (4.60)$$

To calculate $h_{land_{opt}}$ the pressure inside of the pocket, P_{BP} , is needed. In order to calculate the

required pressure in the pocket to satisfy the force equilibrium, steady-state conditions has to be assumed, i.e. $\dot{h} = 0$ and h is an arbitrary height. This is due to the fact that F_{lands} is independent on h_{land} , and can be calculated as a linear pressure drop across the land. This is illustrated by returning to Equation 4.16 for the dimensionless pressure $P(X, T)$, with flooded boundary conditions.

$$P(X, T) = \frac{v_{surf}^* (\phi_c H + \sigma^* \phi_s) (X + 1)}{\phi_x H^3} + \frac{\beta \dot{H} \phi_c (\frac{1}{2} X^2 + X + \frac{1}{2})}{\phi_x H^3} + \left(\frac{1}{2} P_2 - \frac{1}{2} P_1 - v_{surf}^* \frac{(\phi_c H + \sigma^* \phi_s)}{\phi_x H^3} - \beta \dot{H} (X + 1) \right) + P_1 \quad (4.61)$$

where: $v_{surf}^* = \frac{v_{surf}}{d\phi}$

Recall that P_1 and P_2 are dimensionless pressures of P_{BP} and P_{atm} respectively.

If the dimensionless squeeze film $\dot{H} = 0$, and $P(X, T)$ is integrated across the slit, from $X = -1$ to $X = 1$, the dimensionless pressure distribution is equal to:

$$\int_{-1}^1 P(X, T) = \left(\frac{1}{2} P_2 + \frac{1}{2} P_1 \right) \quad (4.62)$$

Notice that, under the given conditions, the pressure distribution is linear and independent of H . From this the steady-state land force, $F_{lands-ss}$, can be written as Equation 4.63.

$$\begin{aligned} F_{lands-ss} &= A_{land} P_{lands} \\ &= (L_W L_H - L_{W_{pocket}} L_{H_{pocket}}) \frac{1}{2} (P_{BP} + P_{atm}) \\ F_{lands-ss} &= w_{BR} \left(\sqrt{\frac{r_{PP} A_P}{r_{WH}}} (r_{WH} + 1) + 2w_{BR} \right) (P_{BP} + P_{atm}) \end{aligned} \quad (4.63)$$

where: A_{land} Total area of the lands

P_{lands} Dimension form of $P(X, T)$

The force equilibrium also consists of F_{BP} and F_{cyl} which are defined as:

$$F_{cyl} = A_p r_{cyl}^2 \pi \quad (4.64)$$

$$F_{BP} = P_{BP} (L_{W_{pocket}} L_{H_{pocket}}) \quad (4.65)$$

These are inserted into Equation 4.66, and by solving for P_{BP} Equation 4.67 is obtained.

$$0 = F_{lands-SS} + F_{BP} - F_{cyl} \quad (4.66)$$

$$P_{BP} = - \frac{\left(\sqrt{\frac{r_{pp}A_p}{r_{WH}}} (r_{WH} + 1) + 2w_{BR} \right) w_{BR} P_{atm} - P_{cyl} A_p}{\left(\sqrt{\frac{r_{pp}A_p}{r_{WH}}} (r_{WH} + 1) + 2w_{BR} \right) w_{BR} + r_{pp} A_p} \quad (4.67)$$

Equation 4.67 as a function of r_{pp} is applied in the optimisation procedure, as an expression for the pocket pressure.

Recall that the objective is to minimise the power loss, as a function of r_{pp} and d_c . This function is the objective function, and the constraints which needs to be satisfied are $h_{land} = h_{land_{opt}}$ and $Q_{Cap}, Q_{leak_{sp}} > 0$. Thus the optimisation problem is stated as:

$$\begin{aligned} \text{Objective function} & : \text{minimise}(\mathcal{P}_{SP}) \\ \text{Non-linear constraint} & : Q_{leak_{sp}} > 0, Q_{Cap} > 0, h_{land} = h_{land_{opt}} \\ \text{Bounds of } r_{pp} & : [r_{pp_{min}}; r_{pp}; r_{pp_{max}}] \\ \text{Bounds of } d_c & : [d_{c_{min}}; d_c; d_{c_{max}}] \end{aligned}$$

The lower bound of r_{pp} is found by applying the expression for h_{land} as a function of r_{pp} and equating with zero and solving for r_{pp} such that:

$$r_{pp_{min}} = 0.7486228495$$

h_{land} is very sensitive to r_{pp} as shown on Figure 4.3.10, thus high accuracy of the minimum bound is needed. Since the height of the fluid film is so sensitive to r_{pp} at a specific pressure, P_C , it is necessary to consider carefully what area ratio is required in order to stay within the desired limits of the fluid film height. Also considerations have to be given to the variations of the pressures in the system as the profile of the height h_{land} as a function of r_{pp} is sensitive to the supply pressure as illustrated on Figure 4.3.10. The upper bound is set to $r_{pp_{max}} = 1$, as that is the maximum desired size of the slipper pad. When the surface area of the slipper pad pocket increases, so does the diameter of the eccentric shaft as seven slipper pads are in contact with it.

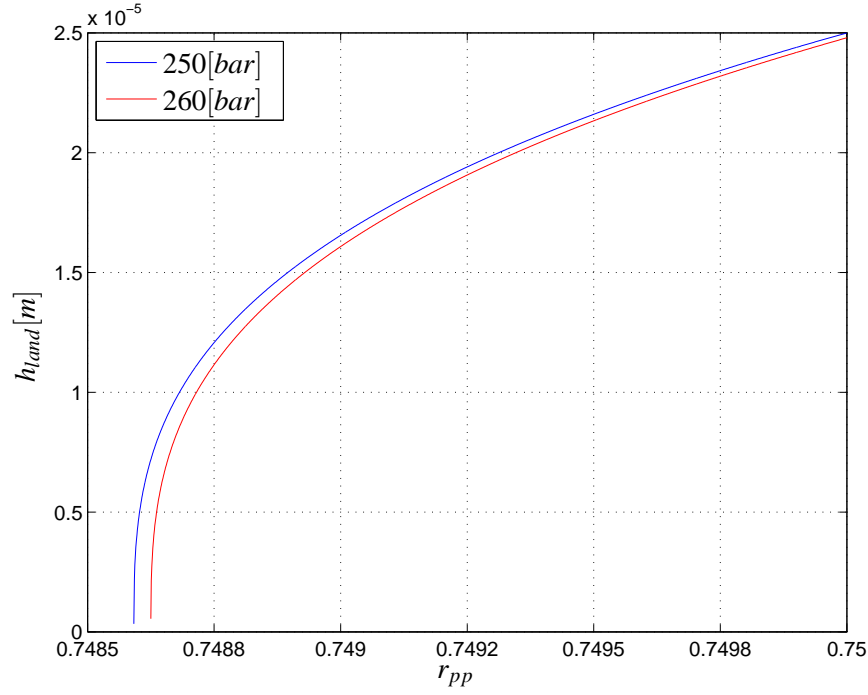


Figure 4.3.10: h_{land} as a function of r_{pp} . Notice the very small increments of r_{pp} .

l_c is defined as the distance from the upper surface of the piston to the surface of the bearing pocket. The stroke length of the piston is $0.58[m]$ thus minimum length of the piston rod is set to $0.6[m]$. The lower bounds of d_c is chosen on the basis of an evaluation of the minimum producible diameter in an $0.6[m]$ long straight tube. $1[mm]$ is chosen as $d_{c_{min}}$ and the upper limit is chosen as $d_{c_{max}} = 20[mm]$.

When the piston rod length, l_c , is considered, the length, l , also has to be considered. Recall that l is the distance from the center of the eccentric shaft to the piston, cf. Figure 4.3.11. However, to define l the radius of the eccentric shaft, r_{ecc} , is needed. The requirements to the minimum radius of the eccentric shaft is set by the size of the slipper pads. Each eccentric shaft is connected to seven pistons, consequently the circumference of one eccentric shaft is required to have room for seven slipper pads. r_{ecc} can be defined from the clearance, C , and $L_H = \sqrt{\frac{r_{pp}A_p}{r_{WH}}} + 2w_{BR}$, cf. Equation 4.55 and Figure 4.3.2:

$$r_{ecc} = \frac{\left(\sqrt{\frac{r_{pp}A_p}{r_{WH}}} + 2w_{BR} + C \right) 7}{2\pi} \quad (4.68)$$

where: C Clearance between the slipper pads, cf. Figure 4.3.11.

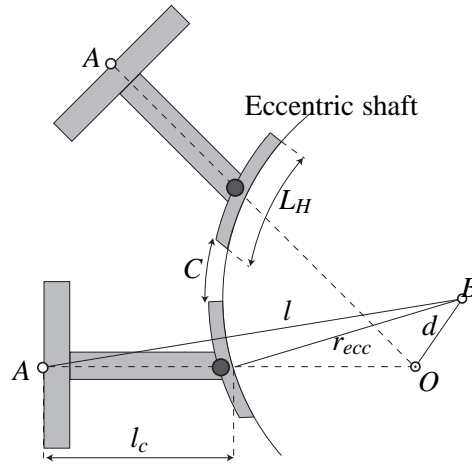


Figure 4.3.11: Lengths and notation for explanation of the clearance C .

This means that after a choice of r_{pp} , r_{WH} , and w_{BR} , r_{ecc} is set according to Equation 4.68. From r_{ecc} , the length l is calculated as:

$$l = r_{ecc} + l_c \quad (4.69)$$

From this it is clear that by altering the slipper pad size, the size of the pump is also altered.

Returning to the optimisation procedure, a working point has to be chosen. This working point is chosen at a point in the cycle where $P_C = 250[\text{bar}]$ and the parameters are taken at a point where the velocity is approximately the average velocity, $v_{surf} = 0.5$, cf. Figure 4.3.8. From Table 4.3.1 it is noticed that l is now $1.165[\text{m}]$, which is significantly different from the l applied in the design sections where $l = 0.7[\text{m}]$.

Parameters	Value	Unit
v_{surf}	0.5	$[\text{m/s}]$
l_c	0.6	$[\text{m}]$
w_{BR}	$50 \cdot 10^{-3}$	$[\text{m}]$
r_{WH}	1.313	—
A_p	0.1590	$[\text{m}^2]$
μ	0.04186	$[\text{m}^2 \cdot \text{s}^{-1}]$
l	1.165	$[\text{m}]$
P_C	250	$[\text{bar}]$

Table 4.3.1: Parameters obtained at the working point

By applying the MATLAB optimisation function, *fmincon*, the minimum of the constrained objective function in the chosen working point is calculated to:

$$\mathcal{P}_{SP} = 103.6[\text{W}] \quad (4.70)$$

This yields an area ratio and capillary tube diameter of:

$$r_{pp} = 0.7486508750 \quad (4.71)$$

$$d_c = 0.0050[m] \quad (4.72)$$

4.3.3 Calculation Problem

After the implementation of the dynamic friction model of a slipper pad bearing as described in section 4.2.2, a problem occurred which will be explained here.

In the previous section, it was concluded that in steady state, the force from the lands, F_{lands} , is independent on h , cf. Equation 4.63, if $\dot{h}_{land} = 0$. However, when the states of the system changes, e.g. the surface velocity or the cylinder pressure, the assumption of $\dot{h}_{land} = 0$ is not valid. Thus unless r_{pp} matches perfectly with the parameters of that exact working point, the force equilibrium will not be satisfied. This means that unless an \dot{h}_{land} is present in the equation for the pressure distribution under the lands, the force equilibrium can not be satisfied which is illustrated in Figure 4.3.12. This is due to the fact that this is the only way that the numerical method can increase or reduce F_{lands} .

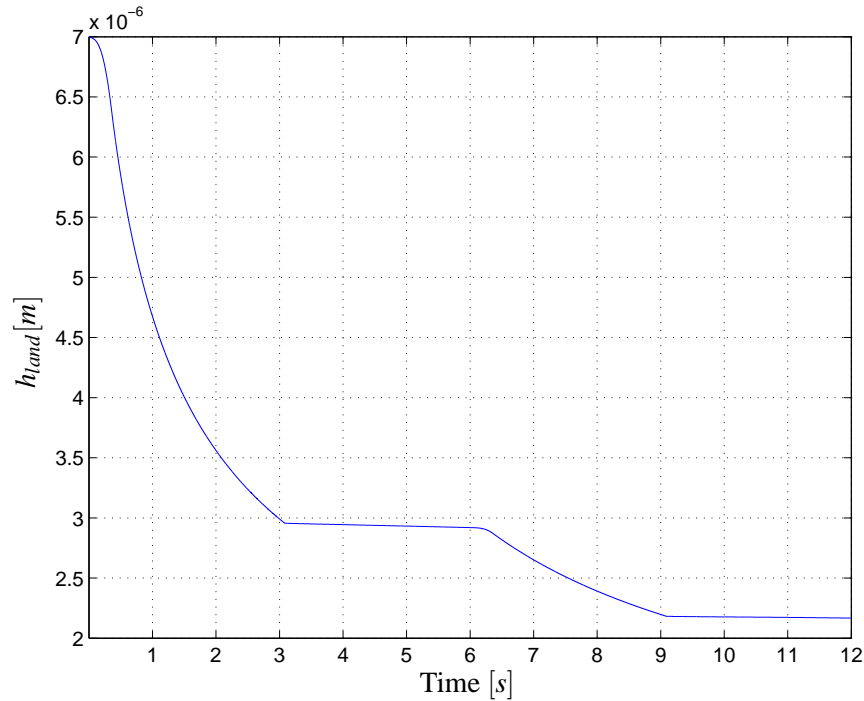


Figure 4.3.12: h_{land} for the dynamic model as a function of time. This shows the result of the required \dot{h}_{land} which in this case has to be negative.

This summarizes to the fact that unless r_{pp} can be tuned to match all operation points perfectly, the slipper pad will not reach any steady state value, but increase or decrease h_{land} . If a negative \dot{h}_{land}

4. Friction and Leakage Analysis

is necessary to satisfy the force equilibrium, the film height will decrease until it is within asperity contacts, and F_{asp} will then fulfil the force equilibrium. If a positive \dot{h} is present, the fluid film height will increase indefinitely. It can only do so, due to the chosen method applied to calculate the pressure in the pocket, which assumes that flow in and out of the cylinder are equal, and the chosen method to calculate F_{lands} .

From the above it can be concluded that the slipper pad cannot be modelled as described in this project. Three methods which might solve this problem are presented:

- **Tilting.** By tilting the slipper pad, the pressure under the lands are able to produce a higher or lower pressure due to the restriction or expansion through the slit, cf. Figure 4.3.13a. In this way the total force from the lands can be higher or lower compared to the current model depending on the situation. This method has been adopted by several sources [Cunningham and McGillavary, 1965], [Koç and Hooke, 1996]. At the time of this conclusion, this method is considered too advanced to be implemented in the model, due to the time frame of the project.
- **Non-flatness.** By producing a non-flat surface of the lands, the pressure through the slit will change as h is no longer constant with x , cf. Figure 4.3.13b. This is not implemented either due to the same reasons as stated for the above method.
- **Steady-state calculation.** The frictional force and leakage can be modelled by applying a steady state assumption. This removes all the dynamic behaviour and simplifies the system. This method is implemented in the subsequent section.

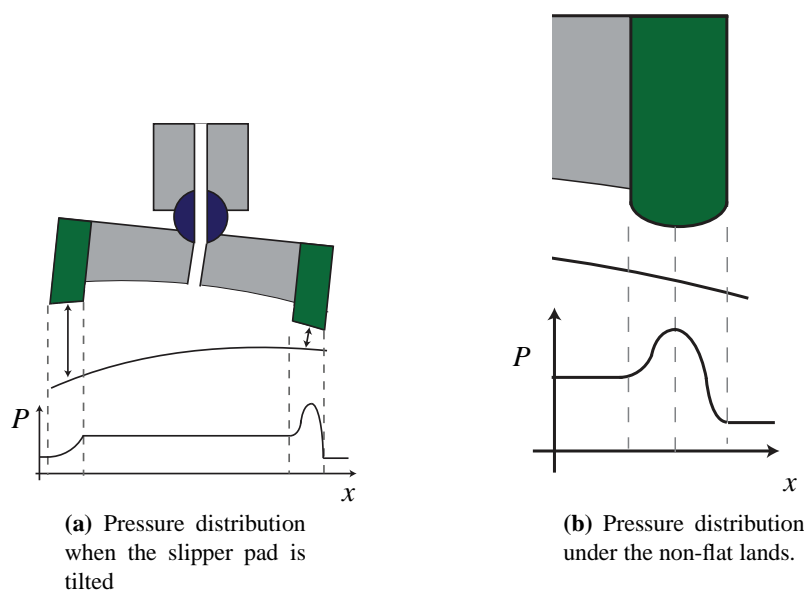


Figure 4.3.13: Slipper pad bearing. Note that the dimensions are exaggerated for purpose of clarity.

4.3.4 Steady-State Model

The steady-state model is produced based on the assumption that with $\dot{h}_{land} = 0$, a sufficiently accurate model can be generated. This is believed to be the case as the pressure in the cylinder chamber is close to constant in a large part of the cycle as it is either $P_C \approx 10[bar]$ or $P_C \approx 250[bar]$. Based on this the assumption is deemed valid and the steady-state model is a sufficiently accurate model of the slipper pad friction and leakage.

4.3.5 Steady-State Model

Q_{Cap} and $Q_{leak_{sp}}$ can be written as stated in Equation 4.73.

$$\begin{aligned} Q_{Cap} &= k_1(P_C - P_{BP}) \\ Q_{leak_{sp}} &= k_2(P_{BP} - P_{atm})h_{land}^3 \end{aligned} \quad (4.73)$$

where: $k_1 = \frac{d_c^4 \pi}{128 l_c \mu}$

$$k_2 = \frac{(L_H - w_{BR})}{6 \mu w_{BR}} + \frac{(L_W - w_{BR})}{6 \mu w_{BR}}$$

When applying that $Q_{Cap} = Q_{leak_{sp}}$ Equation 4.74 can be obtained.

$$\begin{aligned} k_1(P_C - P_{BP}) &= k_2(P_{BP} - P_{atm})h_{land}^3 \\ h_{land} &= \sqrt[3]{\frac{k_1(P_C - P_{BP})}{k_2(P_{BP} - P_{atm})}} \end{aligned} \quad (4.74)$$

The steady state model is based on the assumption that $\dot{h}_{land} = 0$ and fully flooded conditions under the lands. Due to this the expression for the pressure in the slipper pad pocket in Equation 4.67 can be applied. By substituting this for P_{BP} in Equation 4.74 and choosing the positive real solution, h_{land} becomes a function of only P_C as P_{atm} is a constant. Thus for every value of P_C one specific fluid film height, h_{land} , exists. Based on this the leakage and friction can be found by the use of Equation 4.51 and 4.47 respectively.

4.4 Friction and Leakage Results

This section describes the friction and leakage of the piston ring and slipper pad bearing, obtained from the models derived in this chapter. The parameters applied in the simulation are given in Table 4.4.1.

Nomenclature	Parameter	Value	Unit
Viscosity	μ	0.04186	$[Pa \cdot s]$
Friction coefficient	c_f	0.3	$[-]$
Surface roughness	σ	0.35	$[\mu m]$
Poisson's ratio of material 1 and 2	ν_1, ν_2	0.3	$[-]$
Young's moduli of material 1 and 2	E_1, E_2	200	$[GPa]$
Clearances between slipper pads	C	0.05	$[m]$
Size of pocket area	A_{pocket}	0.119	$[m^2]$
Height of piston ring	L_{PR_x}	5	$[mm]$
Length of piston ring	L_{PR_y}	8.75	$[mm]$
Maximum squeeze film	\dot{h}_{lim}	$1 \cdot 10^{-2}$	$\left[\frac{m}{s}\right]$
Converge criteria	C_{con}	200	$[N]$

Table 4.4.1: Parameters for calculation of the friction and leakage of the piston ring and the slipper pad bearing. σ , c_f , ν and E are extracted from [Akalin and Newaz, 2001]

The dimensions of the piston ring are an initial design set, but since the friction force is directly proportional to L_{PR_x} , cf. Equation 4.36, this analysis is not sensitive of this guess. Likewise the leakage is inversely proportional to L_{PR_x} and will decrease accordingly if the ring was to increase in height.

4.4.1 Piston Ring

During calculation of the fluid film height between the piston ring and the cylinder wall a problem which concerns the numerical method applied arises: At the time when decompression starts, the force equilibrium of the piston ring is solved by the numerical method by setting a high \dot{h} , which causes h to increase at a high rate. Depending on the sampling time, T_s , and the calculated \dot{h} , h will overshoot the correct film height. This is illustrated in Figure 4.4.1a. Notice the decrease in overshoot when the sampling time changes. Due to high simulation time, the sampling time is not decreased further below $T_s = 1 \cdot 10^{-6}[s]$. Instead a maximum and minimum \dot{h} , denoted \dot{h}_{lim} , is applied, such that the film height overshoots only a small amount, and then approaches the correct film height.

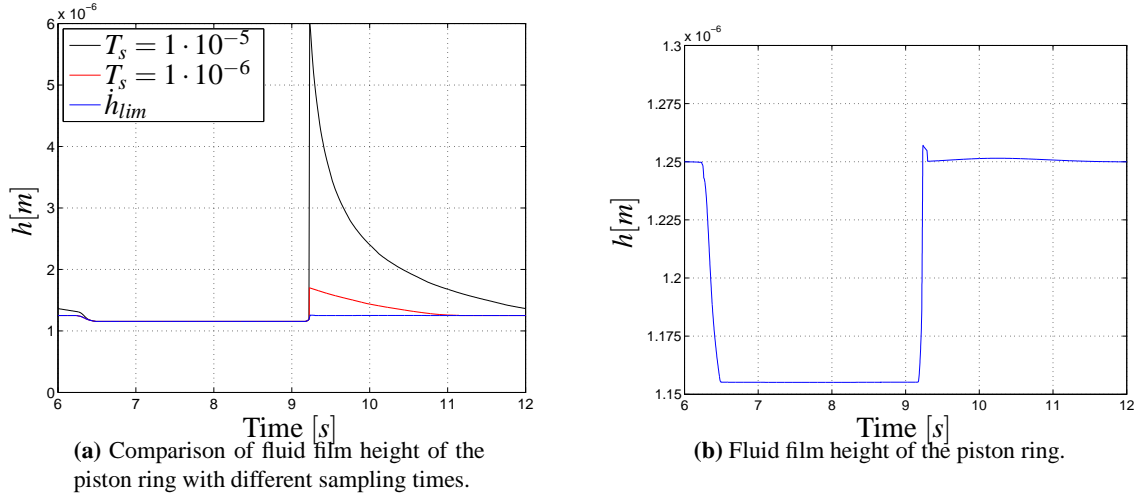


Figure 4.4.1: Fluid film height between cylinder wall and piston ring.

The corrected fluid film height in Figure 4.4.1b follows the cylinder pressure as intended: Low film height with high cylinder pressure and higher film height with low cylinder pressure. The friction and leakage are illustrated in Figure 4.4.2 and 4.4.3 respectively. From these Figures it can be concluded that the leakage power loss is negligible compared to the frictional power loss. This is due to the fact that the piston rings are in asperity contact at all times as $h < \Omega \cdot \sigma = 1.4[\mu\text{m}]$. The high negative friction force at $t = 9[\text{s}]$ is caused by the cylinder pressure, which has not yet decreased from 250[bar] to 10[bar]. This results in a low film height and a high negative frictional force which drops to $-800[\text{N}]$ when the cylinder pressure has decreased to 10[bar] and the film height has increased to $1.25[\mu\text{m}]$.

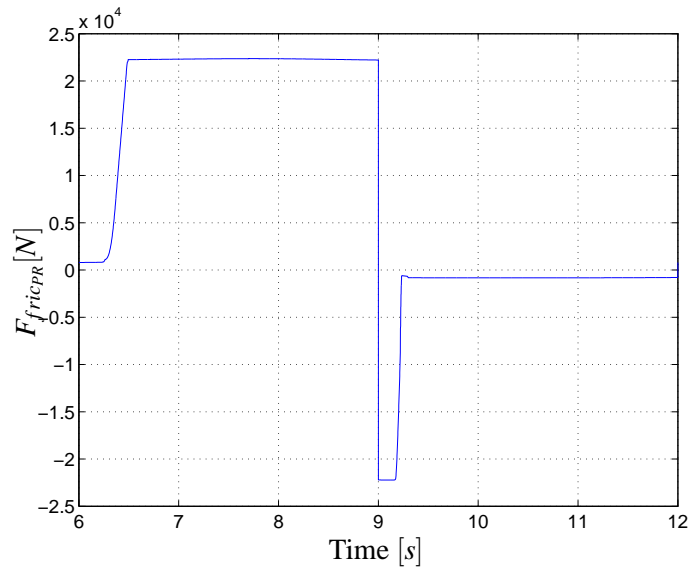


Figure 4.4.2: Friction force between cylinder wall and piston ring.

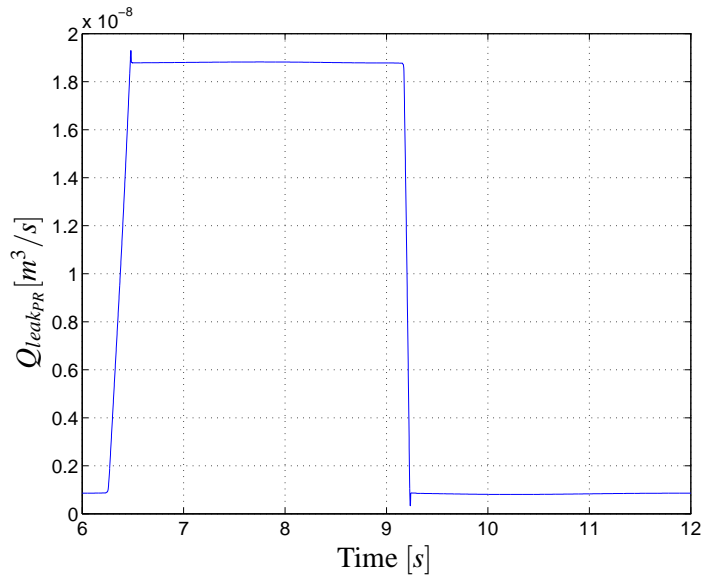


Figure 4.4.3: Leakage flow between cylinder wall and piston ring.

4.4.2 Slipper Pad

The film height of the slipper pad is illustrated in Figure 4.4.4. The film height at 250[bar] is $\approx 9[\mu m]$, which is close to the optimum film height, 9.2[μm]. Notice that the height follows the cylinder pressure as stated in section 4.3.5.

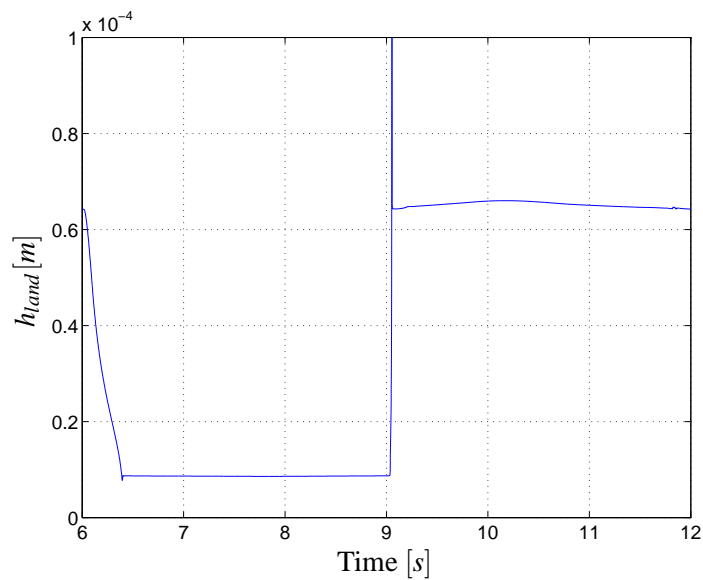


Figure 4.4.4: Fluid film height of the slipper pad.

The friction force and the leakage of one slipper pad bearing is illustrated in Figure 4.4.5 and 4.4.6 respectively. Contrary to the piston ring, the friction is negligible and the leakage now has a significant value. The summed leakage flow of all the cylinders is plotted in Figure 4.4.7.

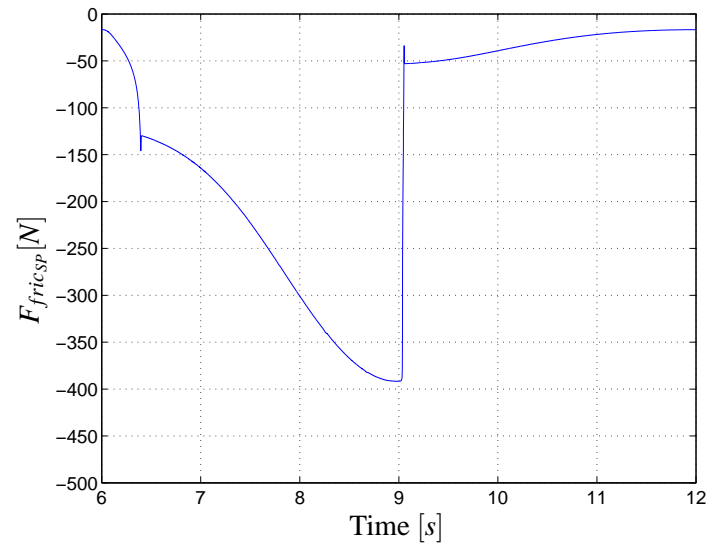


Figure 4.4.5: Friction between the eccentric shaft and the slipper pad.

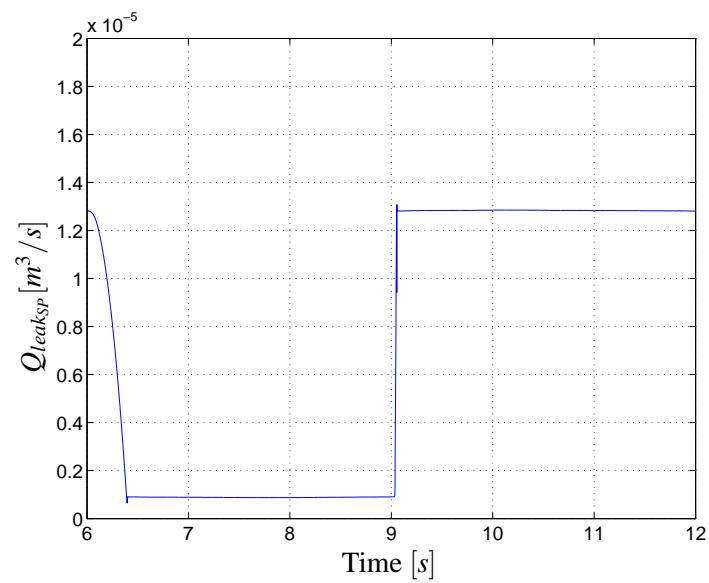


Figure 4.4.6: Leakage flow of one slipper pad.

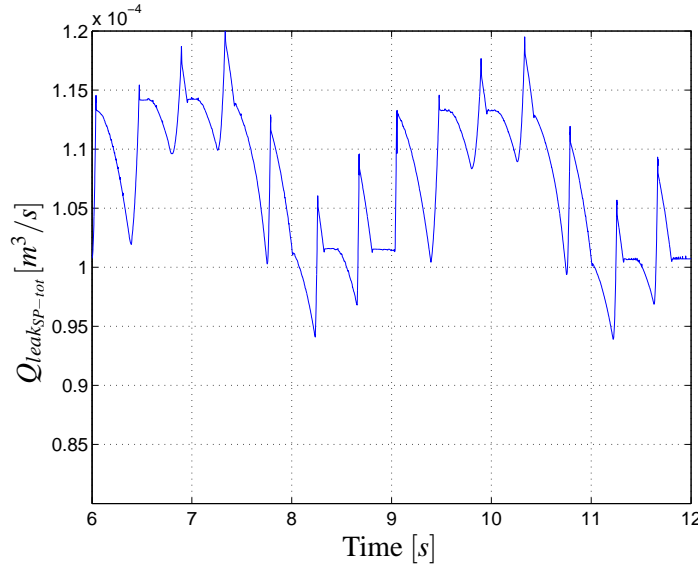


Figure 4.4.7: Total leakage flow of the slipper pad.

The total efficiency η_{tot} can now be evaluated by the same method as the one applied to calculate the hydraulic efficiency in section 2.3.2. By using the hydraulic efficiency the efficiency of the piston ring and the slipper pad can also be calculated.

$$\begin{aligned}\eta_{tot} &= 0.98937 \\ \eta_{PR-SP} &= \frac{\eta_{tot}}{\eta_{hyd}} = 0.99731\end{aligned}$$

The calculated efficiency has to be considered as a guideline for the power loss in the piston ring assembly and the slipper pad, since they are not verified with experimental results. Furthermore only one piston ring is inserted, and several articles suggest the use of three rings [Livanos and Kyrtatos, 2007] [Hu and Cheng, 1994]. However, these articles concerns ICE where the consequences of leakage flow are different than for an hydraulic system, therefore three rings are not necessarily the optimum number in this application. The implementation of more rings may introduce higher frictional losses, but this problem is complex since the pressure distribution through the gap between the cylinder wall and the piston, changes when more rings are inserted.

The frictional and leakage loss of the journal bearing between the piston rod and the slipper pad is not considered in this project. Neither is the bearings which fixates the central shaft connected to the rotor, and the casing of the pump.

Recall that h_{land} is sensitive to the area ratio, r_{pp} at a specific pressure, P_C , as presented in Figure 4.3.10. This means that it is important to consider what area ratio is chosen as it might be difficult to maintain the exact pressure at which it was chosen. This is due to the fact that the height changes rapidly at small variations in r_{pp} . Also the profile of h_{land} as a function of r_{pp} changes depending on the pressure so that with a slightly larger operating pressure the slipper pad might reach $h_{land} = 0$ instead of the intended height. This means that when the slipper pad is designed,

a safety margin has to be carefully considered such that the slipper pad does not reach $h_{land} = 0$ due to high pressure or unsatisfactory tolerances. Also it is important that r_{pp} is not too large since it will cause the leakage to increase rapidly due to the h_{land}^3 -correlation between fluid film height and leakage flow, cf. Equation 4.73.

4.5 Summary

The preceding analysis showed several areas of interest when the friction and leakage in the radial piston pump are considered.

- By implementation of a piston ring in a radial piston pump the leakage can be lowered to a minimum. However, the friction dominates the power loss of the piston ring assembly, due to low film height. Some compromise between friction and leakage exist, and this can be examined further to reduce the total power loss of the piston ring assembly.
- The piston ring friction model applied in this project model only introduces a single piston ring. The model can be expanded to include more rings and thus change the pressure distribution between the cylinder wall and the piston skirt and rings. This can produce a higher film height for each ring, but can also increase the friction due to the larger surface area in contact with the cylinder wall. Consequently some optimum number of rings exists.
- Choice of working point for optimisation. The working point chosen for the optimisation procedure also affects the results of the optimisation procedure, and it only represents a short period of the cycle. An analysis of the best working point for the optimisation procedure will produce a better overall efficiency.
- The derivation of the slipper pad friction model resulted in a correlation between the size of the slipper pad and the size of the pump. By increasing the slipper pad surface area, the diameter of the eccentric shaft increases.
- The dynamic model applied for the piston ring film height, can not be applied for calculation of the film height of the slipper pad, unless the slipper pad can be allowed to reach asperities. The reason for this may be that the method to calculate the film height, needs non-parallel surfaces to reach a steady state. This might be solved by the introduction of tilt or non-parallel surface to the slipper pad bearing, e.g. fillet corners.
- The steady state model produces the frictional and leakage loss of the slipper pad, from the assumption that the film height only depends on the cylinder pressure. The film height of the slipper pad decreases with a higher cylinder pressure, which is consistent with a result from a similar analysis performed on a radial piston motor [Cunningham and McGillavary, 1965].

Conclusion 5

This master thesis was initiated by an examination of hydraulic transmission in a 5[MW] offshore wind turbine. PMC Servi Cylinderservice A/S has designed a radial piston pump for this application with 14 cylinders distributed on two eccentric shafts producing a flow of 12500[l/min] at a working pressure of 250[bar]. PMC servi declares that a total efficiency of 0.96 is reachable by the use of standard NG40 valves as in- and outlet valves. The initiating problem was to examine the problems regarding to opening and closing these valves.

In order to examine this, a mechanical model which describes the movement of the piston was produced. The model is connected to the rotor of the wind turbine by use of an acceleration and velocity controller. The controller is tuned in such a way that it ensures a constant angular velocity of the wind turbine, and that the pump has infinite torque available.

Along with the mechanical model an early version of the hydraulic model was set-up such that the opening of the valves could be examined. Five standard valves from Parker ranging from NG40 to NG100 was inserted as in- and outlet valves of the cylinders. These was modelled with a discharge coefficient of 0.8 and an opening area found based on the assumption that they were sharp-edged. The efficiency of the NG40 valve was calculated to 0.9525 and for the NG63 valve it was found to be 0.9897. The efficiency of the NG40 valve was based on an optimistic calculation and was found to be below the declared efficiency by PMC Servi, thus it is concluded that the radial piston pump cannot produce that efficiency. Therefore the larger NG63 valve was selected as a better choice, due to the significant improvement compared to the NG40 valve.

The hydraulic and mechanical model resulted in a problem specification with the goal of analysing the efficiency of the PMC Servi pump and suggesting modifications for improvement.

Based on the problem specification the power loss across the NG63 valve was examined by a CFD-analysis. This resulted in a variable discharge coefficient and was along with a more accurate modulation of the opening area, implemented in the non-linear model. This leads to a hydraulic efficiency of 0.975862. In order to improve this efficiency a deflector valve was designed, based on a Ph.d. project concerning flow force compensation in a poppet valve, and on computed CFD-calculations. A variable discharge coefficient and an opening area function was also derived for the deflector valve and implemented in the non-linear model which resulted in a total efficiency of 0.983127. A non-dimensional analysis showed that a downsized model of the deflector valve could not be produced and tested in the affiliated workshop, and thus the non-linear model was not verified experimentally. This means that the efficiency has to be evaluated as a guideline, since the CFD-model has to be verified with experimental results in order to make a solid conclusion regarding the efficiency. If the valve was tested, the valve design procedure can be iterated and tested until a satisfying result is obtained.

5. Conclusion

A variation of the mass of the poppet in the deflector valve, the volume between the cylinder and the valve, and the frictional constant, was conducted. This suggested that the bandwidth of the system has to be at an appropriate level such that higher order frequencies are not magnified. Furthermore, a variation of the spring stiffness and distortion of the spring in the deflector valve was varied and resulted in a set of parameters which, along with the optimum mass, frictional constant, and volume was inserted as parameters of the deflector valve. This leads to an improvement of the efficiency to 0.983288.

By insertion of two identical NG63 valves in the non-linear model with a parallel coupling the efficiency increased to 0.990029 and with the deflector the efficiency was 0.992038. From this it can be concluded that by installation of two valves, the efficiency is increased, and the number of valves should be considered if the pump is redesigned.

A friction and leakage model for the piston rings in a radial piston pump, was implemented. However, since no models concerning the rings in a hydraulic radial piston pump is available, literature concerning internal combustion engines, was applied instead. The chosen calculation method uses a concentric piston ring, which can deflect radially and thus creates equal film height all the way around the piston ring. The mixed lubrication model is based on an a non-linear approximation of a Gaussian distribution of asperities and was simplified by assuming constant density and viscosity. The result of the piston ring model was as desired: low film height during compression and higher film height during decompression. The results also showed that the fictional loss was significantly higher than the leakage loss, and the leakage could be considered negligible.

A dynamic model based on the same method as applied at the piston rings, was used to calculate the frictional and leakage loss at the slipper pad bearing, i.e. the hydrostatic lubricated bearing between the eccentric shaft and the piston rod. However, it was concluded that this model cannot be applied to calculate the lubrication film height between the slipper pad and the eccentric shaft. Instead of the dynamic model, a steady-state model was produced by assuming that the squeeze film is zero. This resulted in the film height being a function of only the cylinder pressure.

In order to dimension the slipper pad, an optimisation function which minimised the power loss due to leakage and friction was produced. The ratio between the friction loss and the leakage loss is found to be equal to three at the optimum film height. The optimisation function sets the diameter of the supply tube to the bearing pocket and the surface area of the pocket area, such that the film height is equal to the optimum height in the working point. The optimisation also showed that the film height is sensitive to size of this area, and that the solution lacks robustness. To solve this, a more thorough analysis of the working point is necessary. The optimum area ratio between the piston area and the pocket area is 0.7486508750 and the diameter of the tube is 5[mm] at a supply pressure of 250[bar]. The result of the steady-state model showed significant leakage loss and low frictional loss contrary to the piston ring model. The results also showed that the film height decreased with increased cylinder pressure which is consistent with the results of a similar

analysis of a bearing in a radial piston motor [Cunningham and McGillavary, 1965].

The two friction and leakage models was implemented in the non-linear model and produced a total efficiency of 0.98937. This value is to be considered as a guiding value since no experimental verification of any kind has been performed on the essential parts of the complete model. The significantly high efficiency may be a product of some of the limitations made in this project. E.g. the journal bearings in the piston rod and the bearings which fixates the central shaft connected to the rotor, has not been modelled.

Under the assumption that the parameters applied in the models are satisfactory near the actual values, the efficiency $\eta_{tot} = 0.98937$ confirms that the design proposed by PMC Servi, with the modifications stated in this project, yields a competitive pump for application in a hydraulic wind turbine.

Future Perspectives

If this project was to be expanded some areas of interest are elaborated here.

The non-linear model can be linearised in order to examine if the valves has to have a specific bandwidth, as suggested by the parameter variations. To do so the full transfer function should be outlined including a continuity equation for each of the 14 chambers, and a orifice equation for each of the 28 valves.

As mentioned in the conclusion, the CFD-analysis is not supported by experimental results, which could be performed such that the variable discharge coefficient can be verified. Likewise all the parameters of the non-linear model, eg. bulk modulus, temperature, frictional constant, and pressure losses should be verified by experiments.

Expansion of the slipper pad model by introducing tilt, this might solve the problem stated in the conclusion regarding the dynamic model for calculation of the film height.

The optimum profile and size of piston rings should be examined and likewise the effect of increasing the no. of rings.

Only two major mechanical losses remains in the pump; the journal bearing between the piston rod and slipper pad, and the bearings fixating the central shaft. These should be examined further such that the mechanical efficiency of the pump is examined thoroughly.

Some of the design parameters of the model are set from an initial guess. The correlation between these and the efficiency can be examined by a parameter variation, e.g. the length of the piston rod, the size of the eccentric, the land area of the slipper pad etc.

A long term perspective is to produce a full-scale prototype of the radial piston pump, such that the hydraulic transmission can be tested.

As it appears from the above, there are still many interesting subjects to be investigated, if further development of the pump is desired. However, the most essential aspect is to get an experimental verification of the various models and parameters, in order to continue the development of the pump with the model constructed in this project.

5. Conclusion

Summary 6

The content of this report is a master thesis in Electro-Mechanical System Design (EMSD) at Aalborg University. The title is 'Efficiency of a Radial Piston Pump Applied in a 5MW Wind Turbine with Hydraulic Transmission'. The project spanned from September 1st 2010 to May 31st 2011 and is addressed towards readers with a basic knowledge of mechanical- and hydraulic modelling.

PMC-Servi has proposed a radial piston pump with 14 cylinders to be applied in a 5[MW] wind turbine with an alleged efficiency of 0.96. This efficiency is the foundation of this project where this claim is tested by the use of a non-linear model and computational fluid dynamics. The pump produces a flow of 12.500[l/min] at a working pressure of 250[bar].

In order to examine this, a mechanical model was constructed along with a hydraulic model. Then the claim that regular NG40 valves is sufficient for the pump was tested along with 4 other standard valves ranging up to the size of NG100. All of these valves was inserted as both in- and outlet valves and tested to find the efficiency. The efficiency with the NG40 valve applied was found to 0.9525. As it is an optimistic calculation it is already clear that the pump can not satisfy the claim for an efficiency of 0.96 and an NG63 valve is thus chosen for the subsequent parts of the project. Based on the analysis of the valves and the constructed model, a problem specification with the goal of determining the efficiency of the PMC Servi pump and suggest alterations to improve this, was established.

Based on the problem specification a CFD-analysis was conducted of the NG63 valve in order to determine a variable discharge coefficient and a more accurate area function of the valve. This was then inserted into the model and compared to a similar analysis conducted on a special designed deflector valve. This valve was designed based on a Ph.d project and CFD calculations. A dimensional analysis also showed that a down-scaling of the valve, in order to be able to experimentally test it, was not possible. A variation of parameters was conducted in order to determine the values of the parameters associated with the design. All this resulted in an efficiency of the system of 0.983127 with the deflector valve inserted which was found to be 0.74 percentage points better than with the NG63 valve installed. Further analysis was done with several valves inserted which yielded an efficiency of 0.992038 for two deflector valve inserted.

A friction and leakage model was then constructed for the piston ring applied on each piston of the pump. This was done by utilising models derived for internal combustion engines. These applies a model of the mixed lubrication regime by conducting a non-linear approximation of a Gaussian distribution of asperities. This is then applied along with regular fluid dynamics in order to model

6. Summary

the friction and the leakage. The results yielded a significant friction and a negligible leakage for the single piston ring inserted.

Then a dynamic model of the fluid film height was constructed. This describes the slipper pad bearing applied between the eccentric shaft and the piston rod. The model was based on the same principle as the one utilised for the piston rings, however, the model emerged to be incapable of modelling the fluid film height due to an absence of non-linear behaviour of the pressure under the lands. This is believed to be due to the fact that no tilt was introduced of the slipper pad in the model. A steady state model was constructed instead based on the assumption that the squeeze film was zero. This resulted in an applicable model which yielded a significant leakage flow and negligible friction.

An optimisation procedure was then established in order to determine the dimensions of the slipper pad. This optimisation procedure yielded a ratio between the area of the piston and the area of the slipper pad pocket of 0.7486508750 and a diameter of the supply tube to the pocket of 5[mm].

With these models implemented and the parameters established through the parameter variation and the optimisation procedure the overall efficiency was found to 0.98937.

Bibliography

- Akalin, O. and Newaz, G. M. [2001], Piston ring-cylinder bore friction modeling in mixed lubrication regime: Part 1 - analytical results, *in* 'Journal of Tribology', Vol. 123, ASME, pp. 211–218.
- Andersen, T. O. and Hansen, M. R. [2003], *Fluid Power Systems - Modelling and Analysis*, 2. edn, Aalborg University, Aalborg.
- Andersen, T. O. and Hansen, M. R. [2004], *Fluid Power Circuits - System Design and Analysis*, 2. edn, Aalborg University, Aalborg.
- BWEA [2010], UK Offshore Wind: Staying on Track, Technical report, BWEA. <http://www.bwea.com/pdf/publications/CapReport.pdf>.
- Canbulut, F., Sinanoğlu, C. and Koč, E. [2009], 'Experimental analysis of frictional power loss of hydrostatic slipper bearings', *Industrial Lubrication and Tribology* **61**(3), 123–131.
- ChapDrive [2010], 'TECHNOLOGY'. [Cited 5. Okt 2010]
<http://www.chapdrive.com/technology/>.
- Cunningham, S. U. and McGillavary, D. [1965], The design and operation of hydrostatic slipper pad bearing in hydrostatic motors, *in* 'Proceedings part 3 - Institution of Mechanical Engineering', Vol. 180 - Part 3, pp. 81–101.
- Energistyrelsen [2009], Vindmøller i danmark, Technical report, Energistyrelsen. www.ens.dk.
- EURO AVIA COMPANY [2009], 'Europe will continue to lead global offshore wind', [Online]. [Cited 4. Okt 2010]
<http://energieaeoliana.wordpress.com/2009/12/04/europe-will-continue-to-lead-global-offshore-wind/>.
- EURO AVIA COMPANY [2010], 'Offshore wind heads for record year', [Online]. [Cited 4. Okt 2010]
<http://energieaeoliana.wordpress.com/2010/09/11/offshore-wind-heads-for-record-year/>.
- European Research Community On Flow, T. and Combustion [2000], *Best Practice Guide Lines*, 1. edn, Fluid Dynamics Laboratory.

BIBLIOGRAPHY

- Gohar, R. and Rahnejat, H. [2008], *Fundamentals of Tribology*, Imperial College Press. ISBN-13:978-1-84816-184-9.
- Hu, Y. and Cheng, H. S. [1994], Numerical simulation of piston ring in mixed lubrication - a nonaxisymmetrical analysis, in 'Journal of Lubrication Technology', Vol. 116, ASME, pp. 470–478.
- Ilsøy A. [2010], 'PMC Servi med 5 MW pumpekonsept for vindkraft', *FLUID SCANDINAVIA*.
- Jensen, K. K., Jessen, K., Runólfsson, G., Tychsen, T. and Mortensen, K. A. [2008], Pantograf kran - reguleringsteknisk analyse med forslag til stabilisering, Project, Institut for Energiteknik.
- Jonkman, J., Butterfield, S., Musial, W. and Scott, G. [2009], Definition of a 5-MW Reference Wind Turbine for Offshore System Development, Technical Report NREL/TP-500-38060, National Renewable Energy Laboratory, 1617 Cole Boulevard, Golden, Colorado 80401-3393. Prepared under Task No. WER5.3301.
- Klima- og Energiministeriet [2008], Energipolitisk aftale af 21. februar 2008, Technical report, Klima- og Energiministeriet. http://www.ve-net.eu/_root/media/29161_Energiaftale_21feb08_final%5B1%5D.pdf.
- Koč, E. and Hooke, C. J. [1996], Investigation into the effects of orifice size, offset and over-clamp ratio on the lubrication of slipper bearings, in 'Tribology International', Vol. 29, Elsevier Science Ltd., pp. 299–305.
- Koč, E. and Hooke, C. J. [1998], Considerations in the design of partially hydrostatic slipper bearings, in 'Tribology International', Vol. 30, Elsevier Science Ltd., pp. 815–823.
- Livanos, G. A. and Kyrtatos, N. P. [2007], Friction model of a marine diesel engine piston assembly, in 'Tribology International', Vol. 40, ELSEVIER, pp. 1441–1453.
- MHL Global Corporation Inc. [2008], Wind turbine with hydraulic transmission, Patent US 7,418,820 B2, United States Patent, Harvey et al. [Cited 6. Okt 2010] <http://www.freepatentsonline.com/7418820.pdf>.
- Muljadi, E., Pierce, K. and Migliore, P. [1998], Control Strategy for Variable-Speed, Stall-Regulated Wind Turbine, Technical Report NREL/CP-500-24311-UC Category: 1211, National Renewable Energy Laboratory, 1617 Cole Boulevard, Golden, Colorado 80401-3393. Work performed under task number WE803020.
- Patir, N. and Cheng, H. [1978], An average flow model for determining effects of three dimensional roughness on partial hydrodynamic lubrication, in 'Journal of Lubrication Technology', Vol. 100, ASME, pp. 220–230.
- Patir, N. and Cheng, H. [1979], Application of average flow model to lubrication between rough sliding surfaces, in 'Journal of Lubrication Technology', Vol. 101, ASME, pp. 220–230.

- Rohde, S. [1980], A mixed friction model for dynamically loaded contacts with application to piston ring lubrication, Technical report. Chicago.
- Sørensen, H. L. [1999], Fluidmekanisk Design af Hydrauliske Sædeventiler, PhD thesis, AAU.
- Szirtes, T. [2006], *Applied Dimensional Analysis and Modeling*, 2. edn, Butterworth-Heinemann. ISBN-13:978-0123706201.
- Tripp, J. A. G. J. H. [1971], The contact of two nominally flat rough surfaces, in 'Inst. Mech. Eng.', number 185, pp. 625–633.
- Versteeg, H. K. and Malalasekera, W. [2007], *An Introduction to Computational Fluid Dynamics - The Finite Volume Method*, 2. edn, Pearson Prentice Hall. ISBN-13: 978-0-13-127598-3.
- Watton, J. [2009], *Fundamentals Of Fluid Power Control*, 1. edn, Cambridge University Press. ISBN-13:978-0-521-76250-2.
- WindFacts [2010], 'Future trends for offshore wind'. [Cited 5. Okt 2010]
<http://www.wind-energy-the-facts.org/en/part-i-technology/chapter-5-offshore/wind-farm-design-offshore/future-trends-for-offshore-wind.html>.

BIBLIOGRAPHY

Hydraulic Model

A.1 Variable Stiffness

When a system experiences pressures changing from above 25[bar] down to 15[bar] or changes in the oil temperatures it can be necessary to consider a variable stiffness in the oil (β). The effective stiffness of the fluid-air mixture dependent on pressure (P), temperature (t) and volumetric ratio of free air (ϵ_A) is defined as [Andersen and Hansen, 2004, p. 8-10]:

$$\beta_{eff}(t, P, \epsilon_A) = \frac{1}{\frac{1}{\beta_F} + \frac{\epsilon_A}{\beta_A}} \quad (\text{A.1})$$

where:	β_{eff}	Effective stiffness of the fluid
	β_F	Stiffness of pure fluid
	β_A	Stiffness of pure air
	ϵ_A	Volumetric ratio of free air in the fluid
	t	Temperature
	P	Pressure

Often a reference volumetric ratio (ϵ_{A0}) at atmospheric pressure is used:

$$\epsilon_{A0} = \frac{V_{A0}}{V_{F0} + V_{A0}} \quad (\text{A.2})$$

where:	ϵ_{A0}	Reference volumetric ratio at atmospheric pressure
	V_{A0}	Volume of air at atmospheric pressure
	V_{F0}	Volume of fluid at atmospheric pressure

This reference air mixture is set to 0.01. To evaluate the fluid bulk modulus, Equation A.3 is

applied.

$$\epsilon_A = \frac{1}{\left(\frac{1.0 - \epsilon_{A0}}{\epsilon_{A0}}\right) \frac{\rho_0(t_0)}{\rho(t, P)} \left(\frac{P_{atm}}{P_a}\right)^{\left(\frac{-1}{c_{ad}}\right)} + 1.0} \quad (\text{A.3})$$

where: $\rho_0(t_0)$ Density at atmospheric pressure
 $\rho(t, P)$ Density
 P_a Absolute pressure in fluid
 c_{ad} Adiabatic constant for air - 1.4

Since the only variable here is the pressure of the fluid, the stiffness is directly calculated from Equation A.3 inserted in Equation A.1. When simulating this relation it is often necessary to model the stiffness with a maximum, since it in most application are not higher than 10,000[bar], as a rule of thumb according to [Andersen and Hansen, 2003]. This should be reconsidered when further modeling and testing is fulfilled, since the stiffness in some cases can be up to 14 – 16,000[bar]. The stiffness is illustrated on Figure A.1.1

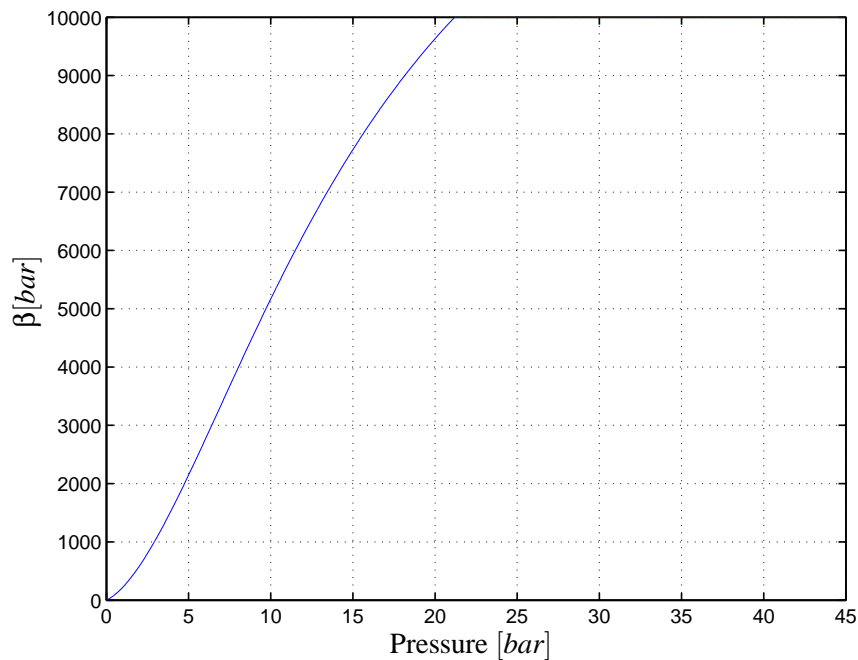


Figure A.1.1: Bulk modulus as a function of pressure at constant temperature of 40[°C].

This chapter consists of further explanations of some of the elements applied in the CFD analysis.

B.1 Fundamental Fluid Dynamics

Every fluid can be described as a function of temperature, velocity, density, and pressure. This correlation is the Navier-Stokes equations, which are essential in order to understand fluid dynamics. Several versions exist, but the finite volume method, with constant temperature, density, and viscosity is applied here. This method sets a finite volume of fluid, e.g. the volume in the valve, the boundary conditions, and calculates the pressure, turbulence and velocity of the particles inside the volume. The equations are presented in Equation B.1 to B.3.

$$\rho \frac{Du}{Dt} = -\frac{\partial P}{\partial x} + \text{div}(\mu \nabla u) + S_{Mx} \quad (\text{B.1})$$

$$\rho \frac{Dv}{Dt} = -\frac{\partial P}{\partial y} + \text{div}(\mu \nabla v) + S_{My} \quad (\text{B.2})$$

$$\rho \frac{Dw}{Dt} = -\frac{\partial P}{\partial z} + \text{div}(\mu \nabla w) + S_{Mz} \quad (\text{B.3})$$

where:	u, v, w	Velocity in x, y, z direction respectively
	$\frac{D}{dt}$	The total/material derivative
	$\nabla u/v/w$	Gradient of velocity u, v, w respectively
	$\text{div } \vec{u}$	Divergence of \vec{u}
	\vec{u}	Velocity vector containing (u, v, w)
	S_M	Source terms such as body forces, e.g. gravity.

To understand these equations the divergence, gradient, and total derivative is described in Equation B.4, B.5, and B.6 respectively.

The gradient is a vector field containing the partial derivatives of a function with respect to x, y, z . ϕ_{ar} is an arbitrary function of three coordinates x, y, z .

$$\nabla \phi_{ar} = \left(\frac{\partial \phi_{ar}}{\partial x}, \frac{\partial \phi_{ar}}{\partial y}, \frac{\partial \phi_{ar}}{\partial z} \right) \quad (\text{B.4})$$

where: ϕ_{ar} Arbitrary function

The divergence of a vector field is defined as:

$$\text{div } \phi_{ar} = \frac{\partial \phi_{ar}}{\partial x} + \frac{\partial \phi_{ar}}{\partial y} + \frac{\partial \phi_{ar}}{\partial z} \quad (\text{B.5})$$

The total derivative is taken along a path moving with velocity \vec{u} , and describes the rate of change of some arbitrary quantity, ϕ_{ar} . However ϕ_{ar} is now also a function of time such that $\phi_{ar}(x, y, z, t)$.

$$\begin{aligned} \frac{D\phi_{ar}}{Dt} &= \frac{\partial \phi_{ar}}{\partial t} + \frac{\partial \phi_{ar}}{\partial x} \frac{\partial x}{\partial t} + \frac{\partial \phi_{ar}}{\partial y} \frac{\partial y}{\partial t} + \frac{\partial \phi_{ar}}{\partial z} \frac{\partial z}{\partial t} \\ &= \frac{\partial \phi_{ar}}{\partial t} + \frac{\partial \phi_{ar}}{\partial x} u + \frac{\partial \phi_{ar}}{\partial y} v + \frac{\partial \phi_{ar}}{\partial z} w \end{aligned} \quad (\text{B.6})$$

B.1.1 Turbulence Modeling

The model describes the turbulence by dividing the flow into the turbulence energy, k , and the dissipation rate, ϵ . At Reynolds no. below 5000, the $k - \epsilon$ model has poor performance but since it is above this in this model, cf. Figure 3.1.1, the performance is considered acceptable.

The standard $k - \epsilon$ model can be modified using *The Renormalization Group (RNG)* [Versteeg and Malalasekera, 2007]. This improves the performance when modelling rapidly changing, streamline curvature, and swirling flows. All of these are present in the modelled valve, hence this version of the model is chosen. Furthermore the RNG-model is known to give more precise results than the standard $k - \epsilon$ solver. However, it is also more numerically unstable than the standard solver, and increases the computation time.

B.1.2 Discretisation and Solution Methods

The *SIMPLE* algorithm scheme (Semi-Implicit Method for Pressure Linked Equations) which couples the pressure and velocity is chosen [Versteeg and Malalasekera, 2007, pp. 3-4].

This algorithm is often used with steady flows, which fits this problem set-up. It can be set to use first or second order approximation, which refers to the accuracy of the approximated function. The second order functions will converge slower, but more accurate compared with the first order function. To decrease the calculation time the first order approximation is chosen as sufficient.

B.1.3 Convergence and Tolerance

A series of factors affects the convergence and calculation time; the chosen maximum residuals, mesh quality, initial conditions, and the complexity of the problem. Most significant is the max-

imum residual value which controls the desired precision of the calculation, i.e. the accuracy of the solution. The maximum value is set to $1 \cdot 10^{-4}$, which is considered acceptable.

B.2 Boundary Conditions

Well-defined boundary conditions are required to calculate valid results. The conditions of the valve are described here:

- Inlet - The fluid is set to a specific velocity u_{in} at the inlet, furthermore the turbulent intensity and hydraulic diameter is set. The velocity is changed from 0 to $15 [m/s]$ in order to simulate different flow situations.
- Outlet - The pressure P_{out} is set to $0[bar]$, this means that the pressure difference across the valve is relative to this value. The turbulence intensity and the hydraulic diameter at this point is also required.
- Walls - The surface roughness of the walls is set to 0. The boundary layer caused by a possible roughness is not examined in this project. The effect of surface roughnesses is expected to be low compared to the influence of the interior geometry of the valve.

The turbulence intensity at the in- and outlet is set to 5%, which is an appropriate guess when dealing with internal flows [European Research Community On Flow and Combustion, 2000]. However the turbulence intensity in a valve directly mounted on a cylinder will likely experience a higher degree of turbulence due to the contracting flow in the restricted inlet area of the valve. This would have to be measured in a test rig, in order to adjust the intensity properly.

The hydraulic diameter determines the dissipation rate, and is set to $63[mm]$ at in- and outlet. Again it is not completely true to set the hydraulic diameter equal to the diameter of the tube since the flow through the inlet is only partly similar to the flow through a circular pipe.

Even though these boundary conditions are a guess, the overall behaviour of the flow will still be considered applicable for this analysis.

B.3 Meshing

A finite control volume of a fluid is meshed into small elements. To decrease the number of elements, symmetry through the $x - y$ plane, illustrated on Figure B.3.1 is applied. This halved the no. of elements.

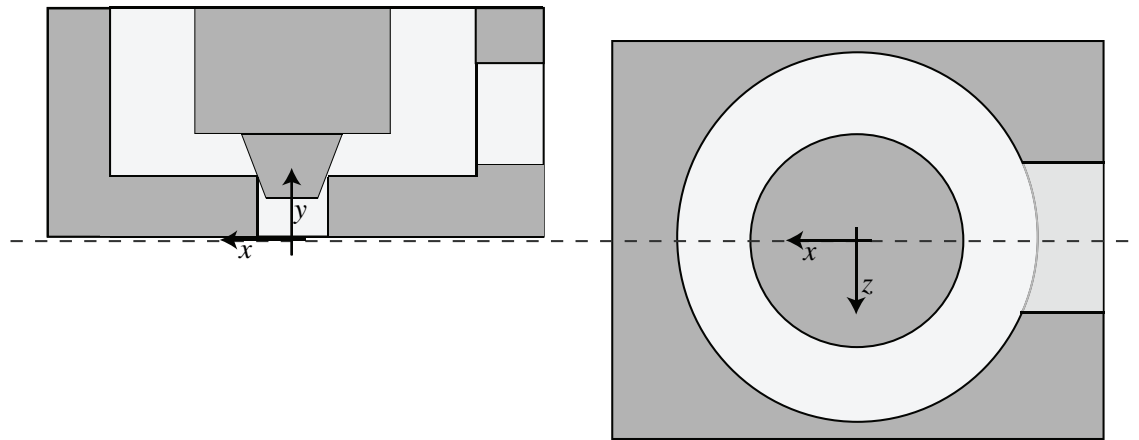


Figure B.3.1: Global coordinate system of the valve.

The method used for meshing the fluid, is the default setting in *ANSYS Mesh* for *ANSYS Fluent*. The mesh quality is adjusted in the settings in the CFD-program, and is a compromise between validity and calculation, converging and meshing time.

If the mesh quality is poor, the problem will be difficult to converge. However, if the mesh is too fine, the problem will also have a long convergence time due to the increment in elements.

B.3.1 Final Mesh

The mesh of the standard NG63 and the deflector valve is described in this section.

The NG63 mesh is fairly simple and mostly standard settings are used, cf. Table B.3.1 and Figure B.3.2 in this section. Figure B.3.2 illustrates the meshed fluid in the NG63 valve, cf. Figure 2.2.4 for an illustration of the valve. Notice that only half of the valve is meshed due to the symmetry as described in Figure B.3.1.

To evaluate a mesh the skewness is often used as an indicator, it is a ratio between 0 and 1, where 0 is a perfect mesh and 1 is an unacceptable mesh. The mesh settings used in the NG63 valve resulted in an average skewness of 0.24 and a maximum of 0.94. This is considered sufficient for this application. If a lower skewness was required, a solution could be to decrease the maximum face size or the curvature normal angle.

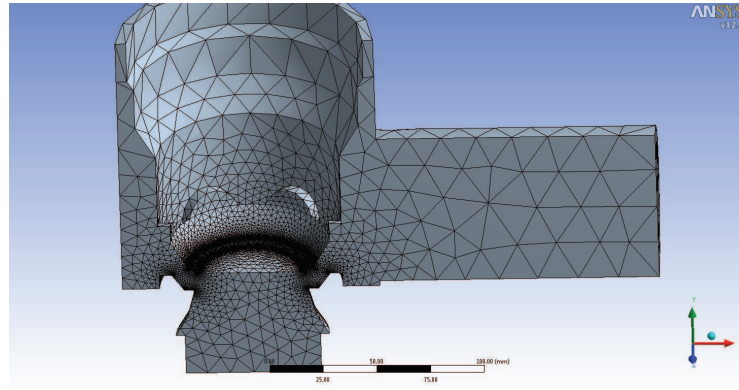
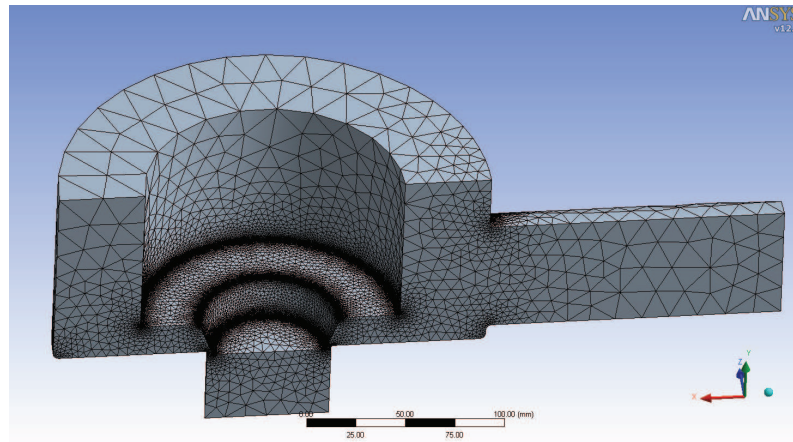
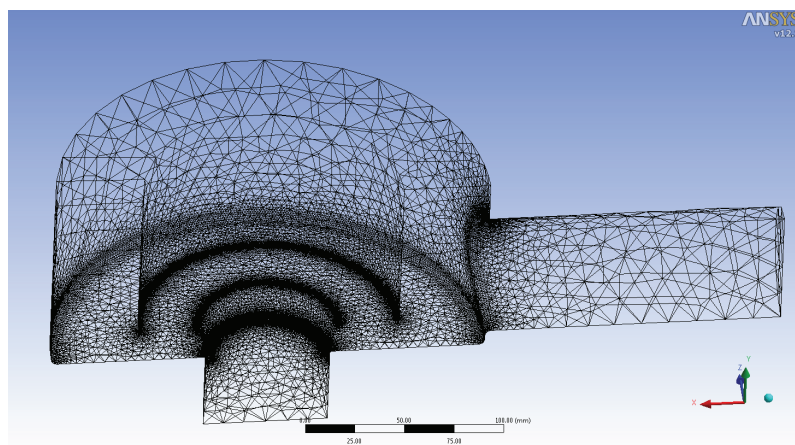


Figure B.3.2: Mesh of the standard NG63 valve in 10[mm] opened position.



(a) Exterior edges and shades



(b) Wireframe.

Figure B.3.3: Mesh of deflector valve in 10[mm] opened position.

The mesh of a 10[mm] opened deflector valve is illustrated on Figure B.3.3. The mesh of the deflector valve in the three lowest positions ($x_{pop} = 1, 2, 3[mm]$) had a high maximum skewness

of 0.98, hence a refinement setting was used to increase the no. of elements in the opening area. This resulted in a lowered maximum skewness of 0.84 and an average skewness of 0.24. The increment in elements from 500,000 to 900,000 is illustrated in Figure B.3.4. This also increases calculation time, hence this is only applied when necessary. A selection of settings of the final mesh for a 2[mm] and a 10[mm] open valve is given in Table B.3.3 and B.3.2.

Figure B.3.4 illustrates the difference between the 10[mm] and the 2[mm] open valve. Notice the even higher increment in elements around the edges in the opening area.

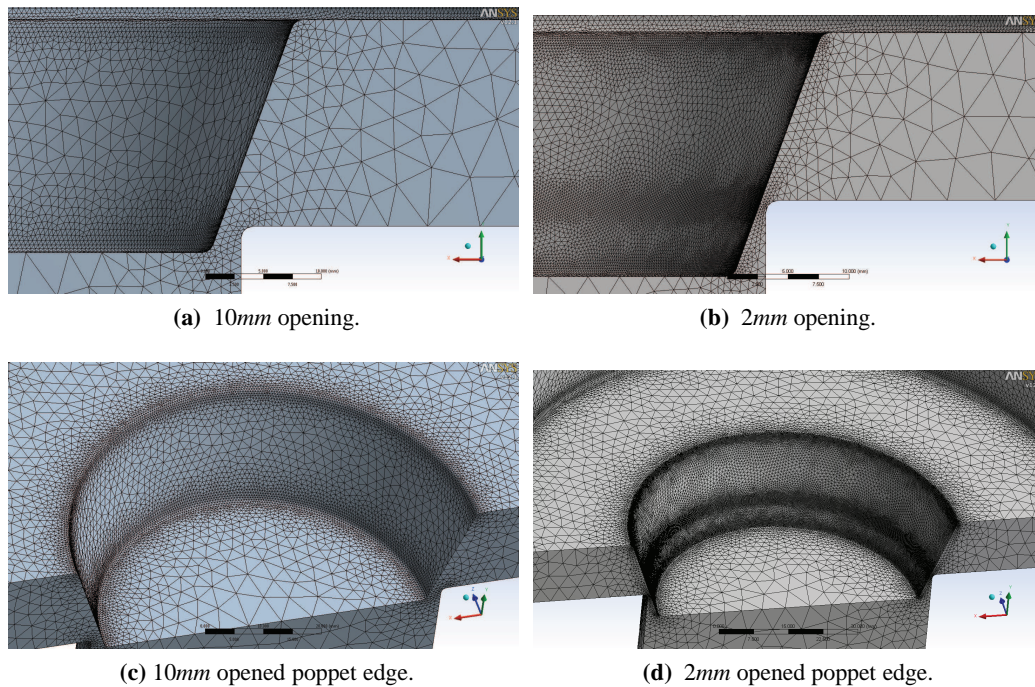


Figure B.3.4: Focus on the difference between 2[mm] and 10[mm] open deflector valve

B.3.2 Mesh Settings

This section illustrates a small selection of mesh settings of the CFD analysis.

Setting	Value	Note
Relevance	-60	Adjusted
Quality	Medium	Adjusted
Smoothing	Medium	Adjusted
Transition	Slow	Adjusted
Max face size	20[mm]	Adjusted
Max tet. size	20[mm]	Adjusted
Growth rate	1.2	Default
Max. curvature normal angle	23.7°	Default
No. elements	557656	Calculated
Nodes	105503	Calculated

Table B.3.1: Mesh settings for 5[mm] open NG63 valve.

Setting	Value	Note
Relevance	-40	Adjusted
Quality	Medium	Adjusted
Max face size	20[mm]	Adjusted
Max tet. size	20[mm]	Adjusted
Growth rate	1.2	Default
Max. curvature normal angle	23.76°	Adjusted
No. elements	59611	Calculated
Nodes	111315	Calculated

Table B.3.2: Mesh settings for 10[mm] open NG63 valve.

Setting	Value	Note
Relevance	-40	Adjusted
Quality	Medium	Adjusted
Max face size	20[mm]	Adjusted
Max tet. size	20[mm]	Adjusted
Growth rate	1.2	Default
Max. curvature normal angle	18°	Adjusted
No. elements	596111	Calculated
Nodes	111315	Calculated

Table B.3.3: Mesh settings for 10[mm] open Deflector valve.

B.4 CFD Result Figures

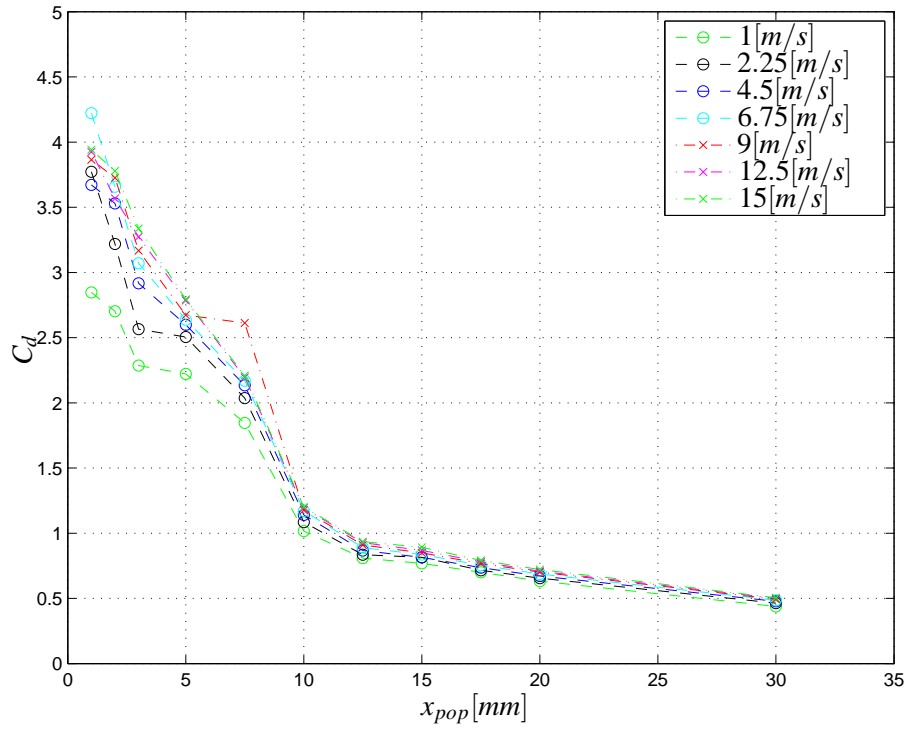


Figure B.4.1: C_d of inlet deflector valve as a function of poppet position.

$x_{pop} [m] \rightarrow$	0.00100	0.00200	0.00300	0.00500	0.00750	0.0100	0.0125	0.0150	0.0175	0.02	0.03
$A(x_{pop}) [m^2] \rightarrow$	$4.40 \cdot 10^{-5}$	$7.11 \cdot 10^{-5}$	$1.00 \cdot 10^{-4}$	$1.64 \cdot 10^{-4}$	$2.96 \cdot 10^{-4}$	$7.96 \cdot 10^{-4}$	$1.23 \cdot 10^{-3}$	$1.66 \cdot 10^{-3}$	$2.11 \cdot 10^{-3}$	$2.57 \cdot 10^{-3}$	$4.45 \cdot 10^{-3}$
$u_{in} [m/s] \downarrow$											
1	2.811	1.199	0.8451	0.3321	0.1482	0.06757	0.044495	0.0271	0.020288	0.01678	0.0116
2.25	8.108	4.279	3.397	1.324	0.6165	0.3	0.211197	0.122	0.098319	0.07908	0.0527
4.5	34.22	14.23	10.51	4.918	2.244	1.087	0.7843	0.4892	0.372462	0.3007	0.199
6.75	58.26	29.82	21.33	10.74	4.887	2.318	1.674	1.045	0.7961	0.6472	0.431
9	123.6	51.09	35.63	18.59	5.991	4.078	2.851	1.79874	1.366	1.105	0.745
12.5	231.1	107.5	64.4	33.04	16.38	7.675	5.292	3.318	2.54748	2.08716	1.39
15	330	138	89.21	47.28	23.27	10.9	7.483	4.531	3.574	2.90	1.97

Table B.4.1: Pressure drop across the deflector valve in $[bar]$.

$x_{pop} [m] \rightarrow$	0.00100	0.00200	0.00300	0.00500	0.00750	0.0100	0.0125	0.0150	0.0175	0.02	0.03
$A(x_{pop}) [m^2] \rightarrow$	$4.40 \cdot 10^{-5}$	$7.11 \cdot 10^{-5}$	$1.00 \cdot 10^{-4}$	$1.64 \cdot 10^{-4}$	$2.96 \cdot 10^{-4}$	$7.96 \cdot 10^{-4}$	$1.23 \cdot 10^{-3}$	$1.66 \cdot 10^{-3}$	$2.11 \cdot 10^{-3}$	$2.57 \cdot 10^{-3}$	$4.45 \cdot 10^{-3}$
$u_{in} [m/s] \downarrow$											
1	2.847	2.703	2.285	2.222	1.846	1.016	0.809	0.769	0.700	0.632	0.439
2.25	3.772	3.219	2.565	2.504	2.036	1.085	0.835	0.815	0.715	0.655	0.463
4.5	3.672	3.530	2.916	2.599	2.134	1.140	0.867	0.814	0.735	0.672	0.477
6.75	4.221	3.658	3.071	2.638	2.169	1.171	0.890	0.836	0.754	0.687	0.486
9	3.864	3.726	3.168	2.673	2.612	1.177	0.909	0.849	0.768	0.701	0.493
12.5	3.925	3.568	3.273	2.785	2.194	1.192	0.927	0.869	0.781	0.708	0.500
15	3.942	3.779	3.337	2.794	2.209	1.200	0.935	0.892	0.791	0.721	0.505

Table B.4.2: Discharge coefficient in the deflector valve.

Opening Area of Deflector Valve

This chapter describes the opening area of the deflector valve.

C.1 Stage 1

The poppet and the necessary lengths are given in Figure C.1.1. To develop an expression for the opening area, the fillet radius (R_m) of the seat edge must be incorporated. To do this, the first task is to convert the spool position, x_U , for a sharp edged valve i.e. $R_m = 0$ (marked with red) to a spool position x_R for a valve with a fillet radius, i.e. $R_m \neq 0$ (marked with green). Looking at Figure C.1.1 x_R is an addition of x_U , h_1 and h_2 :

$$x_R = x_U + h_1 + h_2 \quad (C.1)$$

where:	x_R	Corrected spool position
	x_U	Uncorrected spool position
	h_1	Length given in Figure C.1.1
	h_2	Length given in Figure C.1.1

h_1 (marked with orange) is illustrated at the upper left corner of the Figure. By applying the cosine and tangent relation h_1 is given as:

$$h_1 = \tan\left(\frac{\pi}{2} - \alpha\right) (R_m (1 - \cos(\alpha))) \quad (C.2)$$

where:	R_m	Fillet radius of the edge.
	α	Angle of the poppet, given in Figure C.1.1

h_2 (marked with blue) is found by applying the sine relation.

$$h_2 = R_m - R_m \sin(\alpha) \quad (C.3)$$

$$= R_m (1 - \sin(\alpha)) \quad (C.4)$$

C. Opening Area of Deflector Valve

x_R now becomes:

$$x_R = x_U + \tan\left(\frac{\pi}{2} - \alpha\right) (R_m(1 - \cos(\alpha))) + R_m(1 - \sin(\alpha)) \quad (C.5)$$

To calculate the opening area, r_{Ds} , r_{Dc} and s_R on Figure C.1.1 is required. First s_R and w_R is defined as:

$$s_R = x_R \sin(\alpha) \quad (C.6)$$

$$w_R = x_R \cos(\alpha) \quad (C.7)$$

where: s_R Length given in Figure C.1.1.

w_R Length given in Figure C.1.1.

The radii r_{Ds} and r_{Dc} are defined as:

$$r_{Ds} = r_{in} + R_m - R_m \cos(\alpha) \quad (C.8)$$

$$= r_{in} + R_m(1 - \cos(\alpha)) \quad (C.9)$$

$$r_{Dc} = r_{Ds} - w_R \sin(\alpha) \quad (C.10)$$

where: r_{Ds} Radius given in Figure C.1.1.

r_{Dc} Radius given in Figure C.1.1.

r_{in} $\frac{1}{2}d_i n$

Now the opening area can be defined as a cone frustum with outer radius r_{Ds} and inner radius r_{Dc} and the side s_R :

$$A(x_{pop}) = \pi s_R (r_{Dc} + r_{Ds}) \quad (C.11)$$

$$= 2\pi x_R \sin(\alpha) (r_{in} + R_m(1 - \cos(\alpha)) - x_R \sin(\alpha) \cos(\alpha)) \quad (C.12)$$

C.2 Stage 2

The second stage is defined as the area function when the lower edge of the poppet is above the edge of the seat. Now the inlet area is defined as a new function. This happens when $x_{pop} > x_{pop_e}$, and x_{pop_e} is the position where the area function changes. Figure C.2.1 illustrates the lengths and names needed to define this function.

To define the function, first the original spool position is altered using the displacement x_{pop_e} (marked

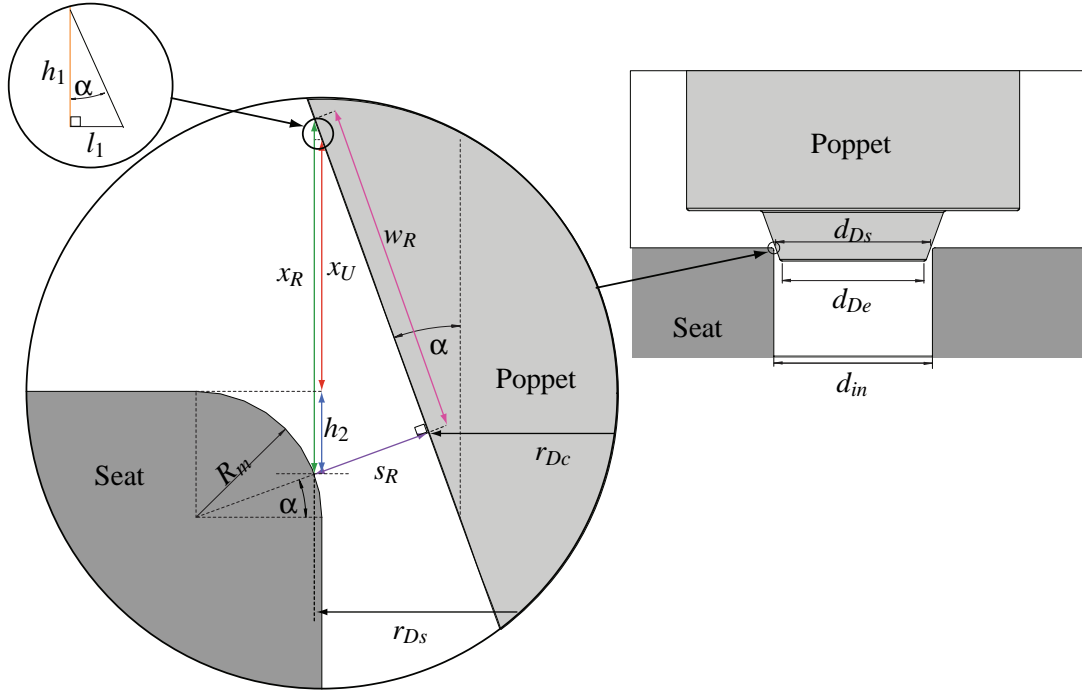


Figure C.1.1: Poppet at a given opening including two detail views.

with yellow):

$$x_R = x_U - x_{pop_e} \quad (C.13)$$

s_R is marked with purple and is calculated by applying pythagoras and that $h_3 = x_R + 2R_m$:

$$s_R = \sqrt{(l_3^2 + h_3^2)} - 2R_m \quad (C.14)$$

where: l_3 Length as given in Figure C.2.1, measured in CAD

The large radius of the cone frustum r_{Ds} is calculated by applying arcus tangent and the cosine relation:

$$r_{Ds} = r_{in} + R_m \left(1 - \cos \left(\arctan \left(\frac{h_3 + R_m}{l_3 + R_m} \right) \right) \right) \quad (C.15)$$

The radius r_{De} is measured and inserted along with r_{Ds} and s_R in Equation C.16

$$A(x_{pop}) = \pi s_R (r_{Ds} + r_{De}) \quad (C.16)$$

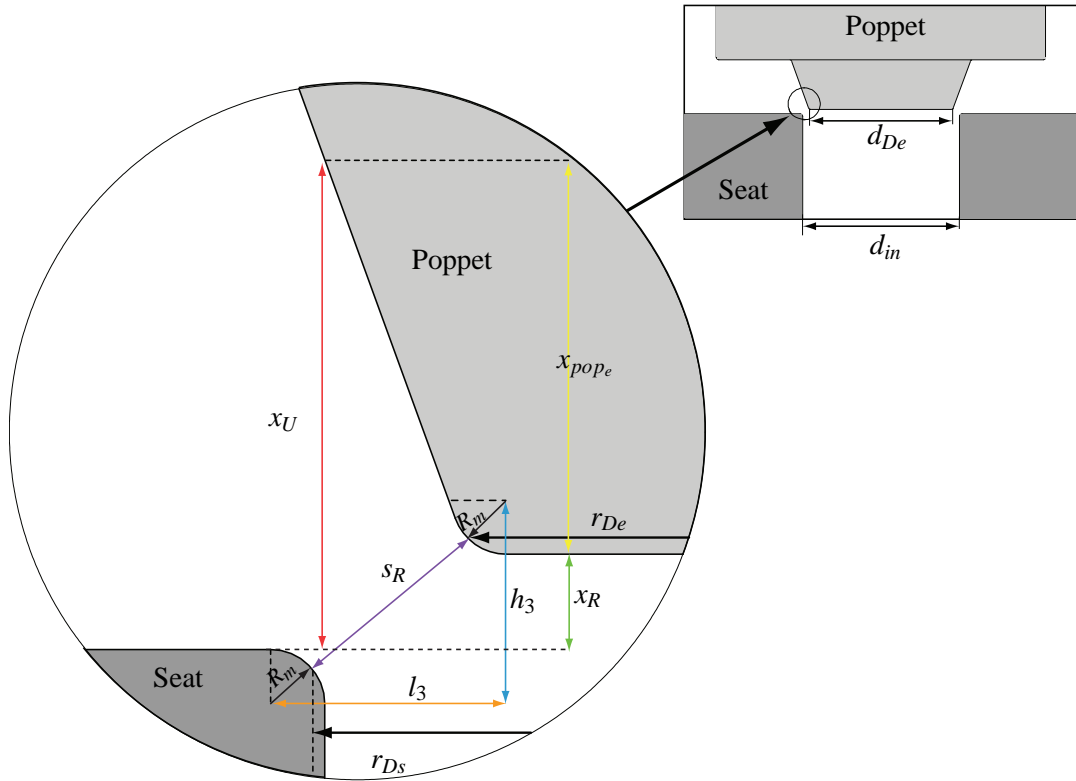


Figure C.2.1: Poppet at stage 2.

The opening area is now defined and can be illustrated as a function of x_{pop} in Figure C.2.2. The blue line illustrates the area function as a discontinuous function, this means that the transitional region between the two stages is not modelled. If a more accurately function was needed, this area would have to be modelled more accurate as well. Instead a rate-limiter is inserted to prevent any discontinuity. The rate limiter, limits the first derivative of the opening area. If the derivative is above the limit (R_{limit}), the opening area will be calculated as:

$$A(x_{pop_i}) = R_{limit} \delta t + A(x_{pop_{i-1}}) \quad (C.17)$$

where: R_{limit} Rate limit

δt Time step

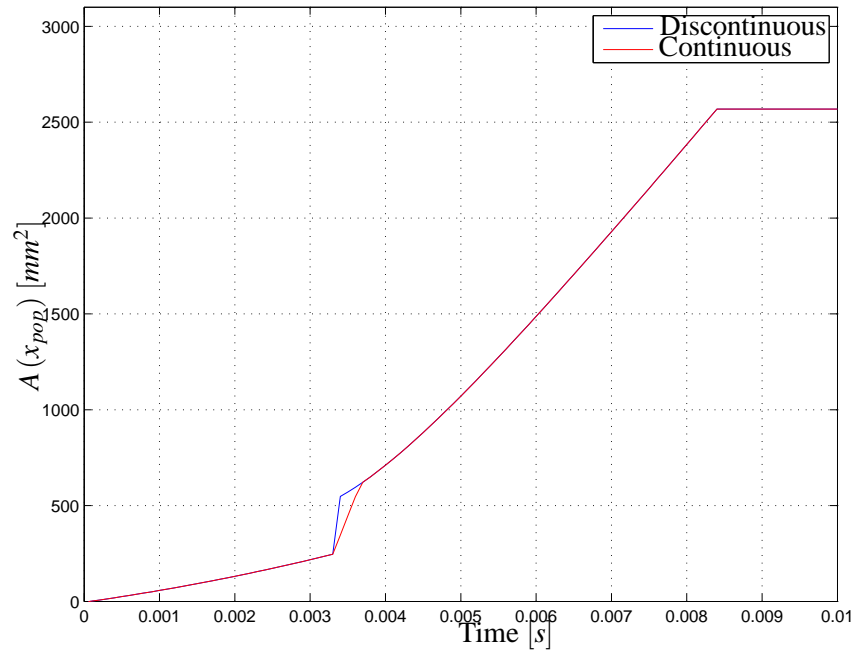


Figure C.2.2: Opening area function.

From Figure C.2.2 it is clear that the opening area increases significantly when entering stage 2 at approximately 0.003[s].

C. Opening Area of Deflector Valve

Friction and Leakage

D.1 Flow Factors

This section describes the flow factors applied in the piston ring model.

D.1.1 Pressure flow factor ϕ_x

The pressure flow factor ϕ_x compares the average flow due to pressure in a rough bearing to that of a smooth surface. ϕ_x is a function of the fluid film height and the surface roughness, and can for isotropic materials be approximated to: [Patir and Cheng, 1978]:

$$\phi_x = 1 - 0.9 \cdot \exp(-0.56H_\sigma) \quad (\text{D.1})$$

where: H_σ Ratio between surface height and surface roughness, h/σ

As the fluid film height H_σ increases above ≈ 7 , ϕ_x approaches 1, and for low H_σ ϕ_x approaches 0 [Patir and Cheng, 1978]. This is only possible under the assumption of an isotropic material. If the material is not isotropic, the pressure flow factor consists of two separate factors in the x and y -direction respectively.

D.1.2 Shear flow factor ϕ_s

The shear flow factor represents the additional flow due to sliding in a rough bearing. If the two surfaces have identical roughnesses this flow factor is set to zero. If this is not the case the flow factor is between zero and one.

D.1.3 Contact flow factor ϕ_c

The contact factor ϕ_c concerns the average gap between two surfaces and for asperities with a Gaussian distribution the flow factor can be written as [Akalin and Newaz, 2001]:

$$\phi_c = 0.5(1 + \text{erf}(H_\sigma)) \quad (\text{D.2})$$

where: $\text{erf}(x)$ Error function

D.1.4 Shear stress flow factor ϕ_f and ϕ_{fs}

The shear stress flow factor ϕ_f concerns the sliding velocity component of shear stress. It can be obtained through integration, for any given density of aperities, of the roughness heights. The density of aperities is assumed to be a Gaussian distribution and can be approximated by the following formula derived by Patir and Cheng [Patir and Cheng, 1978]. The function is separated into two intervals; $H_\sigma \leq 3$ and $H_\sigma > 3$.

For $H \leq 3$


$$\phi_f = \frac{35}{32}z \left((1-z^2)^3 \cdot \ln \frac{z+1}{\epsilon^*} + \frac{1}{60} [-55 + z(132 + z(345 + z(-160 + z(-405 + z(60 + 147z))))]) \right) \quad (D.3)$$

And for $H > 3$

$$\phi_f = \frac{35}{32}z \left\{ (1-z^2)^3 \ln \frac{z+1}{z-1} + \frac{z}{15} [66 + z^2 (30z^2 - 80)] \right\} \quad (D.4)$$

$$H_\sigma = \frac{h}{c} \quad z = \frac{H_\sigma}{3} \quad \epsilon^* = \frac{1}{300} \quad (D.5)$$

ϕ_{fs} is much like ϕ_f but concerns the combined effect of roughness and sliding in terms of mean flow. If the surfaces have identical surface roughness, it is equal to zero which is the case here. If not, it can be approximated by equations written in [Patir and Cheng, 1978].



Efficiency Analysis of a Radial Piston Pump Applied in a 5MW Wind Turbine with Hydraulic Transmission

Kasper Aastrup Mortensen

Klaus Høj Henriksen

Master Thesis in Electro-Mechanical System Design

Aalborg University 2011